CENTRO DE INVESTIGACIONES EN ÓPTICA, A.C.

OPTICAL FIBERS AS ACTIVE MEDIA FOR LASERS
(Raman-Type and Tm-doped)

THESIS SUBMITTED AS PARTIAL FULFILMENT OF REQUIREMENTS FOR OBTAINING THE DEGREE OF DOCTOR OF PHILOSOPHY IN THE FIELD OF SCIENCE (OPTICS)

By

MSc. Maribel Juárez Hernández

Supervisors: Dr. Efraín Mejía Beltrán (CIO)

Dr. Lelio de la Cruz May (UNACAR)

January 2018

León Guanajuato, México

Declaration

I hereby declare that the investigations presented in this thesis have been carried out by me under the supervision of my advisors *Dr. Efraín Mejía Beltrán* and *Dr. Lelio de la Cruz May*. The work is original and has not been submitted in another thesis or dissertation to get a degree, similar or equal to the one intended to obtain here, or any other University or Institution.

To my beloved family and my dear husband,
for all their love and support;
without whom none of my success would be possible.

Acknowledgments

I would like to thank my advisors *Dr. Efraín Mejía Beltrán* and *Dr. Lelio de la Cruz May* and express my sincere gratitude for their entire patient and helpful guidance through my PhD. degree; also acknowledge their time dedicated to this work, to their advices and corrections. Likewise, I would like to thank to my evaluation committee, *Dr. Alexander Kir'yanov, Dr. Olivier Pottiez*, and *Dr. Verónica Vázquez García*, for all their comments and suggestions. I also want to express my gratitude to all those who have been part of my professional and personal education; my family, teachers, friends and colleagues; apologizes for not naming everyone.

This research was supported by Consejo Nacional de Ciencia y Tecnología (CONACYT) who provided me the scholarship No. 377309 and was the contributor to the project CB- 2011-01/166740 that made possible this thesis. Hence, we thank to CONACYT for this valuable support.

Table of contents

Chapter 3: Second (1178 nm) and third (1242 nm) Stokes Raman fiber lasers without intermediate Stokes cavities

Chapter 4: Rare earth doped optical fibers

Chapter 5: Red laser-diode pumped Tm^{3+}: ZBLAN fiber laser

List of figures

Chapter 1: Raman scattering in optical fibers

Chapter 2: Energy transfer mechanisms in a RFL under different cavity configurations

Chapter 3: Second (1178 nm) and third (1242 nm) Stokes Raman fiber lasers without intermediate Stokes cavities

Chapter 4: Rare earth doped optical fibers

Chapter 5: Red laser-diode pumped Tm^{3+}: ZBLAN fiber laser

Chapter 6: Short wavelength emission by up-conversion in a Tm^{3+}: ZBLAN single and dual-diode-pumped optical fiber

Appendix A: Calibration of wavelength of the Ocean Optics USB2000

List of tables

Chapter 4: Rare earth doped optical fibers

Chapter 5: Red laser-diode pumped Tm^{3+}: ZBLAN fiber laser

Appendix A: Calibration of wavelength of the Ocean Optics USB2000

I. Motivations

Optical fiber laser systems have properties that make them highly efficient and in several aspects superior over solid state lasers. The geometrical properties of these systems provide several advantages: their lengths allow higher pump absorption; and overlapping of the signals whereas their thinness allow greater heat dissipation. Besides being compact, the cavities are very stable and immune to external vibrations. Although these kinds of lasers have been investigated since the time of the 1960s, the development of new fiber materials and commercial compact pumps such as laser diodes allow novel and even more compact designs.

In this work, we pursued the demonstration and improvement of new schemes for fiber laser systems, using stimulated Raman scattering and rare earth doped optical fibers; motivated in the fact that the first kind provides an alternative choice to obtain wavelength agile, scalable technology that can span the wavelength spectrum, in addition of low background spontaneous emission. Moreover, these systems can convert practically the entire pump into laser signal, and thermal management becomes relatively easy, especially for Raman fiber lasers due to small absorption at each point of the fiber.

The research of new fiber-based lasers schemes could be useful for various scientific and technological applications, for example: improving the performance in long/ short-range optical communications links, amplification in wavelength division multiplexed signals, laser spectroscopy, sensor systems, and medical applications such as in the fields of dermatology and ophthalmology.

II. Objectives

In this research work we analyzed and proposed novel pumping schemes for Raman fiber lasers (RFLs) for further improvement of infrared optical generation. An analysis related to energy transfer mechanisms between all the signals involved (pump, Stokes, and anti-Stokes) and their generation threshold in different laser cavities (*e.g.*, conventional cavities using fiber Bragg gratings (FBGs) and Random distributed feedback (RFDB)) was conducted. We used output couplers with different reflectivities in all the different laser cavities, in order to understand most of the mechanisms involved in these systems.

Furthermore, we demonstrated an optimized cascade RFL that eliminates the use of several FBGs. This system minimizes the cost of the insertion-loss imposed by the FBGs improving their efficiency.

In addition, we demonstrated new pumping schemes of fluorozirconate optical fibers doped with thulium by using new availability of wavelengths in laser diodes (LDs). We are mainly looking for generating infrared (IR), visible (Vis), and ultraviolet (UV) signals in more efficient, compact and inexpensive fiber laser systems. Pumping these fibers can be more easily afforded with LDs which are economical and efficient light sources. The generation and operation of these lasers systems at the present is quite expensive, in terms of maintenance, storage and cooling costs. Multiple potential applications of these new laser schemes can be easily achieved in numerous research fields and disciplines, increasing benefits and reducing costs.

III. Summary

In this thesis two different main projects were implemented. The first main project is related to RFLs and the second one to doped fiber lasers systems.

The RFL main project was divided in two different investigations; the first one was an experimental study of the signals involved in a RFL under different output coupling conditions. The second one was a demonstration of an alternative to cascade RFL. For the doped fiber laser project, we investigated IR, Vis, and UV generation using new pumping schemes in fluorozirconate fibers.

In the RFL experimental study involving different output coupling conditions, variations in the reflectivity of the output coupler for different cavity laser systems was carried out. We applied conventional cascaded RFL and Random distributed feedback (RDFB) cavities. We concluded that feedback increase does influence negatively on the energy-transfer mechanisms among all the signals involved, hence it also negatively affects the generation threshold for these signals.

In the second RFL study, we proposed a RFL scheme, consisting on modifying a conventional cascade RFL by eliminating the intermediate FBGs, corresponding to cavities for intermediate Stokes signals. In this way, the lower Stokes orders act as virtual links that transfer energy to higher Stokes signals, minimizing the cost of longer fibers and the insertion loss of the FBGs.

Regarding rare–earth (RE) doped optical fiber experiments, we propose the implementation of new fiber laser pumping schemes based on fluorozirconate [ZBLAN (ZrF_4-BaF_3-LaF_3-AlF_3-NaF)] optical fibers doped with thulium. Our starting point was the analysis of emission and absorption cross-sections of the energy levels of Tm^{3+} and the spectral analysis of these schemes. Also, we carried out the theoretical calculation of the optimal fiber lengths for obtaining optimal efficiency.

We described for the first time a continuous wave (CW) laser emitting at 806 nm when diode-pumped at 687 nm in a Tm^{3+}: ZBLAN fiber. This device is suitable for first telecom window and sensing applications. We also explored the possibility for obtaining 450 nm (visible) and 360 nm (UV) in Tm^{3+}: ZBLAN by up-conversion with single and double line pumping with 687 nm and 645 nm LDs. These experimental systems would demonstrate that excitation with visible wavelengths between 640 nm – 690 nm (red) may be feasible for the creation of very efficient and highly functional visible (450 nm) and UV (360 nm) fiber lasers for applications in various areas of industry, medicine and computer science.

It is worth mentioning that we are pioneers in proposing these pumping schemes with visible light LDs (red) for the development of new laser systems. These systems have the advantage of working at room temperature in addition that they do not present photodarkening (*i.e.*, the phenomenon in which the losses of the optical power increase in a medium while this is irradiated with light at certain wavelengths), since the visible light realizes a photobleaching (process inverse to the photodarkening) by itself.

This thesis is divided into five chapters. Chapter 1 shows a brief introduction to Raman scattering processes involved in Raman fiber laser systems. Chapter 2 and Chapter 3 illustrate the analysis and development of the processes involved for fiber laser systems using stimulated Raman scattering (SRS). Chapter 4 shows a small theoretical framework of the electronic and optical properties of rare earth-doped optical fibers. Also, the properties of silica glasses and the specific properties of fluorozirconate fibers doped with Tm^{3+} are touched. In Chapter 5 and Chapter 6 the experimental setups and methodology implemented for building Tm^{3+}: ZBLAN fiber laser systems are presented as well as the results obtained and conclusions.

Chapter 1

Raman Scattering in Optical fibers

Chapter 1

1. *Raman scattering*

1.1 Introduction

The interaction of light with matter can reveal important information about the structure and dynamics of the material, when scattered by some abnormalities present in the medium. This scattered light can conserve its kinetic energy and thus, an elastic scattering process occurs. We will refer to the process when the scattered light does not conserve its initial energy as inelastic scattering.

The first theoretical approach for inelastic scattered light was given by Smekal in 1923 [1]. He considered a model of two quantum levels and predicted sidebands in the spectrum of the scattered light. The Raman scattering effect was first observed by Raman in 1928, in a benzene-based liquid [2]. He observed that by exciting a sample with a certain frequency, the scattered light contained additional frequencies to the pump light. Later in 1962, Stimulated Raman scattering effect was discovered by Eckhardt, et al. [3]. They observed the appearance of lines with higher frequency than usual in a ruby laser.

The scattered light spectroscopy in materials can provide valuable information about the properties of the vibrational, electronic and magnetic states, making it an excellent tool for the study of elementary excitations in gases, liquids and solids. The first experiments about the Raman scattering were done in liquid materials with organic compounds. One of the first solid material in which such effect was observed was a quartz crystal, and was studied by Landsberg and Mandelstam [4]. Subsequently other materials were studied, including glasses. One of the features observed in glasses is that they possess a wider Raman gain spectrum, unlike crystals, whose spectrum is narrower. This phenomenon will be discussed further in the chapter.

The properties of glasses in the oxides category like SiO_2, GeO_2, and B_2O_4 have been widely studied because one of their applications for manufacturing optical fibers. Optical fibers can act as amplifiers and/or lasers, due to the effect of Raman scattering. The molecular composition of the fiber plays an extremely important role, since this determines the amount of Raman gain present in the fiber.

Raman scattering can also have a negative effect on optical fibers, since it imposes certain limitations in communication systems and affect the propagation of ultra-short pulses due to dispersion.

Throughout the chapter, the basic concepts are studied and fundamental properties of spontaneous and stimulated Raman scattering are discussed. Furthermore, propagation equations are described for Raman scattering along an optical fiber.

1.2 Spontaneous Raman scattering

In a homogeneous and isotropic medium, light propagates through the material with some loss due to absorption. However, if the material is not completely homogeneous, especially if the inhomogeneities are comparable to the wavelength of the light, it will spread in all directions in space. If the material shows only fixed spatial inhomogeneities, there will be no change in frequency of the scattered light; *i.e.* light will scatter elastically (Rayleigh scattering). Nevertheless, when vibrations of these inhomogeneities due to temperature exist, they add inelastic components, and the spectrum of the scattered light will show emission lines corresponding to temporal variations (Raman Scattering) [5].

Raman scattering is an inelastic light-matter interaction. When an incident photon hits the medium, (the photon has energy equivalent to $E = \hbar\omega_p$, where $\hbar$ represents 2π multiplied by the Planck constant and ω_p the angular frequency) there will be an energy and momentum transfer ($P = \hbar k$, where $\vec{k}$ represents the wave vector) to the natural vibrations of the molecules present in the medium. These are function of the medium temperature (vibrational modes). Therefore, the structure will have a perturbation due to the dipole moment. This phenomenon may occur in various materials; in particular, silica molecular bonds are highly susceptible to disturbances as shown in **figure 1.1**.

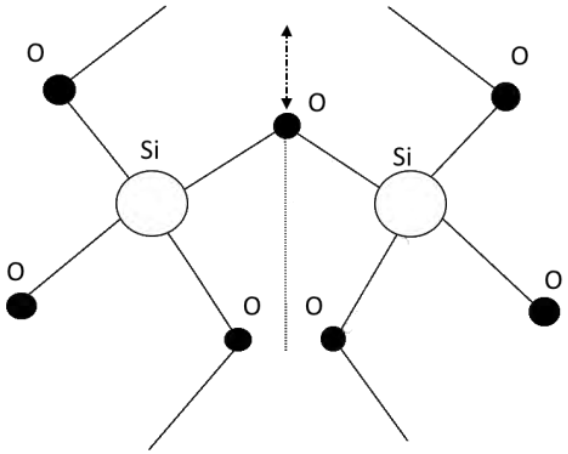

Figure 1.1 Silica (SiO_2) molecule Bond [6].

From a quantum point of view, the process of the Raman effect is the annihilation of a photon mode α (incident photon) and the creation of a photon mode β (scattered photon) [7]. Let us review the functions that describe the state of the system in terms of position and momentum variables [8]. The total Hamiltonian of the system can be described as in **equation 1.1**

$$H_{tot} = H_{vib} + H_{EB} + H_{\text{int}} \tag{1.1}$$

where H_{vib} describes the vibrational terms, consisting of kinetic and potential energy of the system (**equation 1.2**). $\vec{P}$ is the momentum, Ω is the vibrational frequency of the fundamental mode of the system, m is the mass of the molecule, and $\bar{q}$ is the local coordinates vector.

$$H_{vib} = \frac{\left(P^2 + \Omega^2 m^2 \bar{q}^2\right)}{2m} \tag{1.2}$$

The Hamiltonian that depends on the electromagnetic forces is H_{EB} (**equation 1.3**). This depends on the electric $\vec{E}$ and the magnetic $\vec{B}$ fields, and quantizes the radiation field present in the system as described in [9].

$$H_{EB} = \frac{\left(\vec{E}^2 + \vec{B}^2\right)}{2} \tag{1.3}$$

The interaction Hamiltonian H_{int} can be obtained from the electric displacement field $\vec{D}$, which depends on the electric permittivity $\vec{\varepsilon}$ (**equation 1.4**). The electric permittivity is a physical constant (for a linear, homogeneous and isotropic medium) that describes how much the molecules oppose to an external electric field. The electric permittivity can also be expressed by means of the electric susceptibility $\vec{\chi}$. This constant describes the degree of polarization of a dielectric material in response to an applied electric field (*i.e.* describes the tendency of a material to polarize). ε_0 is the vacuum permittivity and $\vec{P}$ the polarization density.

$$\vec{D} = \vec{\varepsilon} \cdot \vec{E} = \varepsilon_0 (1 + \vec{\chi}) \cdot \vec{E} = \varepsilon_0 \vec{E} + \varepsilon_0 \vec{\chi} \vec{E} = \varepsilon_0 \vec{E} + \vec{P} \tag{1.4}$$

However, for a nonlinear anisotropic medium $\vec{\varepsilon}$ is dependent on the position within the medium and the angular frequency of the incident radiation. Therefore, it has a time dependent response. Thus $\vec{P}$ can be expressed in terms of the electric dipole moment $\vec{p}$ as follows:

$$\vec{P}(t) = \varepsilon_0 \vec{\chi}(t) \vec{E}(t) = N\vec{p}(t) = N\vec{\alpha}(t)\vec{E}(t) \tag{1.5}$$

where $\vec{\alpha}$ is called the molecular polarizability and *N* is the number of molecules per volume unit, present in the system. Then the interaction Hamiltonian H_{int} between the dipole moment $\vec{p}$ and the external electric field results in **equation 1.6**.

$$H_{\text{int}} = \vec{E} \cdot \vec{p}(t) = \vec{E}(t) \cdot \vec{\alpha}(t)\vec{E}(t) \tag{1.6}$$

From **equation 1.6** it is possible to apply the perturbation theory to first order approximation using the electric dipole [10]:

$$\vec{\alpha}(t) = \alpha_0 + \left(\frac{\partial \vec{\alpha}}{\partial \vec{q}}\right)_0 q(t) \tag{1.7}$$

It is possible to express the molecular polarizability $\vec{\alpha}$ as a function of general coordinates vector $\vec{q}(t)$. **Equation 1.7** describes the molecular vibration versus time. Therefore, the interaction Hamiltonian can be expressed as

$$H_{\text{int}} = \vec{E}(t) \cdot \vec{p}(t) = \vec{E}(t) \cdot \vec{\alpha}(t)\vec{E}(t) = \underbrace{\vec{E} \cdot \alpha_0 \vec{E}}_{I} + \underbrace{\left(\frac{\partial \vec{\alpha}}{\partial \vec{q}}\right)_0 \vec{E} \cdot \vec{q}(t)\vec{E}}_{II} \tag{1.8}$$

The term I of the **equation 1.8** represents the elastic scattering (*e.g.* Rayleigh scattering) and the term II represents the inelastic scattering: spontaneous Raman scattering (RS). If we express the electric field as $\vec{E}(\omega,t) = \vec{E}_0 e^{i\omega_p t}$, where ω_p is the frequency of the incident light. The general coordinates vector $\vec{q}(t)$ can be also be expressed as $\vec{q}(t) = \vec{q}_0 e^{\pm i\Omega t}$, where Ω is the frequency of molecular oscillation. The polarization in terms of the dipolar moment is [11]:

$$\vec{P}(t) = N \cdot \vec{p}(t) = N\left(\alpha_0 \vec{E}_0 e^{i\omega_p t} + \left(\frac{\partial \vec{\alpha}}{\partial \vec{q}}\right)_0 q_0 \vec{E}_o e^{i(\omega_p \pm \Omega)t}\right) \tag{1.9}$$

In **equation 1.9** it is possible to appreciate the Raman Scattering as an interaction between pump photons with energy $E = \hbar\omega_p$ and an arrangement of molecules with a system of states E_1 (equilibrium state) and E_2 (vibrant state) as in **figure 1.2**. When photons interact with the material, the system could be excited to virtual states (*E_3* or *E_4*)**.** The energy gap of the virtual state $\left(E_3 = E_1 + \hbar\omega_p\right)$ depends on the frequency of the light source ω_p. If the molecule decays from this state to the vibrant state (*E_2*), this will inelastically scatter light (Stokes shift) as a spontaneous Raman scattering as shown in **figure 1.2a.** If it returns to the equilibrium state (*E_1*), then it is an elastic scattering *(*Rayleigh scattering).

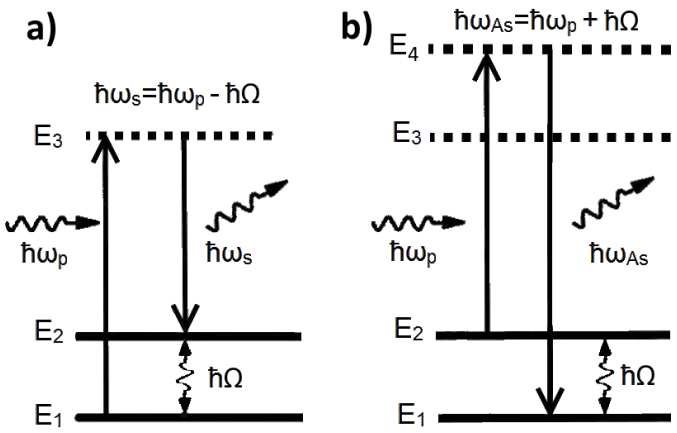

Figure 1.2 Energy diagram for Raman Scattering process. a) Stokes shift; b) anti-Stokes shift.

The frequency of the scattered photon ω_s (Stokes wave) is lower than the frequency of the incident photon, whose energy is $\hbar\omega_s = \hbar(\omega_p - \Omega)$. The excess of energy is transferred to the molecule in the form of kinetic energy, reinforcing the vibrations of the molecular bonds (*e.g.* stretching or bending). **Figure 1.2b** shows the anti-Stokes shift. In this process, the material is in a higher energy vibrating mode E_2 and hence the incident photon excites this state to a virtual state E_4, $(E_4 = E_2 + \hbar\omega_p)$, and when returning to ground state (E_1) the frequency and the energy of the scattered photon will be greater than the incident photon $\hbar\omega_{As} = \hbar(\omega_p + \Omega)$. Then the system loses or provides energy $(\hbar\Omega)$ to the scattered photon (*i.e.*, the system gets cooled).

Since the inelastic scattering processes (Stokes and anti-Stokes shifts) are temperature dependent they are governed by the Boltzmann distribution as $\exp(-(\pm\hbar\omega_s)/k_B T)$, where k_B is the Boltzmann constant and T is the absolute temperature. In a state of thermal equilibrium, the population of the initial state E_1 is higher compared to the vibrational state E_2 so the probability for a Stokes shift is much higher than for the anti-Stokes shift. Therefore, the spontaneous Raman scattering is dominated by the Stokes shifts [12]. Furthermore, the anti-Stokes process is enhanced with increasing temperature and may occur that the probability for anti-Stokes would be comparable to Stokes. However, at low temperatures Stokes-shifts probability can only increase to a certain constant value while the probability for the anti-Stokes decays to nearly zero, since it requires an initially populated excited vibrational state [10].

1.3 Stimulated Raman scattering

Spontaneous Raman scattering (RS) only occurs when an incident signal has low intensity levels, **figure 1.3a**. In this situation molecules contribute to the scattering process by vibrating independently and thus the scattered light is non-directional. But when the intensity level is increased, molecules can be considered as an array of vibrating oscillators that generate photons aligned in phase and behave coherently, **figure 1.3b**. This process is the stimulated Raman scattering (SRS). This leads to an exponential growth of the total scattered light, once the incident power exceeds a threshold value, which is dependent on the length of the medium.

The SRS is emitted in the forward or backward directions, with spectral linewidth narrower than the spontaneous linewidth [13]. The Raman scattering is a phenomenon that should be considered as one step process, in which three routes occur simultaneously: absorption of the incident photon, emission of the scattered photon and transition of the molecule to an excited state. This makes SRS possible when a sufficient number of Stokes photons are created. The energy of the emitted photon is determined by the material as $E_1 + \hbar\omega_p = \hbar\Omega + \hbar\omega_s = E_2 + \hbar\omega_s$ [10].

The anti-Stokes signal is often produced by nonlinear effects, like the four-wave mixing (FWM) and/or two photon absorption (**figure 1.3c**), arising when different frequency components propagate together in the media. When the interaction between the relative phases of all the beams fulfills the condition of phase-matching, this process leads to amplification and/or creation of a different frequency. When the frequency difference between these signals is equivalent to the molecular vibration of the medium (**figure 1.3d**) ($\omega_p - \omega_s = \Omega$ and $\omega_{as} - \omega_p = \Omega$); with $\Omega = 12\times10^3 GHz - 15\times10^3 GHz$, the process is resonantly intensified, referred as the coherent anti-Stokes Raman scattering (CARS).

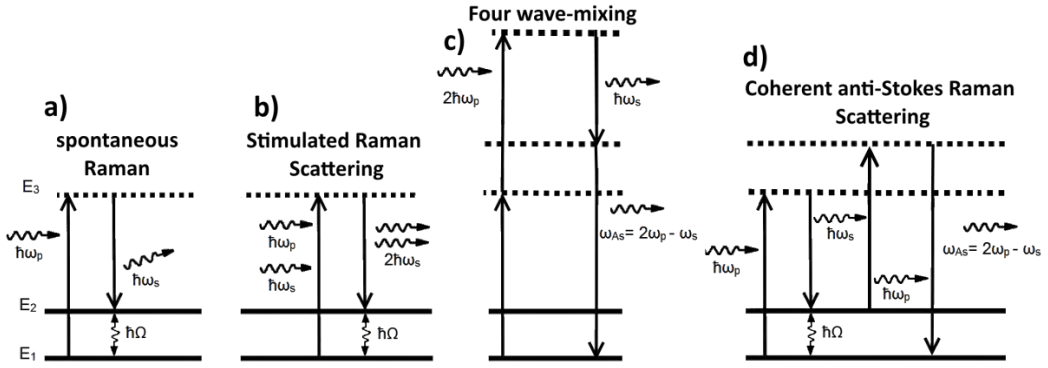

Figure 1.3 Raman scattering processes: a) RS, b) SRS, c) FWM, and d) CARS.

1.4 Raman gain spectrum

The Raman scattering in silica-based fibers arises from the vibrational states in the molecules present in the fiber (as described in the previous section). Several vibrational modes occur in this structure (SiO_2 as shown in **figure 1.4**). The contribution of these vibrational modes and the broadening effects produce the Raman gain spectrum (**figure 1.5**). The Raman gain spectrum is the intensity of the Stokes wave as a function of the Raman shift (frequency shift $\Delta\omega = \omega_p - \omega_s$), *i.e.*, the frequency difference between pump and the Stokes shift [14]. This depends on the decay time related to the excited vibrational state. As a result, the Stokes waves (ω_s) depend on the pump frequency (ω_p) [15]. The Raman gain spectrum can be determined by direct measurement of the gain experienced by a Stokes wave through SRS after propagating through a medium.

The Raman gain (for silica) extends up to 45 THz frequency range (1500 cm^{-1}) and its bandwidth is $\Delta\nu_R$≈14 THz where the maximum Raman gain is at 13.2 THz (440 cm^{-1}). The broadband (*i.e.*, the vibrational energy levels of silica molecules form a band) and multipeak nature of the spectrum is due to the amorphous nature of glass. The conversion between cm^{-1} to Hz is $f(Hz) = c \cdot f(cm^{-1})$ where c is the speed of light (3×10^8 m/s).

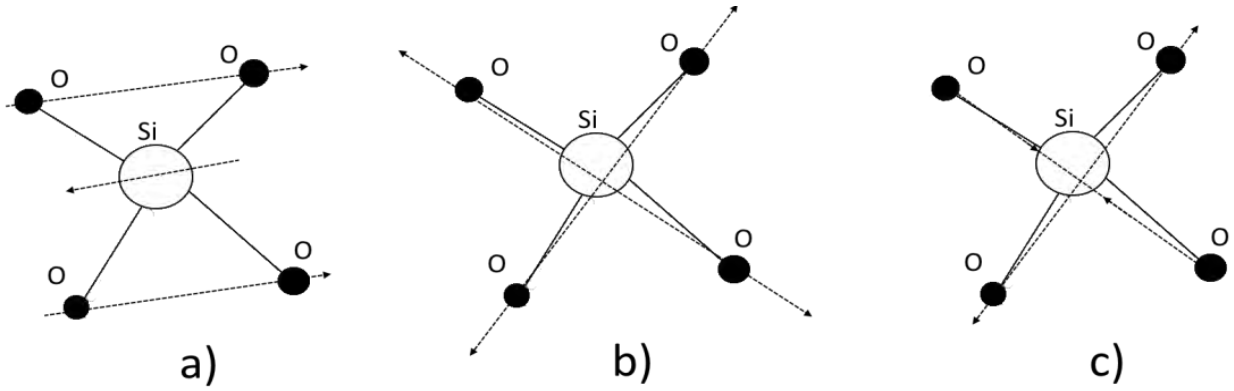

Figure 1.4 Silica (SiO_2) molecule modes; a) “rigid cage” mode emitting at 1065cm^{-1} (32 THz), b) “breathing” mode emitting at 800cm^{-1} (24 THz), c) “transverse” mode emitting at 440 cm^{-1} (13.2 THz) and “longitudinal” mode emitting at 490 cm^{-1} (14.7 THz) [16].

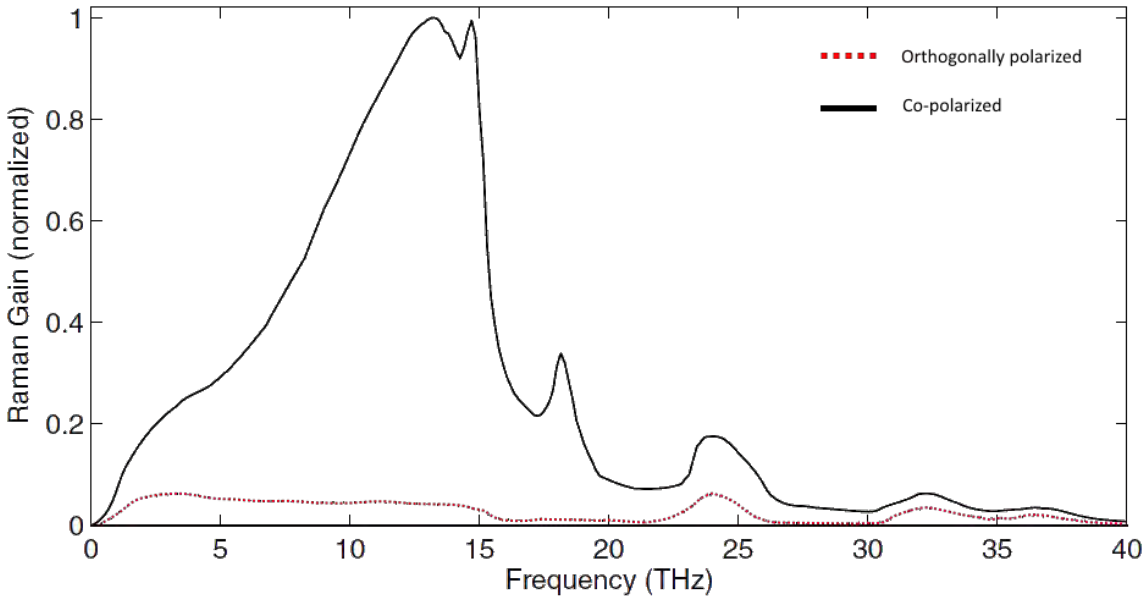

Figure 1.5 Raman gain spectrum of fused silica when pumped at ~1000 nm. When signals (pump and Stokes), are co-polarized and orthogonally polarized [15].

The Raman gain coefficient g_r [m/W] is related to optical gain $g(z)$ as [15]:

$$g(z) = g_r I_P(z) = \frac{g_r P_P(z)}{A_{eff}(\lambda_p)} = G_R P_p(z) \qquad 1.10$$

where I_p is the pump intensity, P_p is the pump power, and A_{eff} is the effective core area $A_{eff} = \pi \cdot W_0^2$ $[m^2]$, W_0 corresponds to the mode field area (see **equation 1.16**); which interacts with the pump beam along an optical fiber. The Raman gain efficiency is defined as $G_R = g_r / A_{eff}$ [$m^{-1}W^{-1}$].

The small signal gain is defined in **equation 1.11** [15],

$$g_0 = g_r I_P(0) * \left(\frac{L_{eff}}{L}\right) = \frac{g_r P_P(0)}{A_{eff}(\lambda_p)} = G_R P_p(0) \left(\frac{L_{eff}}{L}\right) \qquad 1.11$$

where L is the fiber length, L_{eff} is the effective length ($L_{eff} = \frac{[1-\exp(-\alpha L)]}{\alpha}$) which depends on the attenuation coefficient $\alpha(\lambda)$, **equation 1.12**:

$$L_{eff} = \frac{1-\exp(-\alpha L)}{\alpha};\ \lim_{\alpha >> 1}\ L_{eff} = \frac{1}{\alpha};\ \lim_{\alpha \to 0}\ L_{eff} = L \qquad 1.12$$

1.5 Propagation equations for Raman scattering along an optical fiber

When an optical fiber (usually Ge- or P- doped silica fiber) is pumped with high powers (in order of tens of W), the generation of SRS is produced and this scattered light (Stokes signals) propagates along the fiber at both directions (back and forward). Let us assume a system with only forward-propagation as in **figure 1.6,** a set of differential equations that describe the forward propagation of the pump (P_p) and first Stokes (P_s) are defined as:

$$\frac{dP_p}{dz} = \frac{-g_s}{A_{eff\,s}}\frac{\lambda_s}{\lambda_p}P_sP_p - \alpha_pP_p \qquad 1.13$$

$$\frac{dP_s}{dz} = \frac{g_s}{A_{eff\,s}}P_pP_s - \alpha_sP_s \qquad 1.14$$

where g_s is the Raman gain coefficient corresponding to first Stokes, A_{effs} is the effective area of the first Stokes, α_p and α_s are the pump and first Stokes values of the intrinsic loss [m^{-1}] of the host glass (*i.e.*, attenuation coefficients) at each particular wavelength (λ_p and λ_s [m]).

To describe the following order Stokes propagation, we will require calculating a system of equations from the following [17-19]**:**

$$\frac{dP_{n-1}}{dz} = \frac{-g_n}{A_{eff\,n}}\frac{\lambda_n}{\lambda_{n-1}}P_{n-1}P_n - \alpha_{n-1}P_n \qquad 1.15$$

$$\frac{dP_n}{dz} = \frac{g_n}{A_{eff\,n}}P_{n-1}P_n - \alpha_nP_n \qquad 1.16$$

In this set of **equations** (**1.15 – 1.16)**, *n=2, 3,..,N* where *N* is the maximum Stokes wave order; *e.g.*, for N=4 (up to the fourth Stokes wave), we will get a system of eight equations.

The stimulated Raman gain coefficient is given by g_n in [m/W] (**equation 1.16**). It varies inversely with wavelength (λ_n), and is approximately proportional to $1x10^{-13}$ [m/W] (the exact value is $0.9856x10^{-13}$ m/W) at 1μm for silica. When a fiber is pumped at 1550 nm this value is ~ $6\ x10^{-13}$ [m/W].

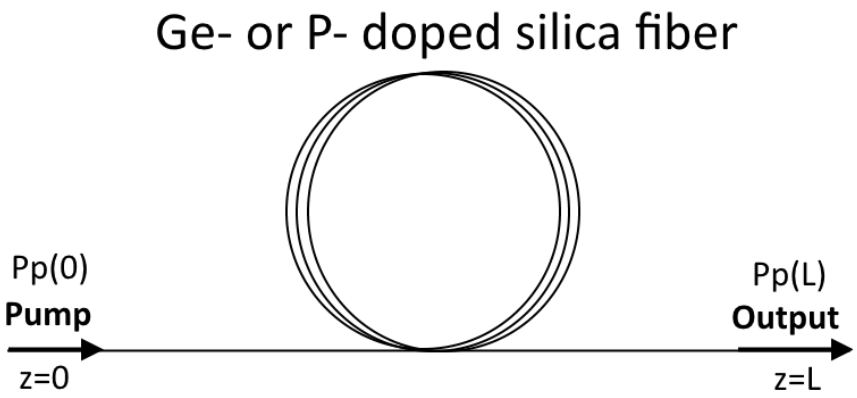

Figure 1.6 Forward propagation in silica fiber.

The effective core area A_{eff} [m^2] is defined as

$$A_{eff} = \pi \cdot W_0^2 = \pi \cdot \left(a\left(0.65 + \frac{1.619}{V_n^{3/2}} + \frac{2.879}{V_n^6} \right) \right)^2 \ [m^2] \qquad 1.17$$

where a corresponds to the core radius, V_n is the normalized frequency (**equation 1.18**). Where NA is the numeric aperture, and n_1 and n_2 are the core and cladding refractive index, respectively.

$$V_n = \frac{2\pi a \cdot NA}{\lambda_n} = \frac{2\pi a \cdot \sqrt{n_1^2 - n_2^2}}{\lambda_n} \qquad 1.18$$

Boundary conditions for the pump power at the input ($z = 0$) and at the output ($z = L$) of the fiber are given by:

$$P_p(0) = P_{in} \qquad 1.19$$

$$P_p(L) = \exp(-\alpha_p \cdot L) \cdot P_{in} \qquad 1.20$$

This is a solution for a system of two equations (*i.e.*, just first Stokes is generated), when considering the case of small-signal amplification for which pump depletion can be neglected. Also supposing $\alpha = \alpha_p = \alpha_s = \frac{\alpha_s + \alpha_p}{2}$ [17, 19] in the **equation 1.14** we can substitute it in the **equation 1.20**. Then, the signal power (Stokes wave) at the output of an amplifier of length L is given by:

$$P_1(L) = P_1(0)\exp\left[\frac{g_R P_{in}}{A_{eff\,1}} \cdot \left(\frac{1 - \exp(-\alpha_p \cdot L)}{\alpha_p} \right) - \alpha_s \cdot L \right] = P_1(0)\exp(G_R P_{in} \cdot L_{eff} - \alpha_s \cdot L)$$

$$P_1(L) = P_1(0)\exp\left(\frac{G_R P_{in}}{\alpha_p} - \alpha_s L\right) \qquad 1.21$$

For the (n-th) Stokes waves power at the boundary condition (L=0), the following relation can be used [20],

$$P_i(0) = h\lambda_i \mathrm{B}_{\mathrm{eff}_i} \approx 10^{-7} \cdot P_{in} \qquad 1.22$$

B_{eff_i} is the Stokes wave bandwidth, centered at the gain peak $\left(G_R = g_r / A_{eff}\right)$; it depends on the intensity of the pump and the fiber length [16]:

$$B_{eff\ j} = \frac{\Delta\nu_R}{2}\left[\frac{\pi \cdot A_{eff_j}}{g_R P_{in} L_{eff_j}}\right]^{1/2} \quad \text{where} \quad \Delta\nu_R = 13.2\,\mathrm{THz} - 14\,\mathrm{THz} \qquad 1.23$$

Then the nonlinear differential equation set (**1.13** to **1.16**) can be solved numerically by the Runge-Kutta method. The solutions can be used for modeling the power propagation of the pump and the Stokes waves along the optical fiber as shown in **figure 1.7**.

The intensity of the stimulated scattered light grows exponentially once the incident pump power exceeds a certain value. This value is considered as critical pump power level P_{cr}. This is defined as the incident coupled power such that the Stokes signal and the residual power are equal. This is $P_p(L)=P_1(L)=P_0\exp(-\alpha_p L)$ [21].

Then the critical pump power satisfies the condition [15,20,22],

$$P_{cr} \approx \frac{\ln\left(P_{in}/P_1(0)\right)\cdot A_{eff}}{g_R \cdot L_{eff}} = \frac{\ln\left(10^7\right)\cdot A_{eff}}{g_R \cdot L_{eff}} = \frac{16 \cdot A_{eff}}{g_R \cdot L_{eff}} \cong \frac{16 \cdot \alpha}{G_R} \qquad 1.24$$

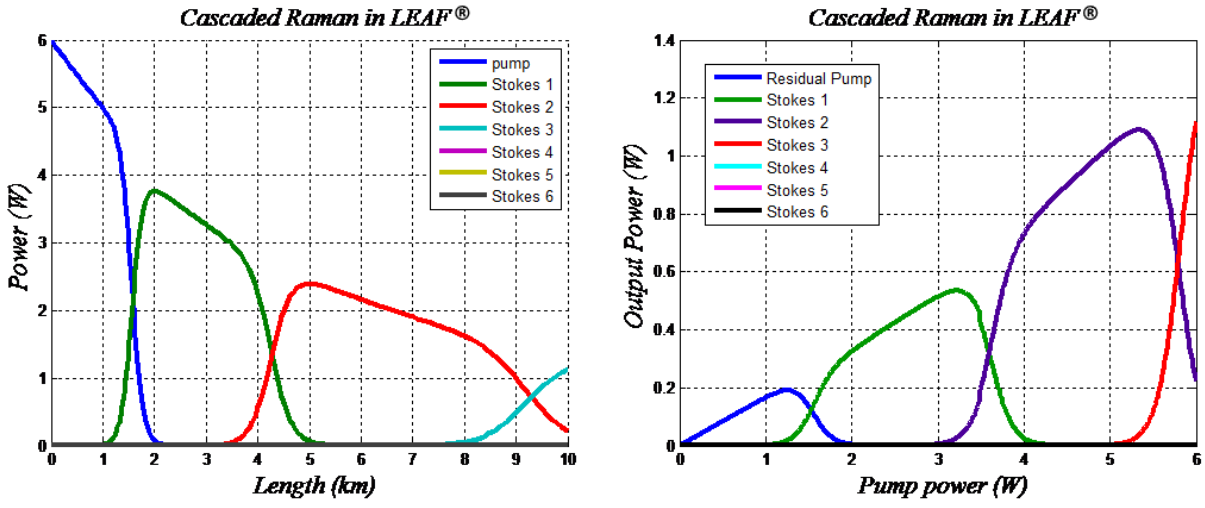

Figure 1.7 Stokes waves power propagation along an optical fiber (10 km Corning® LEAF®®optical fiber pumped with 6 W power).

1.6 Propagation equations for a cascaded Raman fiber laser

The SRS in cascaded Raman fiber lasers (RFLs) (**figure 1.8**) is governed by a set of nonlinear differential equations that describe the pump power and the SRS propagation in both, forward and backwards directions (**equation 1.25** to **equation 1.27**). Spontaneous Raman scattering has been neglected because it is assumed that Raman oscillation is dominant, and that all the fields are unpolarized and that axial symmetry exists [17, 23].

$$\frac{1}{P_p^+}\frac{dP_p^+}{dz} = \frac{1}{P_p^-}\frac{dP_p^-}{dz} = \frac{-g_1}{A_{eff\,1}}\frac{\lambda_1}{\lambda_p}P_1^{\pm} - \alpha_p \qquad 1.25$$

$$\frac{1}{P_i^+}\frac{dP_i^+}{dz} = \frac{1}{P_i^-}\frac{dP_i^-}{dz} = \frac{g_i}{A_{eff\,i}}P_{i-1}^{\pm} - \frac{g_{i+1}}{A_{eff\,i+1}}\frac{\lambda_{i+1}}{\lambda_n}P_{i+1}^{\pm} - \alpha_i \quad i = 1 \text{ to } n-1 \qquad 1.26$$

$$\frac{1}{P_n^+}\frac{dP_n^+}{dz} = \frac{1}{P_n^-}\frac{dP_n^-}{dz} = \frac{g_n}{A_n}P_{n-1}^{\pm} - \alpha_n \qquad 1.27$$

The subscripts ($P_j \;\; j = p,i,n$) refer to the pump and the Stokes waves power [W], respectively. The positive and negative superscripts represent the forward- and backward-propagating pump and Stokes waves. ($\lambda_j \;\; j = p,i,n$) are the wavelengths correspondent to pump, and stokes waves, respectively.

Then boundary conditions are applied for the *i-th* and *n-th* order cascaded RFL. At the input end of the fiber, these are given by:

$$P_p(0) = P_{in} \qquad 1.28$$

$$P_j^{\pm}(0) = P_j^+(0) = R_j^- P_j^-(0) \quad \text{For j} = 1 \text{ to } n-1 \qquad 1.29$$

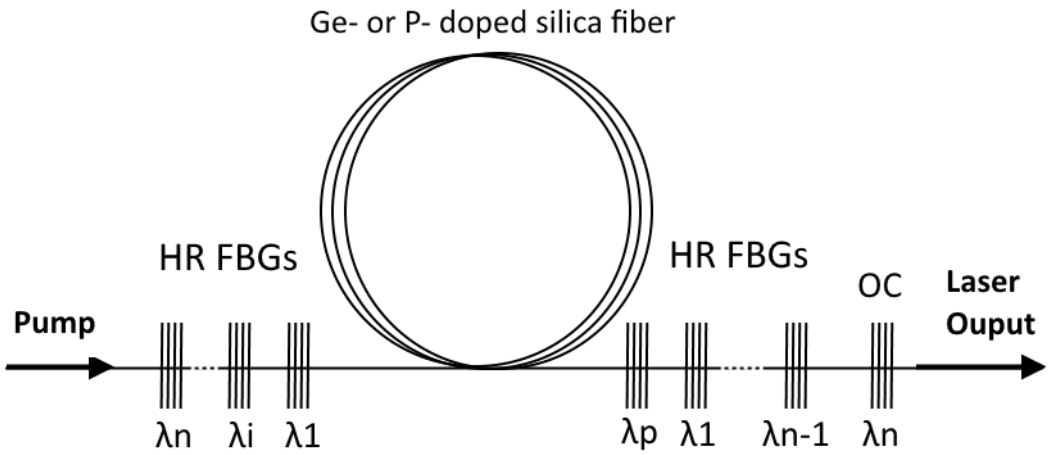

Figure 1.8 Diagram of a cascaded Raman fiber laser.

At the output end of the fiber, the boundary conditions are given by:

$$P_p(L) = R_p P_p(L) = R_p(\exp(-\alpha_p \cdot L) \cdot P_{in} \quad 1.30$$

$$P_j^{\pm}(L) = P_j^{-}(L) = R_j^{+} P_j^{+}(L) \quad \text{For j} = 1 \text{ to } n \quad 1.31$$

Typically, the only reflectivity coefficient that is not close to 1 (high reflecting FBGs is R_n^+, since it corresponds to the output coupler (OC) in **figure 1.8**.

Under steady-state conditions, these equations form the well-known system of first-order, nonlinear boundary-value ordinary differential equations, with separated boundary conditions. For the j-th Stokes wave power the boundary condition at *L=0*, the **equation 1.22** can be applied.

1.7 Raman fiber lasers and amplifiers

RFLs and amplifiers have many advantages, since Raman gain is present basically in all fibers (it depends on the optical fiber's composition); e.g., for Silica, within the 0.3 μm – 2 μm region [24], since the Raman gain is available in the entire transparency region (**figure 1.9)**. Unlike Erbium doped fiber amplifiers (EDFAs), whose operation window is about 4.5 THz (1530 nm –1565 nm), RFLs and amplifiers have the potential to operate in more than twice the range of the EDFAs in the transparency window. Another feature of the Raman gain is that it depends on pump wavelength; by using two or more pump wavelengths it is possible to extend the Raman gain bandwidth. Also, Raman amplification is a relatively broadband process with a bandwidth >5 THz.

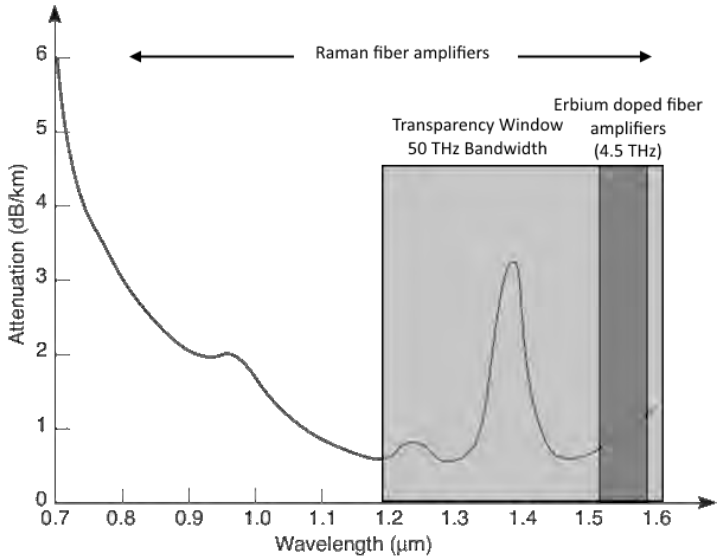

Figure 1.9 Attenuation versus wavelength for a typical fused silica fiber [24].

There are also some drawbacks for RFLs and amplifiers. These systems often require long gain media (fiber lengths are cents of meters). Furthermore, Raman gain is polarization dependent, it can be optimized when signals (pump and Stokes) have the same polarization and diminishes when both are orthogonally polarized (**figure 1.5)**.

In recent years RFLs and amplifiers are gaining popularity. The improvement and development of high pump power laser diodes or cladding-pump fiber lasers as well as the development and availability of all-fiber components like the FBGs and wavelength division multiplexors (WDMs) make RFLs and amplifiers more robust and compact systems, making them more attractive for most applications.

1.8 Special fiber based Raman lasers and amplifiers

Special fibers with much higher Raman gain and (or) various Raman frequency shifts are often used for Raman fiber lasers, even despite of all the features that silica-based Raman fibers have. Hence, many investigations for obtaining new glasses that enhance Raman gain features have been implemented. It was discovered that glasses containing heavy-metal oxides (Sb_2O_3-GeO_2 and Sb_2O_3-As_3O_2) have very high Raman cross-sections, approximately 30 times exceeding SiO-GeO_2 [24].

In the 1980s, it was found that Germania glass (GeO_2), has the highest cross-section among doped-glasses (420 cm^{-1} frequency shift), approximately nine times that of silica. Another interesting glass was the vitreous P_2O_5 (Phosphate glass) that has two Raman frequency shifts (650 cm^{-1} and 1300 cm^{-1}); the cross sections for these bands are 5.7 and 3.5 times higher than silica. Due to manufacturing, binary glasses (Phosphosilicate SiO_2-P_2O_5), that have enough Raman gain and often-shown new bands, were also investigated.

These show that the band corresponding to 650 cm^{-1} was attenuated whereas the 1300 cm^{-1} stayed strong (**figure 1.10**). The obtained results showed that low-loss P_2O_5-doped silica fibers could be considered as promising high-gain Raman fibers. However, fabrication of these fibers also presented some difficulties, as different thermal expansion coefficients and melting temperatures. It was discovered that together with these defects, the loss coefficient of these fibers grows considerably with increasing P_2O_5 contents.

For compensating these difficulties, the development and effectiveness of continuous wave (CW) cascaded Raman fibers intensely encouraged the research for developing lasers and amplifiers in the 1.3 μm window. These systems usually make a more efficient conversion of pump to Stokes waves, since these cavities are considered a low-loss cavity

system. These systems are comprised by a set of FBGs that provide high reflectivities for each of the intermediate Stokes waves, and several hundred meters of germanosilicate optical fiber. An example of this, is the cascaded RFL (**figure 1.8**), which ends with an OC FBG with reflectivity ~20% that extracts the output power of the desired wavelength. The cascaded RFLs pumped with LDs are very efficient systems for the 1.2 μm 1.6 μm region. These could be applied to pump diverse optical amplifiers.

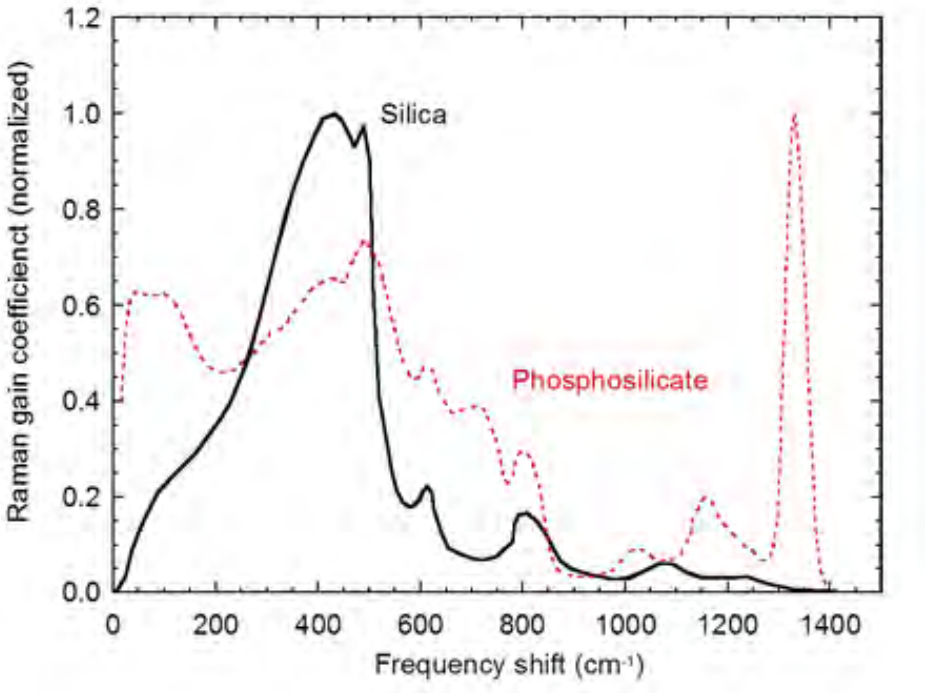

Figure 1.10 Normalized Raman gain spectra of silica fiber and phosphosilicate fiber [25].

1.9 Distributed Raman vs. discrete REs doped amplifiers

For longer fiber-optic links as used for long-line data transmission, one or several fiber amplifiers are usually needed for obtaining a sufficiently high signal power at the receiver. For this situation, a short classification for RFLs and amplifiers can be applied: the distributed and the discrete Raman amplifiers.

In many cases, such amplifiers are *discrete* amplifiers. These systems use some assisting doped-fibers, often of a few meters of some rare-earth-doped fiber (REDF); which provide additional gain. Discrete amplifiers are pumped with fiber-coupled LDs and used as part of the transmitter, or somewhere between parts of the transmission fiber. In these systems most of the power is confined within the REDF.

However, it is also possible to employ so-called *distributed* amplification, where the pump power extends within a long length of the transmission Raman gain fiber itself. Here, the pump power (typically high-power pumps) is typically injected at the receiver or transmitter end, or from both directions (counter-propagating pumps). Such a distributed amplifier may have a similar overall gain, where Raman gain is used to obtain amplification, but much lower gain is obtained per unit length. It is meant to approximately maintain a reasonable signal power level in the presence of propagation losses, rather than increasing the power level by tens of decibels. So, these systems do not require high signal levels and consequently the nonlinear effects are reduced.

1.10 References

1. A. Smekal, "Zur Quantentheorie der Dispersion," Naturwissenschaften 11, 873–875 (1923).
2. C. V. Raman and N. S. N. Nathe, "The diffraction of light by high frequency sound waves: Part I.," Proc. Indian Acad. Sci. - Sect. A 2, 406–412 (1935).
3. G. Eckhardt, R. W. Hellwarth, F. J. McClung, S. E. Schwarz, D. Weiner, and E. J. Woodbury, "Stimulated Raman Scattering From Organic Liquids," Phys. Rev. Lett. 9, 455–457 (1962).
4. G. Landsberg and L. Mandelstam, "Eine neue Erscheinung bei der Lichtzerstreuung in Krystallen," Naturwissenschaften 16, 558 (1928).
5. W. Hayes and R. Loudon, Scattering of Light by Crystals, First Edit (Dover Publications, Inc., 2012).
6. J. Bromage, "Raman Amplification for Fiber Communications Systems," J. Light. Technol. 22, 79–93 (2004).
7. R. W. Hellwarth, "Theory of Stimulated Raman Scattering," Phys. Rev. 130, 1850–1852 (1963).
8. K.-H. Chen and Kuei-Hsien, "Spontaneous Raman and Coherent Anti-Stokes Raman Spectroscopy of Infrared Multiphoton-Excited Molecules.," Thesis (PH.D.)--HARVARD Univ. 1989.Source Diss. Abstr. Int. Vol. 50-12, Sect. B, page 5696. (1989).
9. Y. R. Shen and N. Bloembergen, "Theory of stimulated Brillouin and Raman scattering," Phys. Rev. 137, A1787–A1805 (1965).
10. S. P. Singh, R. Gangwar, and N. Singh, "Nonlinear Scattering Effects in Optical Fibers," Prog. Electromagn. Res. 74, 379–405 (2007).
11. M. a. Farahani and T. Gogolla, "Spontaneous Raman scattering in optical fibers with modulated probe light for distributed temperature Raman remote sensing," J. Light. Technol. 17, 1379–1391 (1999).
12. R. L. Sutherland, Handbook of Nonlinear Optics (2003), Vol. 36.
13. C.-S. Wang, "Theory of Stimulated Raman Scattering," Phys. Rev. 182, 482–494 (1969).
14. J. M. Baptista, J. C. W. a. Costa, a. P. Barbero, M. a. G. Martinez, H. M. Salgado, M. B. Marques, M. T. M. Rocco Giraldi, C. Correia, and O. Frazao, "Stimulated Raman Scattering and its Applications in Optical Communications and Optical Sensors," Open Opt. J. 3, 1–11 (2009).

15. G. P. Agrawal, "Fiber-Optic Communication Systems, 4th Edition," in Fiber-Optic Communication Systems, 4 th (2011), pp. 1–600.

16. J. A. Buck, Fundamentals of Optical Fibers (John Wiley & Sons, 2004).

17. L. de la Cruz May, M. May Alarcón, F. Méndez, M. L. Estrella Rosas, M. J. Vázquez López, and P. Mollinedo, "Approximate determination of the maximum power stored in Stokes lines generated in silica fibers," Opt. pura y Apl. ISSN-e 2171-8814, Vol. 46, N^{o}. 1, 2013 (Ejemplar Dedic. a Mex. Opt. Photonics Meet. 2012 - MOPM), págs. 7-12 46, 7–12 (2013).

18. L. de la Cruz-May, E. B. Mejía, O. Benavides, D. V Talavera, and J. Vasquez-Jimenez, "Exact determination of scaling of the Raman gain efficiency in silica fibers," Laser Phys. 23, 55103 (2013).

19. L. De La Cruz-May, J. A. Alvarez-Chavez, E. B. Mejia, A. Flores-Gil, F. Mendez-Martinez, and S. Wabnitz, "Raman threshold for nth-order cascade Raman amplification," Opt. Fiber Technol. 17, 214–217 (2011).

20. Y. Murakami, K. Noguchi, F. Ashiya, Y. Negishi, and N. Kojima, "Maximum Measurable Distances for a Single-Mode Optical Fiber Fault Locator Using the Stimulated Raman Scattering (SRS) Effect," IEEE Trans. Microw. Theory Tech. 30, 1461–1465 (1982).

21. J. M. Baptista, J. C. W. A. Costa, A. P. Barbero, M. A. G. Martinez, H. M. Salgado, M. B. Marques, M. T. M. Rocco Giraldi, C. Correia, and O. Frazao, "Stimulated Raman Scattering and its Applications in Optical Communications and Optical Sensors," Open Opt. J. 3, 1–11 (2009).

22. S. D. Jackson and P. H. Muir, "Theory and numerical simulation of nth-order cascaded Raman fiber lasers," J. Opt. Soc. Am. B 18, 1297 (2001).

23. B. Burgoyne, N. Godbout, and S. Lacroix, "Theoretical analysis of nth-order cascaded continuous-wave Raman fiber lasers. I. Model and resolution," J. Opt. Soc. Am. B 22, 764 (2005).

24. M. N. Islam, Raman Amplifiers for Telecommunications 1 Physical Principles, Springer Series in Optical Sciences (Springer New York, 2003), Vol. 90/1.

25. M. Chen, A. Shirakawa, X. Fan, K. Ueda, C. B. Olausson, J. K. Lyngsø, and J. Broeng, "Single-frequency ytterbium doped photonic bandgap fiber amplifier at 1178 nm," Opt. Express 20, 21044 (2012).

Chapter 2

Energy transfer mechanisms in a RFL under different cavity configurations

Chapter 2

2. *Energy transfer mechanisms in a Raman fiber laser*

2.1 Abstract

We report an experimental study of the signals delivered by a two Stokes cascaded Raman fiber laser under different output coupling conditions. Our main results let us to conclude that feedback reflectivity variations have a great influence on Stokes to Stokes energy-transfer mechanisms. It is also confirmed that, although for lower feedback the high threshold for Stokes generation is not satisfactory, the conversion efficiency does; the contrary occurs for high-reflective output coupling cavities.

2.2 Introduction

Stimulated Raman scattering (SRS) has been the subject of intense theoretical and experimental research during the past 20 years in the fields of nonlinear optics and optical fibers. The SRS phenomenon is very effective for generating and/or amplifying optical signals in the wavelength region of 1.1 μm 1.7 μm. This is useful for improving the performance in long–range optical communications links, to amplify wavelength-division-multiplexed signals, signal processing, laser spectroscopy, and sensing systems; as well as for medical applications such as in the fields of dermatology and ophthalmology [1-5].

In the early 1980's, the potential for fiber lasers and amplifiers based on SRS was first demonstrated by Stolen et al. [6]. However, it was not certain that an efficient CW pumped Raman fiber laser would be possible. Later, the advent of FBGs revolutionized the field of fiber lasers and amplifier systems; leading to the ability of constructing nested highly reflecting cavities for Raman fiber lasers. One of these cavities was first introduced by Grubb et al. [7] and consisted on pumping through one set of highly reflecting FBGs (resonant to first and the higher-order Stokes wavelengths) spliced to several hundred meters of germanosilicate fiber; at the other end, a set of FBGs completed the cavity. The purpose of such assembly is that each intermediate Raman Stokes order is contained within the cavity until its energy is entirely converted to the next higher order Stokes, and so on; *i.e.*, cascaded generation is a process in which a Stokes signal acts as a pump source for the next Stokes. Another kind of laser cavities are the random distributed feedback (RDFB) fiber lasers that operate under optical feedback provided by Rayleigh scattering caused by randomly distributed composition and/or refractive index variations

along the fiber and amplified through stimulated Raman scattering (SRS) [8]. The condition for these lasers is to have a high gain and a long medium as it is required that several very small scattered signals contribute to the total feedback [9-13].

The focus of this work consisted on investigating the conversion efficiency, the generation threshold and the energy transfer among all the signals involved (pump, Stokes and anti-Stokes) as function of cavity feedback on cascaded fiber lasers. The aim of this work is to find out whether it is worth to use several FBGs closed cavities or half open cavities. The pros and cons of each type of configuration are analyzed and discussed and, in our point of view, important conclusions have been obtained.

2.3 Experimental configurations

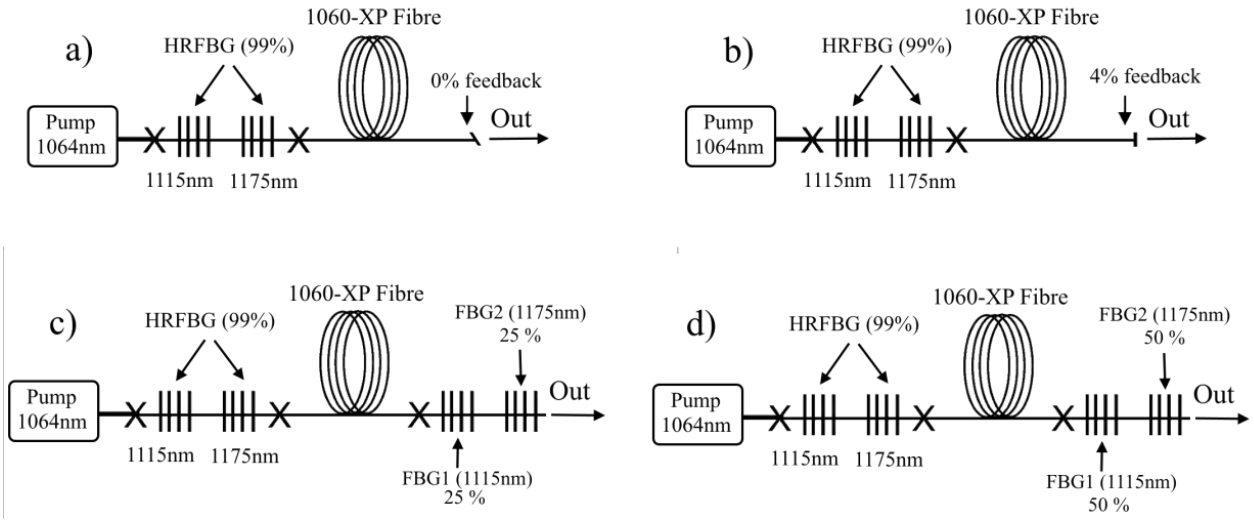

Figure 2.1 Half-open cavities a) angled cleaved, 0% feedback; b) Fresnel reflection, 4% feedback; Nested Raman fiber laser cavities, c) 25% output coupler; d) 50% reflectivity output coupler.

We investigated four experimental configurations (**figure 2.1**). A 1064 nm-pump ytterbium CW fiber laser (*IPG photonics*®) delivering up to 10 W was spliced to the HR FBGs operating as the HR-mirrors of the cavities for first and second Stokes (1115 and 1175 nm) spliced to the 1-km Raman gain fiber (*Nufern*® 1060-XP®) with g_R= 2.1 ± 0.1 $W^{-1}Km^{-1}$ [15,16]. The commercial FBGs had a ~6 μm-core diameter similar to fiber the 1060-XP fiber. Two of those configurations were half open cavities as in **figure 2.1a** and **figure 2.1b**; one with 0% feedback (an 8° angled polished connector was used to avoid the Fresnel reflection) for having RDFB laser operation; the other one used the Fresnel reflection. The other two configurations were nested cavities as shown in **figure 2.1c** and

figure 2.1d. In these, the FBGs acted as output couplers that provided much higher optical feedback for both Stokes; the reason for using identical reflectivities for both Stokes is to properly compare with the first basic cavity design; in this way, one configuration had 25% feedback and the other one 50%.

In all configurations, the pump power level was gradually increased in order for the first and second Stokes signals to be delivered. The total output power was measured with a power meter (PM) and it was distributed among all the spectral components monitored by an optical spectrum analyzer (©*Thorlabs 202*, OSA).

2.4 Results and discussion

As an example of how to obtain the output power at each component, **figure 2.2** shows the typical output spectra for 4% feedback configuration (at 6.2 W coupled pump power). From this spectrum, the area under the curve at each delivered component is associated to the power contained in it. **Equation 2.1** describes it for residual power. The total area represents the total delivered power, and is the sum of all areas contained in each spectrum. In this way, the output power of each component can be separated for further analysis of its evolution under the gradual increase in pump power; these are represented in **figure 2.3**.

$$P_{res} = \frac{(\mathrm{AREA\,1}) \cdot (\mathrm{Measured\,power\,(W)})}{\mathrm{TotalArea}}; \quad \mathrm{TotalArea} = \sum_{i=1}^{n} \mathrm{AREA\,n} \qquad 2.1$$

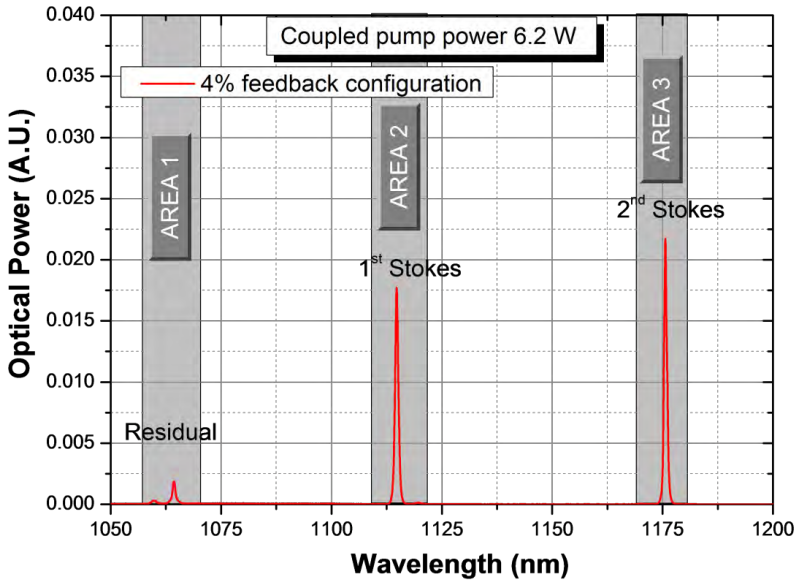

Figure 2.2 Typical output spectra for 4% feedback.

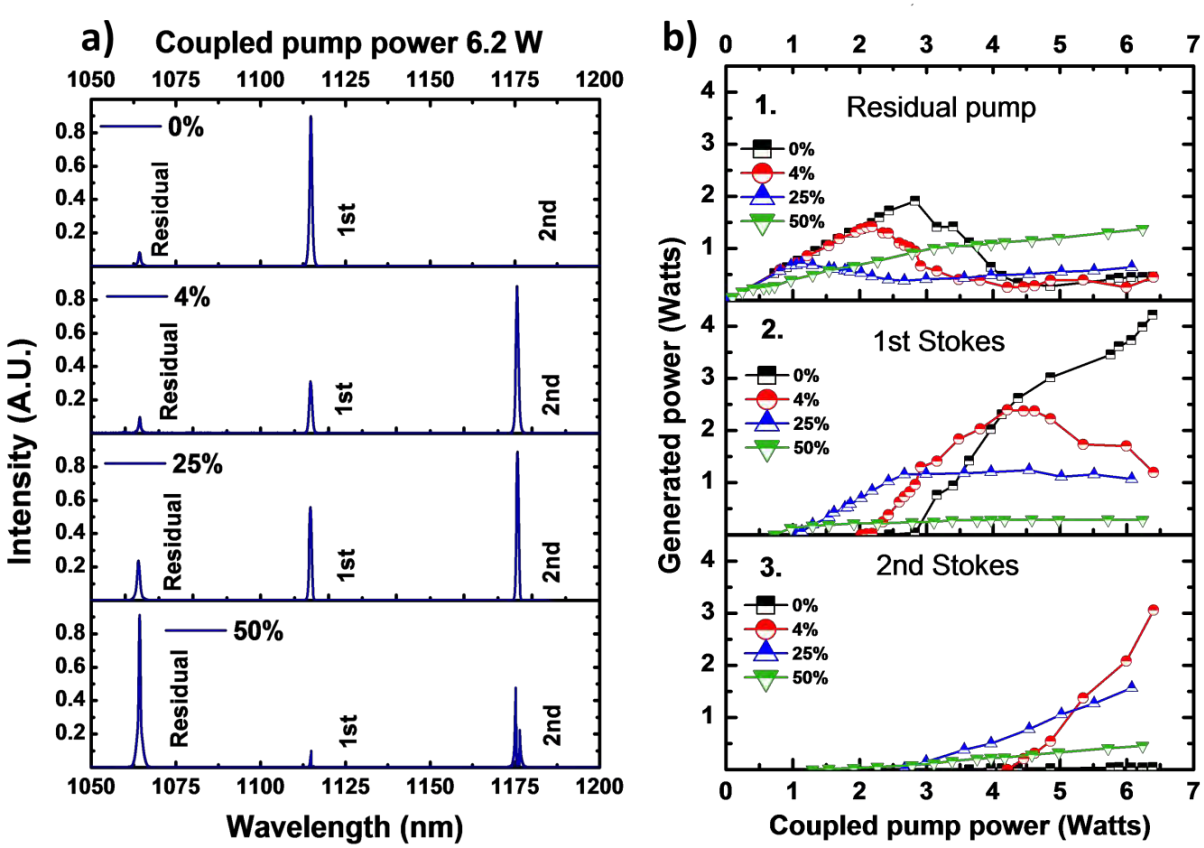

Figure 2.3 a) Output spectra for 0%, 4%, 25% and 50% feedback at 6.2W power pump; b) Energy conversion curves of residual pump, first and second Stokes for 0%, 4%, 25%, and 50% feedback configurations.

Figure 2.3 shows the pump-dependent output energies for residual pump, first and second Stokes. It is possible to observe in **figure 2.3b**, for most of the configurations, a tendency to decay for the residual pump immediately when the first Stokes is produced. A subsequent saturation occurs in first Stokes power when second Stokes is created (*i.e.*, there is an energy transfer from the first Stokes to the second one) accompanied by a gradual slight increase of the residual signal. This behavior agrees with [14]; however, this is not so clear when the feedback is higher, for 50% feedback (**figure 2.3b.1)**, where the residual pump only suffers slight slope changes when first and second Stokes appear, but in general, it continues increasing monotonically.

In **figure 2.3b** for the 0% feedback configuration, the Raman conversion efficiency (*i.e.,* the power efficiency for each corresponding Stokes component, $\eta = {}^{P_{stokes}}\!/_{P_{coupled}}$) at maximum coupled pump power (6.2 W), it was 70% for first Stokes and less than 1% corresponding to the second Stokes signal.

We observed that practically all the energy is transferred to the first Stokes; this is due to its high slope efficiency, allowing its output power to exceed all other configurations despite its higher generation threshold of 2.8 W. Since this wavelength (1115 nm) experiences lower attenuation (linear losses) than the pump wavelength, a larger number of converted photons propagate through the fiber, thus improving the efficiency [11,14]. As the threshold for second Stokes was much higher than for the other configurations, it resulted in an increased achievable output power for the first Stokes. Higher pump power or longer fiber (Raman gain) would be required for the second Stokes to fully develop.

In the case of Fresnel (4%) feedback, the maximum Raman conversion efficiency for the first Stokes was lower than in the previous case, 57% for 4.2 W coupled pump power, because the first Stokes saturates to generate the second Stokes. Nevertheless, it had an improved generation threshold of 2 W. The Raman conversion efficiency for the second Stokes was 50% at 6.2 W with a generation threshold of 4.2 W. As a consequence, there was a better energy transfer from first to second Stokes in this configuration.

For the 25% feedback configuration, the maximum Raman conversion efficiency for first Stokes was 43% at 2.7 W pump power, whereas for the second Stokes it was 26% at 6.2 W. This system exhibits better generation thresholds, 1 W for the first and 2.7 W for the second Stokes. We observed that the energy tends to be distributed among all the Stokes signals. Under this situation, contrary to our expectations, the energy transfer is poorer and is denoted by the low pump depletion. We believe that this non-satisfactory performance relies on the insertion losses added by the FBGs not to mention the Stokes energies stored inside the cavity. High intensities within the cavity can produce nonlinear spectral broadening and hence some spectral components may leak at FBGs' reflections. Additionally, the power distribution of each signal (residual pump, first and second Stokes) along the fiber, is affected due to the high reflectivity of the FBG, causing overlapping as described in [14]. This deteriorates the maximum-achievable efficiency at the output end. This configuration is appropriate for multi-line laser applications such as increasing efficiency on up-conversion visible-UV lasers [15, 17].

Although with better thresholds, the less efficient system was the one for 50% feedback that exhibited much lower pump depletion and hence the residual pump contains most of the total energy. Therefore, the maximum conversion efficiency was only 6.5% at 4.5 W pump for the first Stokes and just 7.3% at maximum pump for the second. The generation thresholds were 0.64 W and 1.29 W, respectively.

In general, for lower feedback systems the generation thresholds are rather high; but once reached, there is high energy-conversion efficiency. For higher feedbacks, although lower thresholds take place, the trade-off is huge in terms of energy conversion since most of the generated energy is contained within the cavity (more nonlinear effects), insertion losses are added (less power delivered) and pump depletion is poorer.

To better understand the energy transfer in these systems, lower order signals were studied in more detail. In addition, a weak anti-Stokes signal (1018 nm) was present during all experiments. **Figure 2.4a** shows a typical spectrum that corresponds to 4% feedback configuration whereas **figure 2.4b** presents the pump-dependent evolution of the anti-Stokes signal for the same configuration.

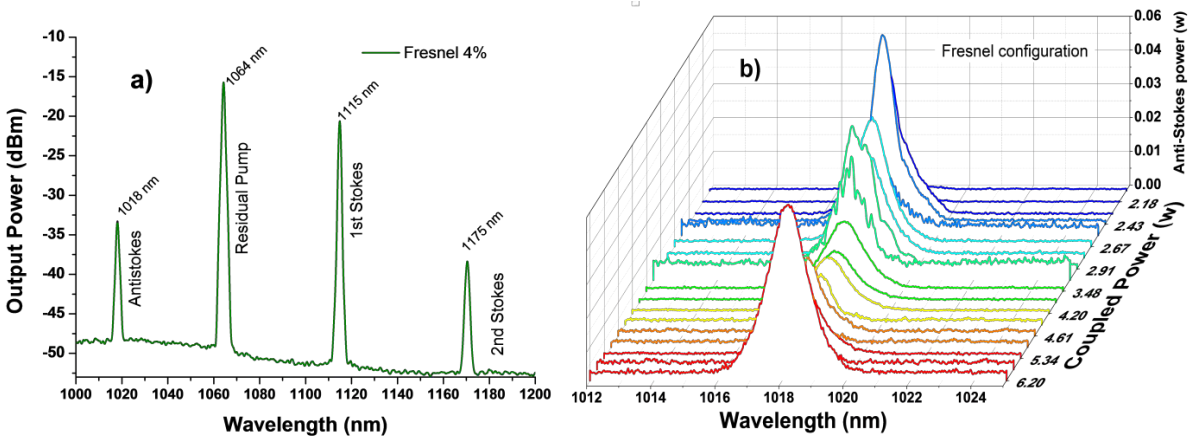

Figure 2.4 a) Typical Raman spectrum with anti-Stokes. b) Pump-dependent anti-Stokes component for Fresnel configuration.

The anti-Stokes signal is often produced by nonlinear effects (FWM and CARS), arising when different frequency components propagate together in the fiber (refer to **section 1.3**). In CW regime, this phase-matched frequency conversion condition is simply satisfied, and therefore an efficient anti-Stokes can emerge [18].

Figure 2.5a shows the Fresnel-configuration energy conversion curves. In the range of 2 W 4 W, the anti-Stokes signal is produced by the FWM process between the pump and the first Stokes waves; two pump photons and one first Stokes photon create the anti-Stokes ($\omega_{as}=2\omega_p-\omega_s$) as in the scheme in **figure 2.5b.** The CARS process in this system is produced when the frequency difference between signals (pump and Stokes) is equivalent to the molecular vibration of the medium (Ω), *i.e.*, $\omega_p-\omega_s=\Omega$, $\omega_{as}-\omega_p=\Omega$, and $\omega_{as}-\omega_s=2\Omega$.

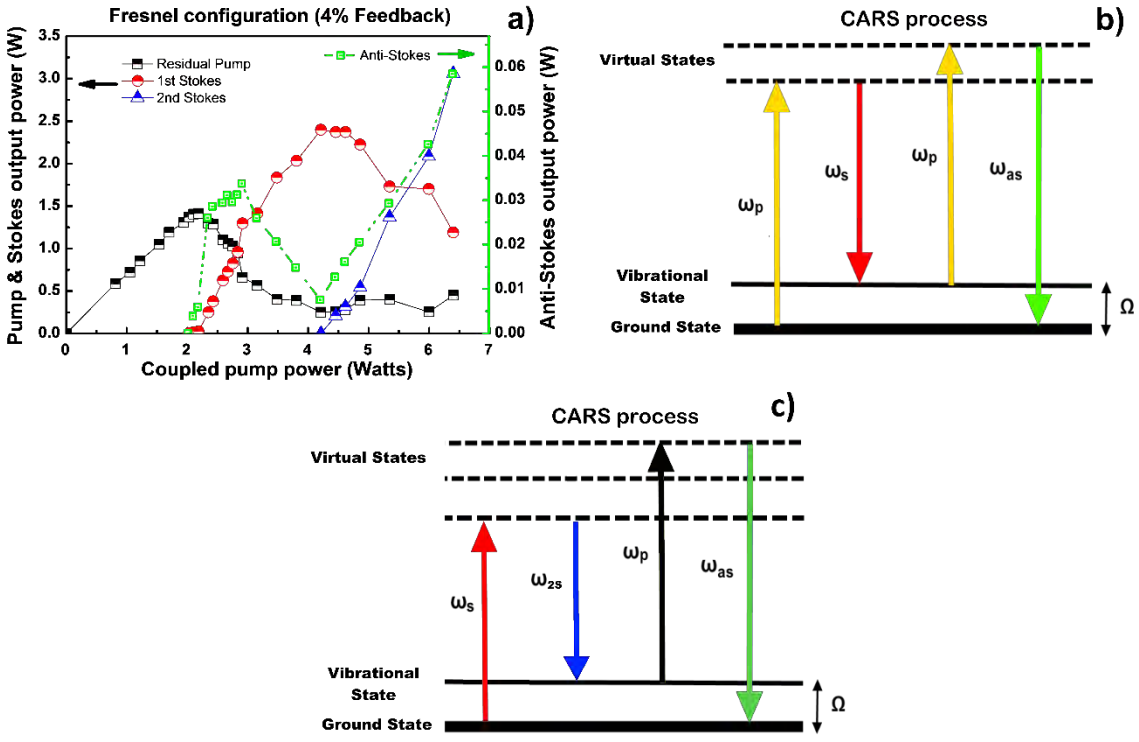

Figure 2.5 a) Fresnel configuration energy conversion curves of the anti-Stokes, residual power, first and second Stokes. b) Degenerate CARS process, c) Non-degenerate CARS process

From **figure 2.5a**, the generation threshold for anti-Stokes signal coincides with the generation of first Stokes at 2 W. Note the high slope efficiency of the anti-Stokes that tends to diminish within the 2.5 W – 2.8 W range where a slight energy recuperation of pump occurs (the pump slope tends to increase). We believe that this recovery occurs because some anti-Stokes photons are re-absorbed in the ground state to give back energy to the pump by generating its own Stokes. Afterwards, before the first Stokes reaches maximum, anti-Stokes and pump deplete giving back their energy to first Stokes. This occurs until the second Stokes emerges. At higher powers (> 4 W) second Stokes is involved and therefore the FWM mechanism changes, a new interaction between pump, first Stokes, and second Stokes photons creates the anti-Stokes. Now one first Stokes photon, one second Stokes photon, and one pump photon produce the anti-Stokes (**figure 2.5c**) ($\omega_{as} = \omega_{1s} + \omega_p - \omega_{2s}$) as a non-degenerate CARS process. At this range, anti-Stokes and pump regain energy along with second Stokes, all fed by the first Stokes.

A similar behavior of the anti-Stokes signal at lower pump power occurs, but for systems in which the second Stokes does not clearly emerge (0% and 50% feedback) the anti-Stokes suddenly vanishes at the higher pump powers. The general behavior allows us

to affirm that not only energy transfer from lower to higher order Stokes takes place but also to their corresponding anti-Stokes signals.

2.5 Conclusion

The increase of OC reflectivity of a Raman resonant cavity results in a decrease of energy-transfer of pump to Stokes, Stokes-to-Stokes and anti-Stokes-to-Stokes components. Configuration with high reflectivity could be useful when the Raman gain fiber is short and/or the pump power available is low. Although the threshold for Stokes generation is easily achieved; the trade-off is low energy efficiency. In this configuration, most Stokes energy is contained inside the cavity and pump energy is poorly absorbed. This is a serious drawback of these configurations that were supposed to be very promising. On the other hand, lowering the OC reflectivity increases the thresholds but improves the energy transfer, making systems with fewer restrictions related to fiber length and/or pump power availability very efficient once threshold is reached; in fact, this (the high threshold operation) is the only one trade-off. Since sufficiently pumped and long Raman fiber lasers are very efficient, using air-glass or even RDFB allows extracting most of the power produced at the Stokes signals.

In summary, as investigated here it is worthwhile to have longer fibers for more efficient Raman fiber lasers than spending in several FBGs to have shorter fibers with the drawback of much more inefficient systems.

In the next chapter, we have gone even further away, when eliminating some of the FBGs for the inner cavities, making the system even cheaper and having very interesting results.

2.6 Acknowledgment

Portions of this chapter have been formally published at the Laser Physics Journal as: M. Juárez-Hernández, E. B. Mejía, L. de la Cruz-May, O. Benavides, "Stokes-to-Stokes and anti-Stokes-to-Stokes energy transfer in a Raman fiber laser under different cavity configurations," Laser Phys. **26**, 115105 (2016).

2.7 References

1. S. Singh and R. S. Kaler, "Flat-Gain L-Band Raman-EDFA Hybrid Optical Amplifier for Dense Wavelength Division Multiplexed System," IEEE Photonics Technol. Lett. 25, 250–252 (2013).

2. Y. Y. Zhu, W. L. Zhang, and Y. Jiang, "Tunable Multi-Wavelength Fiber Laser Based on Random Rayleigh Back-Scattering," IEEE Photonics Technol. Lett. 25, 1559–1561 (2013).
3. M. K. Saxena, S. D. V. S. J. Raju, R. Arya, R. B. Pachori, S. V. G. Ravindranath, S. Kher, and S. M. Oak, "Raman optical fiber distributed temperature sensor using wavelet transform based simplified signal processing of Raman backscattered signals," Opt. Laser Technol. 65, 14–24 (2015).
4. G. Bolognini and A. Hartog, "Raman-based fiber sensors: Trends and applications," Opt. Fiber Technol. 19, 678–688 (2013).
5. H. G. Breunig, M. Weinigel, R. Bückle, M. Kellner-Höfer, J. Lademann, M. E. Darvin, W. Sterry, and K. König, "Clinical coherent anti-Stokes Raman scattering and multiphoton tomography of human skin with a femtosecond laser and photonic crystal fiber," Laser Phys. Lett. 10, 25604 (2013).
6. R. H. Stolen, "Fiber Raman lasers," Fiber Integr. Opt. 3, 21–51 (1980).
7. S. G. Grubb, T. Erdogan, V. Mizrahi, T. Strasser, W. Y. Cheung, W. A. Reed, P. J. Lemaire, A. E. Miller, S. G. Kosinski, G. Nykolak, P. C. Becker, and D. W. Peckham, "1.3 μm Cascaded Raman Amplifier in Germanosilicate Fibers," in Optical Amplifiers and Their Applications (1994), p. PD3.
8. S. K. Turitsyn, S. A. Babin, D. V. Churkin, I. D. Vatnik, M. Nikulin, and E. V. Podivilov, "Random distributed feedback fiber lasers," Phys. Rep. 542, 133–193 (2014).
9. D. V. Churkin, S. A. Babin, A. E. El-Taher, P. Harper, S. I. Kablukov, V. Karalekas, J. D. Ania-Castañón, E. V. Podivilov, and S. K. Turitsyn, "Raman fiber lasers with a random distributed feedback based on Rayleigh scattering," Phys. Rev. A 82, 33828 (2010).
10. A. E. El-Taher, P. Harper, S. A. Babin, D. V Churkin, E. V Podivilov, J. D. Ania-Castanon, and S. K. Turitsyn, "Effect of Rayleigh-scattering distributed feedback on multiwavelength Raman fiber laser generation.," Opt. Lett. 36, 130–2 (2011).
11. I. D. Vatnik, D. V Churkin, E. V Podivilov, and S. A. Babin, "High-efficiency generation in a short random fiber laser," Laser Phys. Lett. 11, 75101 (2014).
12. H. Zhang, P. Zhou, H. Xiao, and X. Xu, "Efficient Raman fiber laser based on random Rayleigh distributed feedback with record high power," Laser Phys. Lett. 11, 75104 (2014).
13. Z. Wang, H. Wu, M. Fan, L. Zhang, Y. Rao, W. Zhang, and X. Jia, "High power random fiber laser with short cavity length: Theoretical and experimental investigations," IEEE J. Sel. Top. Quantum Electron. Sel. Top. Quantum Electron. 21, 10–15 (2015).
14. S. A. Babin, I. D. Vatnik, A. Y. Laptev, M. M. Bubnov, and E. M. Dianov, "High-efficiency cascaded Raman fiber laser with random distributed feedback," Opt. Express 22, 24929 (2014).
15. D. V. Talavera and E. B. Mej a, "Blue up-conversion Tm3+-doped fiber laser pumped by a multiline Raman source," J. Appl. Phys. 97, 53102 (2005).
16. L. de la Cruz-May, E. B. Mejia, O. Benavides, J. Vasquez Jimenez, J. Castro-Chacon, and M. May-Alarcon, "Novel Technique for Obtaining the Raman Gain Efficiency of Silica Fibers," IEEE Photonics J. 5, 6100305–6100305 (2013).
17. E. B. Mejía, A. N. Starodumov, and Y. O. Barmenkov, "Blue and infrared up-conversion in Tm3+-doped fluorozirconate fiber pumped at 1.06, 1.117, and 1.18 μm," Appl. Phys. Lett. 74, 1540–1542 (1999).
18. S. Zaitsu and T. Imasaka, "Continuous-wave anti-Stokes Raman laser based on phase-matched nondegenerate four-wave mixing.," Opt. Lett. 40, 73–76 (2015).

Chapter 3

Second (1178 nm) and third (1242 nm) Stokes Raman fiber lasers without intermediate Stokes cavities

Chapter 3

3. *Second (1178 nm) and third (1242 nm) Stokes Raman fiber lasers without intermediate Stokes cavities*

3.1 Abstract

In the work described in this chapter, we propose what we consider an original and novel configuration for cascaded RFLs. This system starts operating as an open cavity laser (*i.e.*, no FBGs) for lower order Stokes components, and becomes unidirectional once the higher order single-FBG cavity reaches operating threshold. Hence, it consists on unidirectional laser cavity using a single high-reflecting FBG and the Fresnel reflection as output coupler (OC). This scheme generates two or three Stokes waves; where lower order Stokes (first and second) act as "virtual links" that transfer energy from pump to higher order Stokes signals in the intermediate non-FBG cavities. The system uses commercial silica fiber and minimizes the cost and inserting-loss of all the FBGs that typically compose these systems (traditional nested cavities). The possibility to more easily spam the 1 μm – 2 μm window becomes available through the schemes proposed here.

3.2 Introduction

The cascaded RFLs are traditionally the way for converting signals within the 1.2 μm – 1.6 μm spectral region. Nevertheless, there exist some limitations because of the maximum Raman shift of 13.2 THz (440 cm^{-1}) and 14.1 THz (470 cm^{-1}) provided by silica-based (cheap) commercial optical fibers [1]. When wavelengths beyond these shifts are desired to be generated, schemes often consist of nested cavities, with intermediate cavities using several pairs of FBGs. To achieve radiation in the long wavelength part of the region, one needs to have more than three Raman cascades (therefore more than three pairs of FBGs) if using a germanosilicate fiber [2]. This common scheme implies poor efficiency since the introduction of each FBG produces an insertion loss of more than 1 dB, in addition to the losses introduced by splices.

The usual solution for reducing the number of FGBs, is using a (usually non-commercial) high concentration P_2O_5-doped fiber that presents a Raman frequency shift at around 40 THz or 1330 cm^{-1} [3] (see **figure 1.10**). This proposal was suggested as Raman medium in [4], as a way to simplify the schemes and to increase the efficiency; although a good solution, it is expensive given that producing this fiber is not as simple as producing

silica fiber. The fabrication of phosphosilicate fibers presents several complications, such as different thermal expansion coefficients (for SiO_2 and P_2O_5) and melting temperatures.

Although phosphosilicate Raman fibers are still used for constructing CW RFLs, to cover the spectral region of 1.1 μm – 1.6 μm [3], these CW phosphates-based medium-power laser systems might not be the most convenient sources for pumping optical fiber amplifiers and some lasers, since, the loss-coefficient of these fibers grows considerably by increasing the P_2O_5 contents. Apart from being a little far from the 1550 nm region, the minimum loss for phosphates (located at 1340 nm – 1500 nm) is about 0.8 dB/km compared to 0.22 dB/km (at 1550 nm) for Silica [5].

Motivated on this, we present an alternative scheme that solves most of these disadvantages. The resonant frequencies of silica molecules inside an optical fiber pumped at around 1064 nm vibrate around 440 cm^{-1} (at room temperature), where the first Stokes is generated. We have demonstrated that it is possible to directly obtain the second Stokes Raman shift at around 900 cm^{-1} without using an intermediate first Stokes cavity. Once the cavity reaches operation, it practically transforms all the energy from pump and bi-directional intermediate components into a single and narrow (unidirectional) signal. Even more, we probed that is possible to achieve higher-order Stokes waves without using inner cavities for the intermediate ones.

In this proposed system, although longer fiber is required; it does not rely on using the intermediate FBGs for inner cavities, making it even simpler and cheaper than our system studied in [6] (**Chapter 2**).

Important advantages such as commercial affordability and avoiding splicing and FBGs losses are present in this proposal. Although, a quantitative comparison to typical cascaded phosphate based systems is beyond the scope of the work, the hypotheses based in the RDFB intermediate cavities operating as “virtual links” perfectly worked with a degree of reproducibility up to the situation of achieving a fourth Stokes (1310 nm) by means of a single third-Stokes half cavity of 5 km of silica fiber. We describe the detailed experiments, results and conclusions in the following sections.

3.3 Experimental methodology and Results

For our experimental setup, we used an OFS® TrueWave® RS (Reduced slope Low water peak) Raman gain fiber. The gain Raman Efficiency of this fiber is shown in **figure 3.1** [7]. Firstly, we obtained the loss spectrum of the TrueWave® RS. To do this, we used a 940 nm pumped ytterbium-doped fiber for generating amplified spontaneous emission (ASE) for 1 μm –1.2 μm region used as "white light" for applying the cutting-back method in the fiber as described in [8]. We measured this spectrum with the optical spectrum analyzer (OSA) *Thorlabs 201*®. Such data was completed with the data-sheet of the manufacturer [9] that covers the 1250 nm – 1625 nm region, and completed with the Reference [7] for the 1440 nm – 1675 nm region.

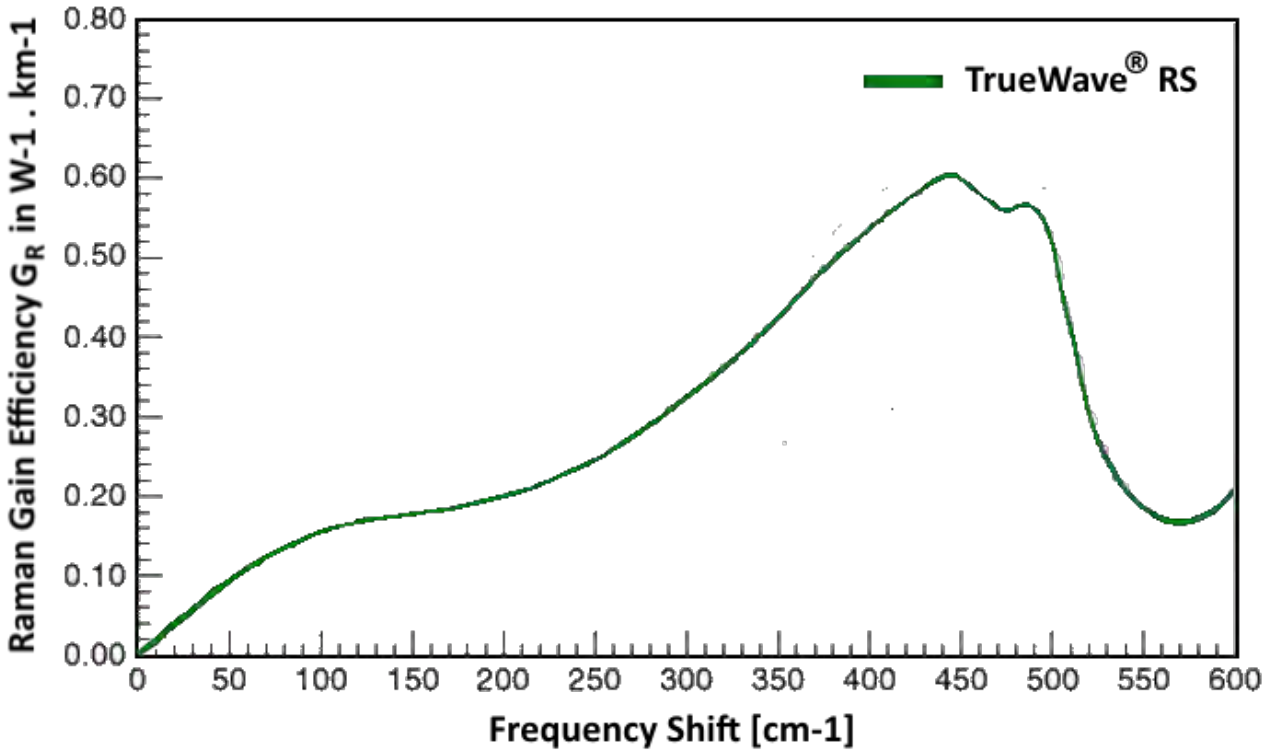

Figure 3.1 Raman gain efficiency spectra for TrueWave® RS optical fiber [7].

The "whole" spectrum is shown in **figure 3.2**. Observe that this fiber has low loss in the 1375 nm – 1425 nm region, where the water-loss peak is present in most standard fibers. These peak practically does not exist for this fiber and hence opens the possibility to overcome this "barrier" for obtaining Stokes signals at higher orders.

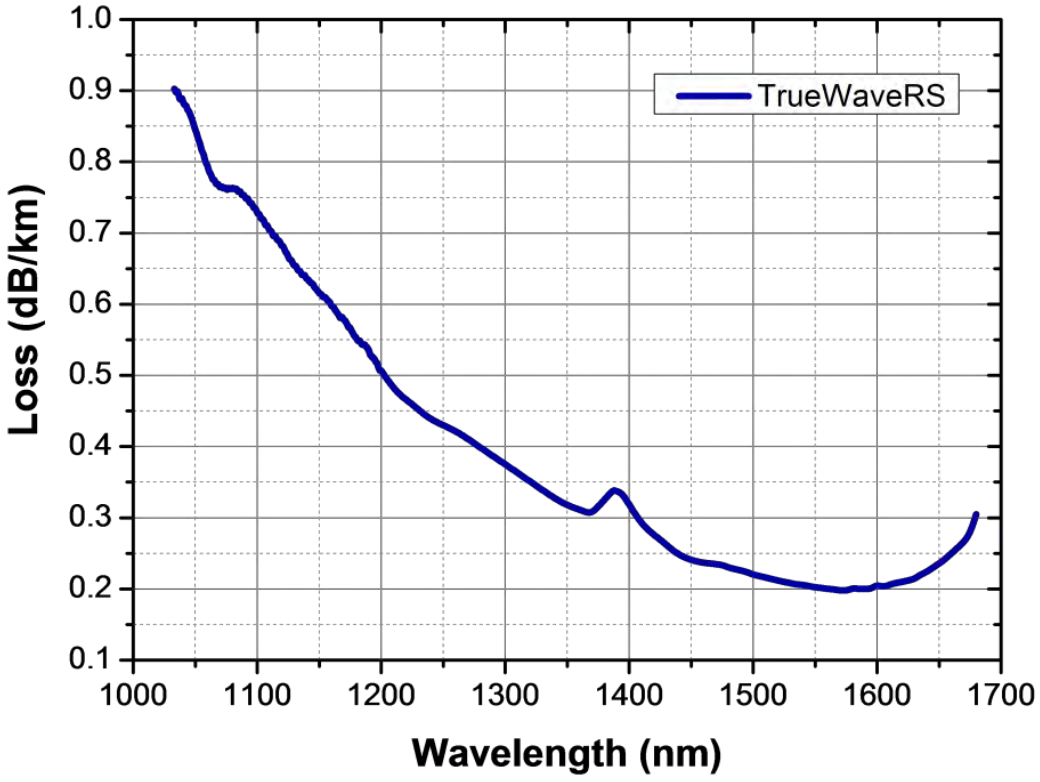

Figure 3.2 Attenuation Vs. Wavelength of TrueWave® RS optical fiber

Our initial experiment was realized in a free-running RFL configuration composed of 5 km of the TrueWave® RS fiber, *i.e.*, using non-selective cavity whose broadband mirrors are composed of RDFB [10] along the fiber together with glass-air interface (Fresnel refection) at the output end. This fiber is single-mode (SM) from 1250 nm to longer wavelengths. This system was pumped with an optically-isolated 1064 nm ± 0.4 nm ytterbium CW (10 W maximum) SM fiber laser from *IPG photonics*® (**figure 3.3**).

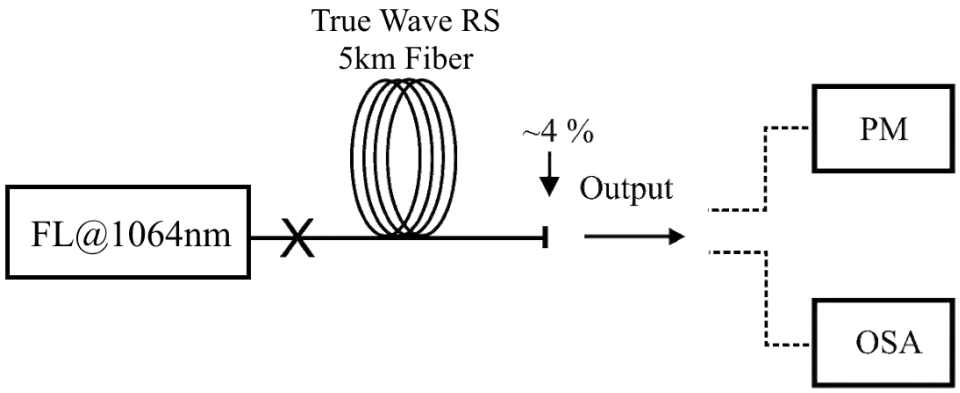

Figure 3.3 Experimental setup for free-running configuration.

Before realizing a more detailed analysis, we took some delivered spectra when applying several pump powers. **Figure 3.4a** contains two of them, one corresponding to 3.2 W, the first Stokes is clearly generated at 1117.55 nm, 13.2 THz shift and at 1121.54 nm corresponding to 14.1 THz. Although not shown in the figure because it is so weak, an anti-Stokes at 1015.7 nm also becomes generated. As observed in the second spectrum for 6 W coupled pump, the double-line second Stokes is now generated at 1176.5 nm and 1178 nm (also 13.2 THz and 14.1 THz shifted). Also, the third Stokes gets generated at around 1242 nm (same frequency shift); the anti-Stokes is still there, although much weaker, as it will be described below.

From this type of spectral information, we obtained the power at each Stokes component (sometimes composed of several spectral lines) as described in [8] and presented in **figure 3.4b**, where one may observe the energy transfer evolution as coupled pump power increases.

The residual pump (red dash line), gradually feeds Stokes signals, *i.e.*, it starts to deplete as soon as the first Stokes (blue short dash line) starts to rise (at just 0.6 W). The anti-Stokes signal (black dash-pointed line) rises just after (0.8 W); although weak, apparently it promotes energy transfer back from first Stokes to pump for the 0.8 W – 2.7 W interval. At 2.1 W first Stokes equals the pump and at 2.5 W anti-Stokes reaches zero, then the system starts operating also on the 14.1 THz shift (1121.54 nm) [11]. The gradual increase of the pump makes the first Stokes signal absorbing all the energy from it. Once the anti-Stokes signals disappears, the system returns to the typical energy transfer (*i.e.*, energy goes from pump to Stokes).

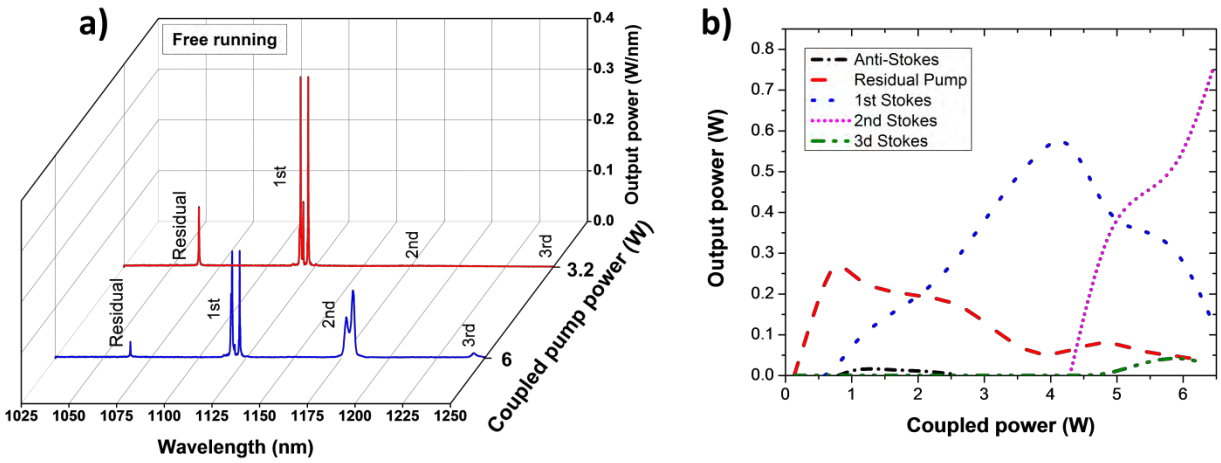

Figure 3.4 a) Typical emitted spectra (3.2 and 6W coupled pump) of the "free-running" configuration; b) Delivered powers at all signals as function of pump power for free-running setup.

At above ~4.0 W coupled power the residual pump signal starts recovering some energy, while the first Stokes wave starts depleting, along these phenomena the 2nd Stokes wave appears (pink short dot line) at 4.3 W, corresponding mainly to 1177.44 nm (13.2 THz shift). It is important to note here, that the pump acts like the "anti-Stokes" for the dominant first Stokes signal (1117.55 nm).

When the energy increases to 4.83 W a second spectral line for 2nd Stokes wave appears (not visible) at 1181 nm (14.1 THz shift). This occurs until the 3rd Stokes wave appears (green dash-double dot line) at 4.75 W coupled pump, corresponding to 1244.3 nm. Again the 3rd Stokes wave gives energy back to all signals as observed by the positive slope changes of the curves. At 6.44 W, most power is delivered by 2nd Stokes wave. Although not shown, the 4th Stokes appeared here as a band centered at 1323.83 nm (only visible with log scale).

In **figure 3.5**, a new scheme is presented. A 13.2 THz 2nd Stokes FBG (1177.7 nm) was introduced into the cascaded RFL cavity (notice that we did not include the 1117.55 nm FBG corresponding to the 1st Stokes).

Figure 3.6a contains the delivered spectra as function of coupled pump power. At low powers below 3.2 W the system behaves equally as the "free running" system. But once 2nd Stokes is generated (1177.7 nm); this absorbs most of the energy delivered by the pump and the 1st Stokes. At higher powers (6 W), the system behaves as a free running cavity setup pumped with a source at 1177.7 nm wavelength. **Figure 3.6b** gives the output power variation with coupled pump power.

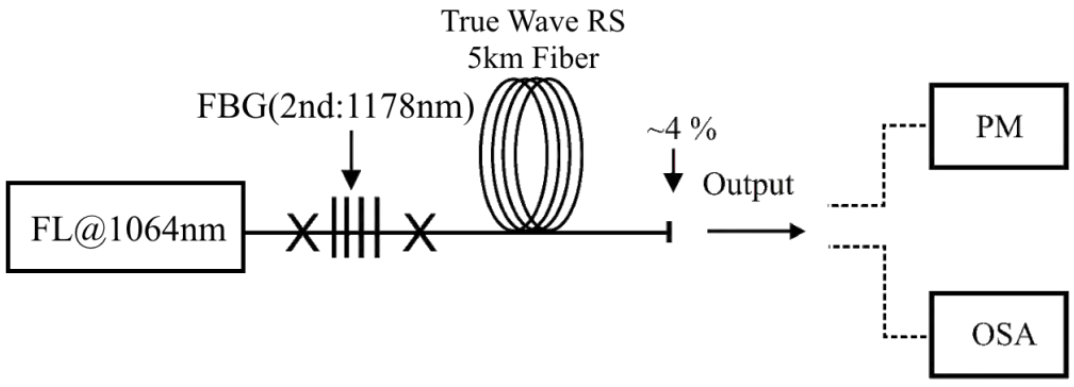

Figure 3.5 Raman fiber laser with cavity for second Stokes wave (1178nm).

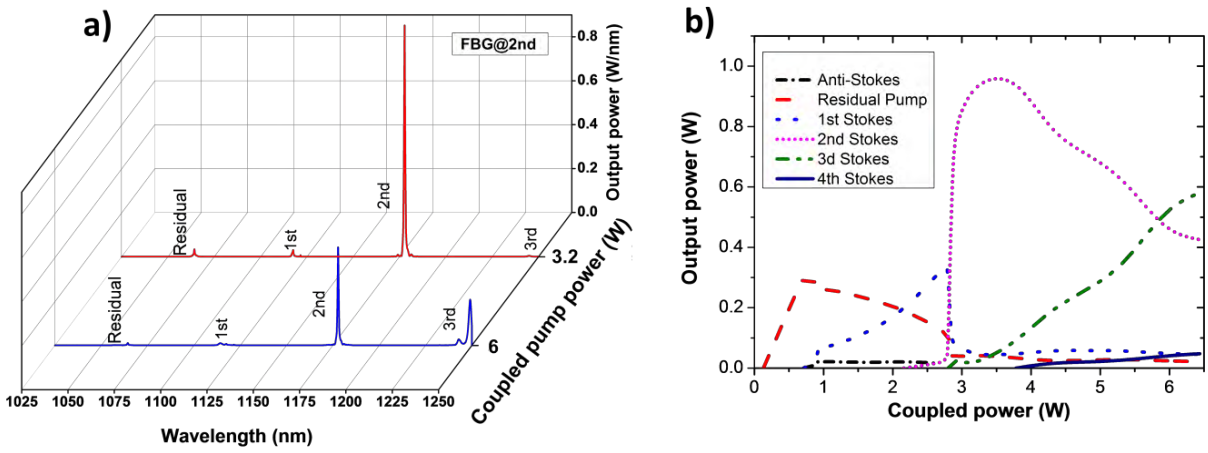

Figure 3.6 a) Emitted spectra of the RFL with cavity for second Stokes; b) Delivered powers at all signals as function of pump power (FBG@1178 nm).

In **figure 3.6b** before the system reaches 2.69 W it operated exactly as the previous one (free running), at this point the FBG demands most of the energy that was contained within the pump (1064 nm red dash line), the 1st Stokes (1117 nm blue dot line) and the anti-Stokes (1015 nm black dash dot line). This behavior was somehow expected from our hypothesis, as 1st Stokes wave acts as an energy reservoir under this scheme. This signal (1177.7 nm) consolidates fully at 3.5 W (30% efficiency) with a single spectral line (the FBG line). The system then becomes unidirectional by the sense that most power is delivered through a single fiber end because the other end is the HR FBG; *i.e.*, out of this interval (2.69 W – 3.5 W) all free running generated signals are delivered through both ends. The system starts functioning as a free running laser pumped by 1117.7 nm (2nd Stokes).

The next Stokes waves, the third (1240 and 1245 nm green dash line) and the fourth (1324 nm solid blue line) act as in a nested cavity cascade RFLs.

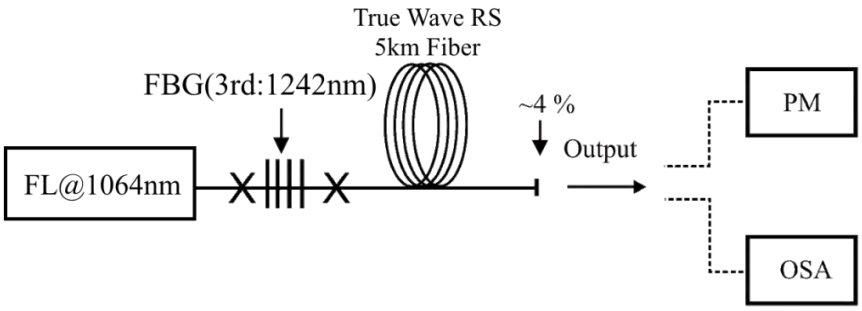

Figure 3.7 Raman fiber laser with cavity for third Stokes wave (1242 nm).

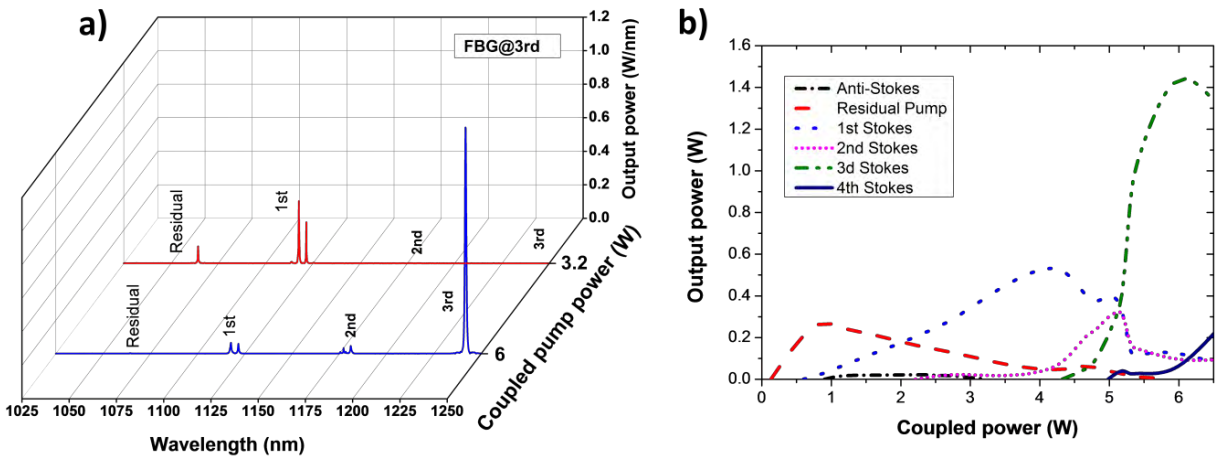

Figure 3.8 a) Emitted spectra of the RFL with cavity for third Stokes; b) Delivered powers at all signals as function of pump power (FBG@1242 nm).

The result obtained here gives the possibility for using more than one intermediate "virtual links" (or alternated links) for scaling up to even higher orders of Stokes components. We explored this possibility by modifying the configuration as in **figure 3.7** operated as "virtual links" while a third Stokes FBG located at 1241.7 nm was used to force the system to operate in this region.

We also decided to probe the scheme shown in **figure 3.8.** Where we present the emitted spectra for different pump powers in **figure 3.8a;** again, the system behaved as "free running" for low coupled pump powers (see the red solid line at 3.2 W), this happened over a larger power interval (0 W – 4.5 W) (**figure 3.8b** shows the energy transfer evolution). From this part of the figure, at 4.65 W the 3rd Stokes (green dash dot line) absorbs now the 2nd Stokes (pink short dot line) while at the same time it feeds-back energy to the first (blue dash line) and residual pump (red dash line). We observed that at 5 W the 3rd Stokes demonstrates sudden rise from 0.35 W to 1.5 W output power just at increasing pump by only 0.7 W containing practically all the energy, at around 6 W. Moreover, two more Stokes, 4th (navy solid line) and 5th (almost insignificant), corresponding to 1310 nm and 1393 nm just appear (in a 3rd Stokes free running fashion).

Note that at 6 W coupled pump, 3rd Stokes reaches its maximum of 1.5 W with 25% efficiency. As fully expected, this causes a serious depleting of all other signals (lower order ones).

It was not possible to explore beyond these wavelengths, but we believe that the next components at 1486.6 nm (6th), 1590.6 nm (7th), 1710.3 nm (8th), 1849.5 nm (9th) and 2013.3 nm (10th) corresponding to 7th to 10th Stokes, would cover the transmission window

of silica fiber. Hence, omitting FBGs benefits a lower cavity loss given that each FBG usually inserts 0.5 to 1 dB loss to the cavities; using a single FBG is (roughly-speaking) equivalent to add one additional kilometer of optical fiber. It is in this point where our results become of importance for improving and more efficient scaling to longer wavelengths, at moderate pumping powers.

3.4 Conclusions

We propose a new approach for Raman fiber lasers with simplified cavities by eliminating some FBGs in cascaded systems. We demonstrated that it is not necessary to complete all the intermediate Stokes cavities to scale up to higher orders. In fact, schemes based on our proposal minimize the detrimental back energy transfer to lower order, present in “regular” schemes, providing a more optimized, simpler and cheaper system. With this approach, it is possible to substitute expensive Raman gain fibers such as phosphate fibers by commercial silica fibers (much cheaper) in long-shifted Raman fiber lasers and amplifiers.

3.5 Acknowledgment

Portions of this chapter have been formally published at the Laser Physics Journal as: E. B. Mejia, M. Juárez-Hernández, and L. De La Cruz-May, "Second (1178 nm) and third (1242 nm) Stokes Raman fiber lasers without intermediate Stokes cavities," Laser Phys. **27**, (2017).

3.6 References

1. A. Bertoni, "Analysis of the efficiency of a third order cascaded Raman laser operating at the wavelength of 1.24 μm," Opt. Quantum Electron. **29**, 1047–1058 (1997).
2. S. G. Grubb, T. Strasser, W. Y. Cheung, W. A. Reed, V. Mizrahi, T. Erdogan, P. J. Lemaire, A. M. Vengsarkar, D. J. DiGiovanni, D. W. Peckham, and others, "High-power 1.48 μm cascaded Raman laser in germano-silicate fibers," Tech. Dig. Ser. Soc. Am. **18**, 197–199 (1995).
3. E. M. Dianov and A. M. Prokhorov, "Medium-power CW Raman fiber lasers," IEEE J. Sel. Top. Quantum Electron. **6**, 1022–1028 (2000).
4. E. M. Dianov, M. V. Grekov, I. A. Bufetov, S. A. Vasiliev, O. I. Medvedkov, V. G. Plotnichenko, V. V. Koltashev, A. V. Belov, M. M. Bubnov, S. L. Semjonov, and A. M. Prokhorov, "CW high power 1.24 μm and 1.48 μm Raman lasers based on low loss phosphosilicate fibre," Electron. Lett. **33**, 1542 (1997).

5. C. Headley; M. Mermelstein; and J.-C. Bouteiller, "Raman Fiber Lasers," in *Raman Amplifiers for Telecommunications 2 Sub-Systems and Systems*, M. N. Islam, ed., 1st ed., Springer Series in Optical Sciences (Springer New York, 2004), Vol. 90/2, pp. 353–382.
6. M. Juárez-Hernández, E. B. Mejía, L. de la Cruz-May, O. Benavides, "Stokes-to-Stokes and anti-Stokes-to-Stokes energy transfer in a Raman fibre laser under different cavity configurations," Laser Phys. **26**, 115105 (2016).
7. C. R. S. Fludger, "Linear Noise Characteristics," in *Raman Amplifiers for Telecommunications 1: Physical Principles*, M. N. Islam, ed. (Springer New York, 2004), pp. 91–120.
8. L. Cruz-May and E. B. Mejia, "Raman fiber laser improvement by using Yb^3+-doped fiber," Laser Phys. **19**, 1017–1020 (2009).
9. "http://www.ofsoptics.com/index.html".
10. S. K. Turitsyn, S. A. Babin, D. V. Churkin, I. D. Vatnik, M. Nikulin, and E. V. Podivilov, “Random distributed feedback fibre lasers,” Physics Reports, vol. 542, no. 2. pp. 133–193, 2014.
11. R. H. Stolen, C. Lee, and R. K. Jain, "Development of the stimulated Raman spectrum in single-mode silica fibers," J. Opt. Soc. Am. B **1**, 652 (1984).

Chapter 4

Rare earth doped optical fibers

Chapter 4

4. *Rare earth doped optical fibers*

4.1 Introduction

Amplifiers and lasers based on optical fibers, have many important features that make them the ideal systems for some applications, superior to bulk-type lasers. Optical fiber lasers have the special characteristic of having an enlarged big-gain active material, due to their fiber-lengths ranging from a few centimeters to hundreds of meters. By being able to roll them up, these systems occupy small spaces, which make them relatively compact. Furthermore, these lasers dissipate the heat naturally and very efficiently, since the optical fibers have a large surface to volume relation requiring, most of the time, no additional cooling systems. Also, they usually have very small pump power threshold for lasing operation because of their high gain and low attenuation.

In order for an optical fiber to act as an optical amplifier or a laser, this has to have "active" compounds inside its core. Some of these "active compounds" also usually called "active centers" are the *rare earth* (RE) elements. The RE elements are a group of transition metals, found mainly in the first row below the main body of the periodic table (the lanthanide series, that occupy the atomic numbers from 57 to 71), plus scandium and yttrium (**figure 4.1**). Despite the name, these elements are fairly abundant in the Earth's crust. However, they do not appear in pure form in nature, but they are found as compounds in some minerals. Their properties make them extremely difficult to isolate.

The lanthanides have several properties that become suitable for doping optical fibers to function as optical amplifiers and lasers; these elements present absorption and emission bands from the ultraviolet (UV) to the Infra-red (IR), in the 200 nm – 6000 nm region [1]. The host materials for this kind of elements are usually glasses and crystals.

When doping optical fibers with REs, these depend on the host material since several properties are affected, among others: the fluorescence life-times, the emission and absorption cross-section spectra; as well as the excited stated absorption. All these affect their gain capabilities [2]. One example of these optical materials are the fluorozirconate glasses, these glasses possess special properties when doped with REs, since these can absorb up to several photons in the IR to produce optical signals in the visible or UV region [1]. These properties will be discussed more extensively later.

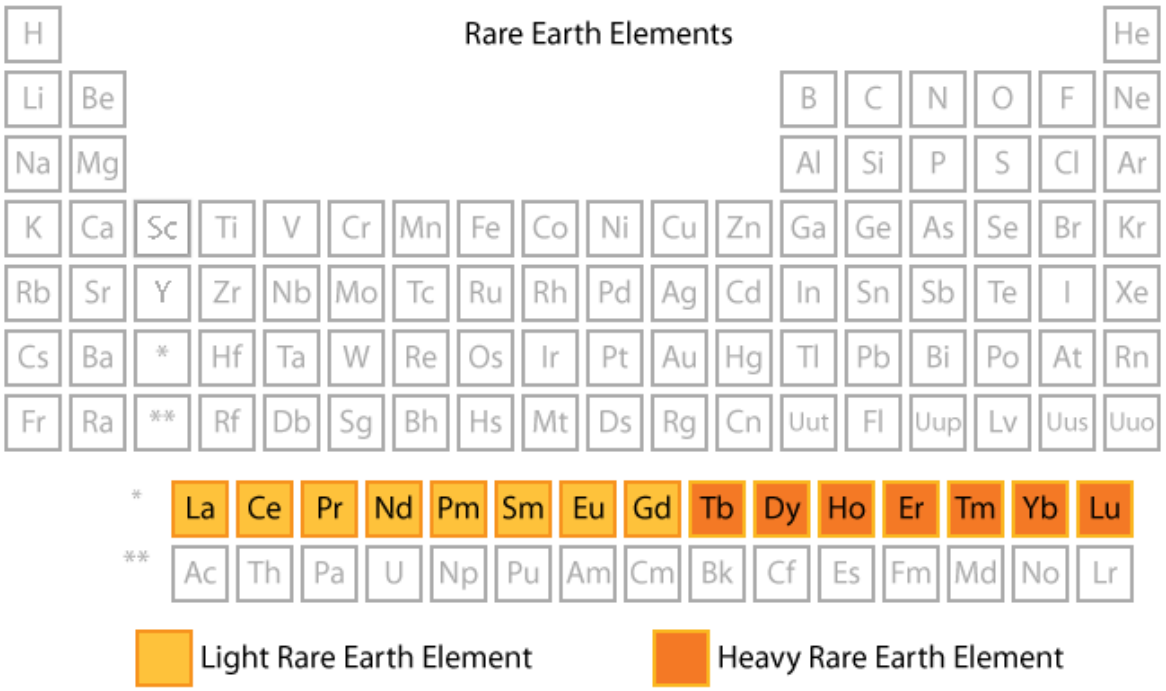

Figure 4.1 Periodic table of the elements delineating the rare earth elements.

4.2 Electronic and optical properties of rare earths

The lanthanides group is characterized for having certain electronic-configuration properties that make them apt for doping optical fibers that can be used as optical amplifiers and lasers.

Atoms of the REs elements usually form trivalent cations and in general the lanthanides are known for having the 4f sublevel semi-filled. The electrons belonging to this sublevel are more compact toward the nuclei when increasing the atomic number (Z), except for the Lanthanum, Cerium, Gadolinium and Lutetium, which use their unique electron from the sublevel 5d [2].

The trivalent ionization level ($^{3+}$) is the most stable state for lanthanides and allows the elements to be optically active. For example, the electronic configuration for non-ionized Thulium is: Tm = [Xe] $4f^{13}$ $6s^2$ (in the compact form); and for the triple ionized Thulium is: Tm^{3+}= [Xe] $4f^{12}$. On the other hand, the Lanthanum (La^{57}) and the Lutetium (Lu^{71}) by being triple ionized have the following electronic configuration: La^{3+}= [Xe] $4f^0$ y Lu^{3+}= [Xe] $4f^{14}$. For these last two elements, their sublevels are filled or closed, being optically inactive.

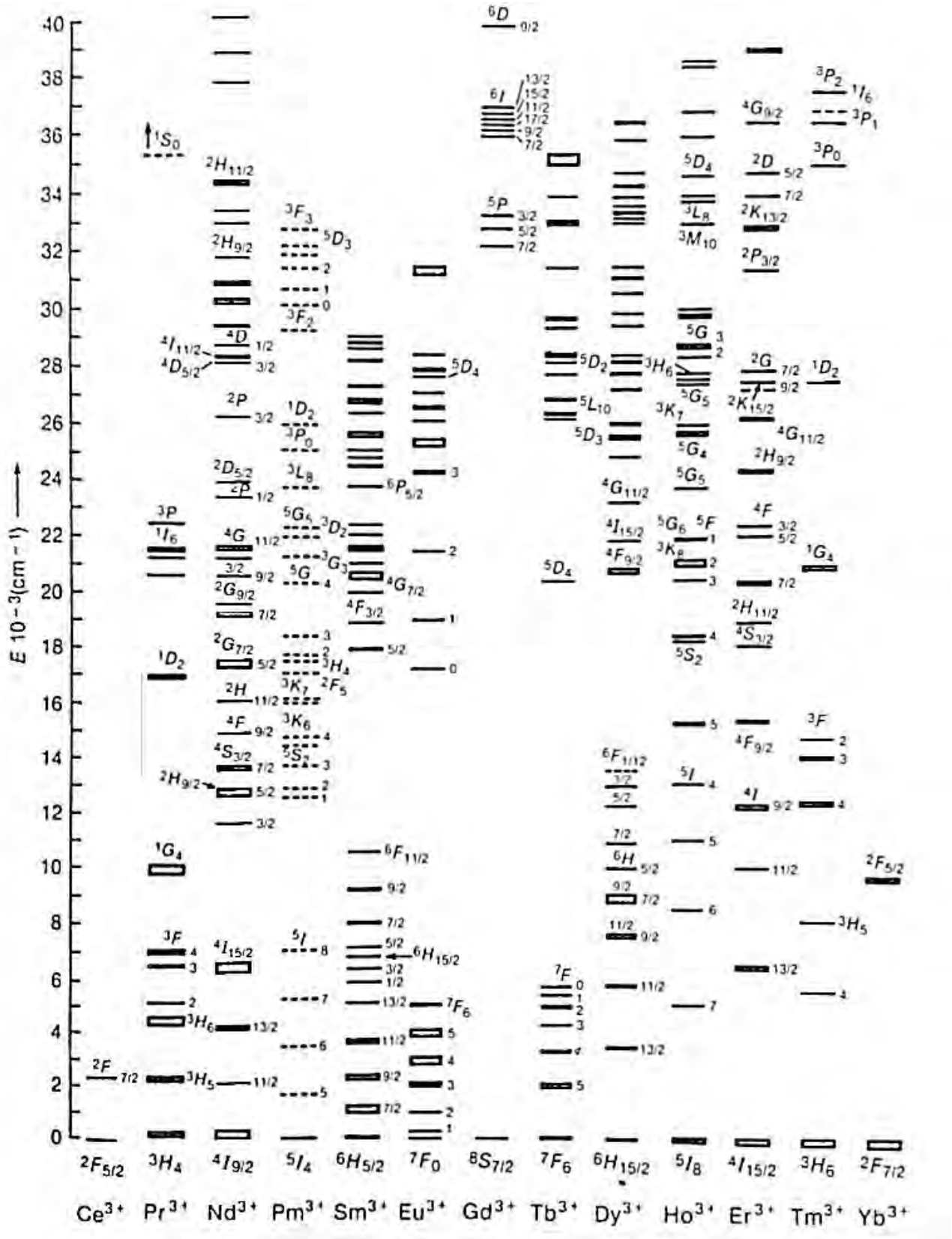

Figure 4.2 Energy level diagram for rare earth elements (Dieke´s diagram).

The spectrum belonging to a triply ionized ion observed in the UV, visible and IR is a consequence of the transitions between states 4f. These transitions are immune to external disturbances such as electromagnetic and vibrational fields of the host material, since the layers of the sub-levels 5s and 5p produce a “protecting” or shielding effect. Optical transitions between states 4f are manifested as thin bands (**figure 4.2**).

When a RE with a trivalent level of ionization (RE^{3+}) is immersed in a condensed material like a crystal or glass, the three electrons operate as strong bonds to the molecules of the host [3].

According to Pauli's exclusion principle, "In an atom, two electrons cannot have their 4 quantum numbers equal." The quantum numbers are: *n*, *l*, *m* and *s*. Where *n* is the energy level of the atomic radial region (*n* = 1, 2…*i*; with *i* integer). The second quantum number *l* is the so-called sub-level, referring to the angular momentum dependent on the type of orbital, and is proportional to the magnetic field produced by its movement, *l* = 0,1 ... *n*-1. Within the sub-level the orbitals have the same general form (*l*) but differ in spatial orientation (*m*). The vector of orbital angular momentum consists of the magnitude *l* and the direction *m* of the translational motion of the electron. The fourth quantum number, *s*, refers to the vector that describes the magnetic field produced by the rotation of the electron and is called "*spin*", then two electrons that occupy the same electronic sub-level rotate in opposite directions [4].

From the Hamiltonian for a central potential with spherical symmetry (for a free ion, without interactions) and obtaining the solution as a function of the product of the radial and angular parts (spherical harmonics), solutions are obtained which are eigenvalues of the Hamiltonian *L* (Total orbital angular momentum) and *S* (total spin). *L* and *S* are the vector sums of the quantum numbers of orbital and spin, $L = \sum_i l_i$ and $S = \sum_i s_i$.

The total angular momentum *J* is given by the vector sum as *J*=*L*+*S*, where *L* is an integer and S may be an integer or a multiple of ½ [5]. The total orbital angular momentum is specified by the letters *S*, *P*, *D*, *F*, *G*, *H*, *I*, *K* ... corresponding to the numbers *L* = 0, 1, 2, 3, 4, 5, 6, 7 ... respectively. The collection of quantum states *J*, *L*, and *S* are designated in a term (*J*, *L*, *S*), in the manner $^{2S+1}L_J$ which is the so-called Russell-Saunders coupling.

This collection of states defines the terms of the configuration, which are all degenerate in the approximation of the central potential. This degeneracy can be reduced due to three types of perturbations related to the electrostatic or Coulomb interaction and the spin-orbit coupling; the latest is the strongest of the magnetic interactions and breaks

down the *LS* degeneration in terms of the levels of *J*. These two do not take electron-electron interactions into account.

There are other types of external interactions. The first is the so-called "Stark effect", which is due to interaction between the structure of atoms or molecules surrounded by an external electric field; this interaction has almost no influence on the electronic structure, however, it modifies the spectral features such as the width and position of emission or absorption lines. Another external effect is the so-called "Zeeman effect", which originates due to the presence of an external magnetic field, and where the degeneration is diminished. This induces the broadening of the emission lines (line splitting).

The linear combinations of the degenerate states serve as a basis for evaluating the states of electron-electron interactions (**figure 4.3**). The angular multiplicity or the number of possible states is $2J + 1$ and the multiplicity of the spin is $2S + 1$.

An example using the notation of the collection of quantum states for the ground state of the Thulium ion (Tm^{3+}), $^3H_6$ corresponds to (6, 5, 1); the angular multiplicity (the possible number of states) is $2J + 1 = 2(6)+1=13$ and spin multiplicity is $2S+1= 2(1)+1=3$.

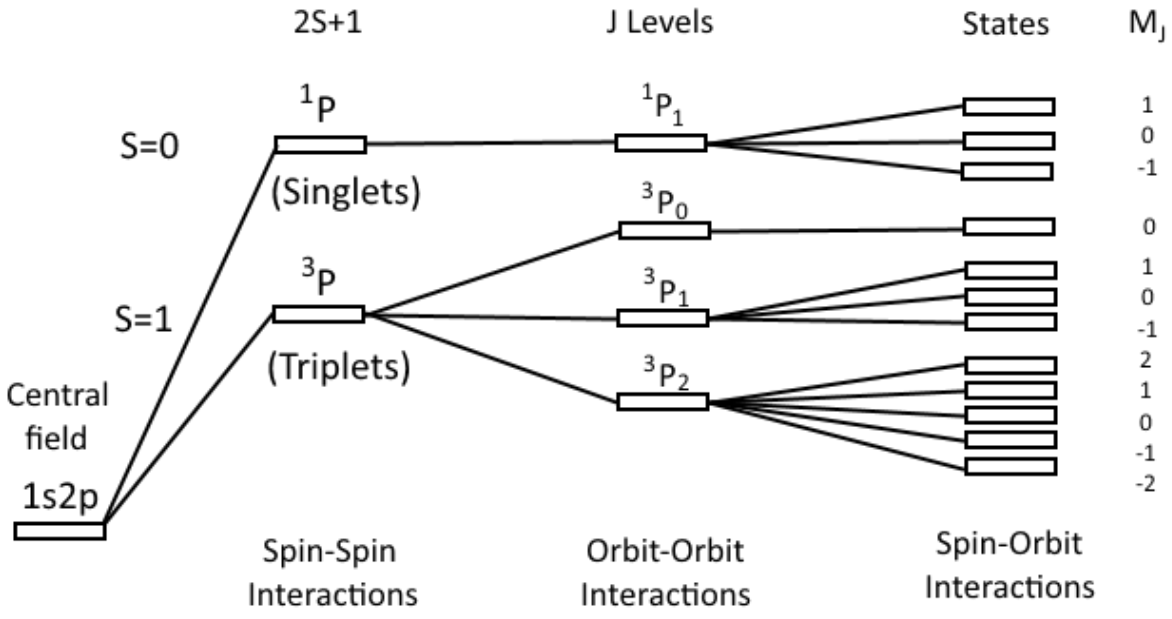

Figure 4.3 Rupture of energy degeneration depending on the type of interaction.

4.3 Properties of ionized rare earths in crystals and glasses

When REs are introduced into a crystalline material, weak interactions occur due to an electric field produced by the interaction with the atoms of the lattice. This kind of interaction gives rise to radiative transitions. Each *JLS* level is divided into discrete sub-levels called “multiplets” whose spacing oscillates around 10 cm^{-1} to 100 cm^{-1} [6]; this effect breaks with the degeneration of the *JLS* level, turning it into a non-degenerate sub-level dependent on the symmetry of the crystal.

In glasses, this kind of interaction (atomic interaction) causes an increase in the separation of energy levels. If the glass is more covalent, as in silicates, it will emit and absorb at longer wavelengths; instead, a more ionic glass like fluorides, emit and absorb at shorter wavelengths [7].

Since crystals have all their atoms perfectly ordered, all RE ions are exactly under the influence of the same crystalline field, and therefore have the same broadening in all their energy levels, so-called "homogeneous broadening." Glasses, on the other hand, do not have an ordered internal structure, each ion presents different multiplets or different Stark-levels and their superposition produces the so-called "inhomogeneous broadening". Each ion has its own absorption and emission spectrum, as well as its own radiative decay time. Therefore, the spectral properties can now be considered as the average of all the individual spectra of each of the ions. This causes the emission and absorption spectra to be wider in glass than in crystals.

There are other types of interactions; these occur when the RE ion immersed in a solid interacts with the "vibration" of the host material, these interactions are called non-radiative or phononic interactions. If the Stark components of a multiplet are energetically close, they can be reached by one or more phonons, which induce upward (less efficient) and / or downward (more efficient) transitions. The high variation of vibrational spectra in a two-level system between the materials makes the non-radiative relaxation process extremely dependent on the host material.

The population level in each band tends to be concentrated in the lower "Stark" sub-level at room temperature, obeying the Boltzmann distribution. This causes the absorption spectrum to shift to shorter wavelengths and the fluorescence or emission spectrum to longer wavelengths (**figure 4.4**). This asymmetry results in the difference between the bands of absorption and fluorescence, which would not occur if all sub-levels "Stark" in a band were equally populated.

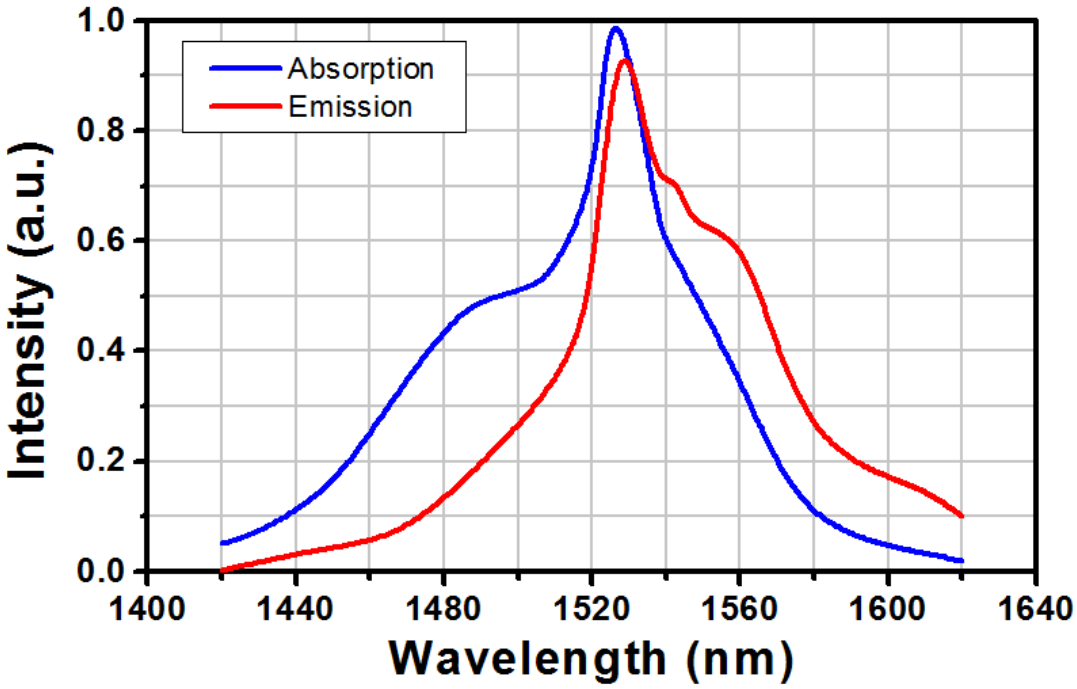

Figure 4.4 Erbium-doped silica fiber emission and absorption spectra.

4.4 Comparison of RE doped- silicate and fluorozirconate based glasses

Glasses, by definition, are an inorganic-fusion product cooled to a rigid condition without crystallization. Its atomic composition is completely random, asymmetric and aperiodic on a large scale. The most common glass is the tetrahedral structure of silica $(S_iO^4)^2$ and silicon dioxide (SiO_2). To these materials metallic impurities, structural defects and water contents can be added, which is a result of the variations in their manufacture [8].

The most common metallic impurities such as alkaline earths modify the atomic networks breaking some oxygen bonds, resulting in an alteration of the atomic structure. They also modify different chemical and physical properties such as density, refractive index, thermal expansion and viscosity, which depends on the temperature. These modifiers (Al^{3+} and Na^{+}) facilitate the incorporation of trivalent REs ions into the glass.

The fundamental optical bands of absorption in silica glass appear in the UV region ~ 0.1 μm due to electronic transitions and in IR at 10 μm due to molecular vibrations. In the UV-visible region there is absorption due to structural defects of the centers and this decreases between the VIS and IR regions.

The variety of glasses that can be created with different compounds is not infinite; in fact, the glasses solidify only if certain molar ratios are respected. Glasses of optical use are classified into four main categories: oxides, halides, oxyhalides and chalcogenides.

In the oxide category, phosphate glasses activated with Nd^{3+} and Er^{3+} have high thermal stability and great potential in high-power applications. Other oxide glasses such as aluminosilicates and germanosilicates are used in the manufacture of Er doped fibers.

In the halide category, heavy metal fluoride glasses have a large variety, which include fluorozirconates, fluoraluminates, fluorindates and fluorogalates. Fluorozirconates are the family with the most stable compounds, since they have low vibrational frequencies which reduce the intrinsic losses near the IR region and improve the fluorescence properties.

Fluoride glasses have a refractive index of 1.46 to 1.57, which offers low Fresnel losses less than 4% and have the unusual property of having a dn/dT of about $-1x10^{-5}$ K^{-1}, which minimizes the thermal auto-focusing when the glass is heated [9].

Glasses have superior advantages than other solid-state materials such as ceramics, polycrystalline and crystalline materials, for the use of optical technologies such as lasers and amplifiers. Since these have several features such as transparency, low birefringence, optical quality, high threshold of optical damage, thermal resistance, low nonlinear refractive index, high variety of possible compositions, adaptability of size and shape, as well as the low cost of raw materials [10].

The use of RE doped glasses in manufacturing optical fibers is very common, especially for the telecommunications area. Most of the optical fibers are silicate-based (SiO_2). Another of the materials that are used in manufacturing optical fiber are the fluorozirconates, specially the ZBLAN so called for its composition of ZrF_4 (56%), BaF_2 (14%), LaF_3 (6%), AlF_3 (4%), and NaF (20%) [mol %]. For the manufacture of ZBLAN optical fibers, it is necessary to have a difference of refractive indexes between the core and the cladding to fulfill the total internal reflection condition; for which additional dopants such as PbF_2 are used to raise the refractive index and HfF_4 to decrease it.

One of the main differences between these glasses is the behavior of the phononic emission. It is observed that the fundamental vibrational modes of the fluorozirconates allow the transmission of UV to mid- IR (0.25 μm – 8 μm); while the silicates are highly absorbent beyond 2 μm. Most fluoride glasses have theoretical losses of 0.001 dB/km at 2.6 μm, which makes them highly transparent beyond 3.5 μm (**figure 4.5**).

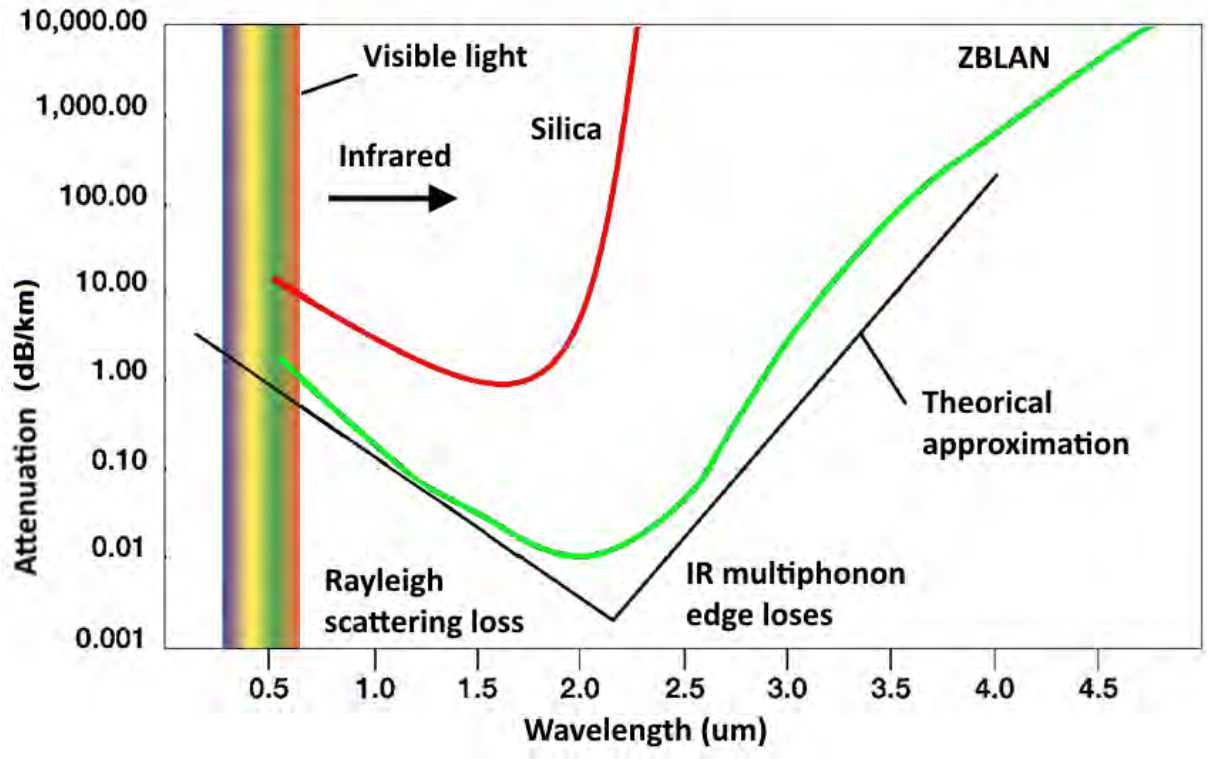

Figure 4.5 Comparison of attenuation between ZBLAN and Silica glasses.

In addition, the multi-phonon probability for emission of an ion at any excited *JLS* level is much higher in silicates than in fluorozirconates, allowing larger lifetimes in the excited state by several orders of magnitude. Comparing the non-radiative transitions between the energy levels of both materials, silicates needs higher phonon energy (in order of 1100 cm^{-1} to 3300 cm^{-1}); whereas in fluorozirconate this is ~580 cm^{-1} to 1740 cm^{-1}. This condition considerably restricts the number of possible laser transitions in RE-doped silicates.

In a metastable state, *i.e.*, an energy state with a long decay lifetime, its lifetime can be reduced considerably due to the multiphonon emission, if the host material supports high energy phonons, as in the case of silicates. The population dynamics of RE ions is established by non-radiative transitions, these enable the depopulation of higher levels to populate lower levels without emission of photons. It is then convenient to have multiphonon reduction, as in the case of heavy metal or fluorozirconate glasses, where its population dynamics is more strongly determined by radiative transitions [11]. This enables the material to have the *up-conversion* phenomenon (this would be discussed later in the chapter).

By having low phonon energy transitions, there are in theory several metastable levels in fluorozirconates, where in these levels may accumulate large amounts of the total population, which may delay radiative decay.

As briefly mentioned before, optical fiber lasers have obvious advantages over other "bulk" counterparts. Fiber lasers overlap both the pump and the laser oscillation signals allowing a superior absorption of the excitation signal. In addition, they extend the possibilities for new sources of pumping, since they can collect several pump beams to increase the intensity and improve the beam quality. High output intensities can be achieved even with minimal powers, *e.g.*, using fibers with a small core diameter and high numerical aperture (NA).

The RE doped fluoride-fiber lasers have low losses and allow the up-conversion mechanism, which is an advantage. It allows populating the upper states of higher energies and exploits the huge lifetimes of the intermediate excited states [3]. Then, up-conversion lasers can operate at shorter wavelengths than the pumping source (**figure 4.6**). In addition, since they have low phononic energies their range of available wavelengths goes from the near-UV to the mid-IR.

Throughout several investigations, researchers have tried to implement new pumping schemes for fiber lasers that allow the generation of new wavelengths by pumping with laser diodes LDs (commercial or still in development). These systems can provide new available wavelengths where solid state lasers cannot provide or are difficult to obtain. Since the RE absorption has a wide bandwidth (> 5 nm), these sources are an excellent option to be used.

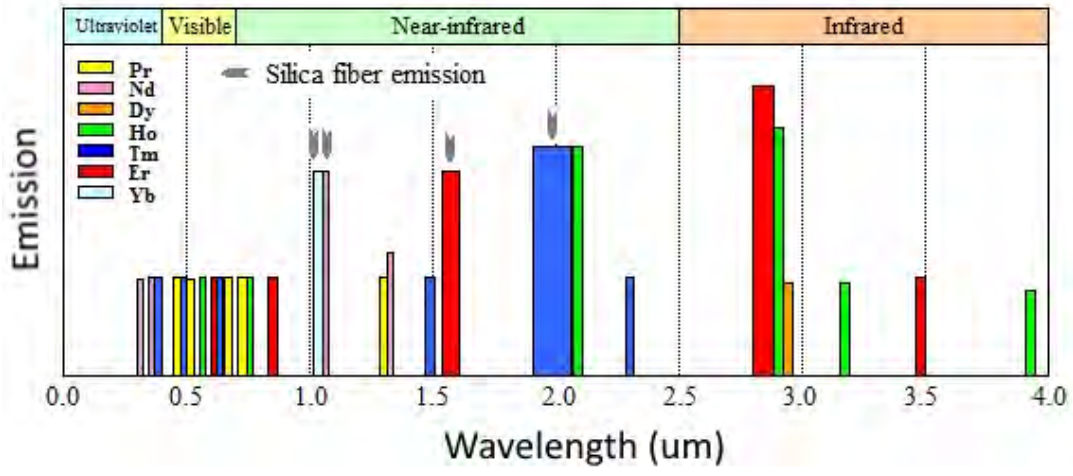

Figure 4.6 Emission wavelengths of laser transitions demonstrated to date in rare-earth doped ZBLAN and Silica fibers.

Table 4.1 Laser transitions in fluoride fibers doped with rare earths.

Dopant	Possible co-dopant	Wavelengths [nm]
Pr^{3+}	Yb^{3+}	491,520,615,635,695, 715,885,910,1300
Nd^{3+}		381,412,1050,1350
Ho^{3+}	Tm^{3+}	550,1190,1850,2075, 2900
Er^{3+}	Pr^{3+}	550,850,1600,1700, 2710,3500
Tm^{3+}	Yb^{3+}, Tb^{3+}	455,482,810,1470, 1820,1900,2300
Yb^{3+}		1120,1020

Then, using fluorozirconate fibers allows laser action with low thresholds, high efficiency and numerous possibilities of pumping by up-conversion [12]. Some of the most important laser transitions are provided in **table 4.1** [9]. In addition to these transitions, others can be achieved by co-doping with different elements such as Sm and Dy.

4.5 Features of Tm^{3+} doped fibers

Tm^{3+} have several valuable emission wavelengths available in some glass hosts like silicon glasses and there are much more additional transitions in fluoride-based glasses. Some of these emissions that can be possible to obtain in both glasses can occur in the range of 1000 nm – 2000 nm.

The absorption spectrum for thulium (Tm^{3+}) immersed in silicon and fluoride glasses (specifically fluorozirconates) is very similar for both glasses, except that in fluorides the ultraviolet edge is shifted to shorter wavelengths and therefore Tm^{3+}-doped fluorozirconate has larger fundamental bands [7].

When examining thulium for radiative transitions that can provide gain for amplifiers or laser systems, one of the main considerations is the availability of metastable states. Unlike Er^{3+} and Nd^{3+}, in which there are metastable states obtainable for most glasses, in Tm^{3+} only the excited state levels $^3H_4$ and $^1G_4$ are metastable for most glasses. Since, in general, excited states have much shorter lifetimes and multi-phonon processes are much stronger.

In fluoride fibers, having very low phonon energies, the level $^3F_4$ is metastable (see **table 4.2** [13]), whereas *e.g.* $^3H_5$ is quenched by multi-phonon processes which transfer the ions to $^3H_4$. These circumstances make it possible to pump thulium ions efficiently into the upper levels, from where blue light can be emitted. This is exploited in some up-conversion fiber lasers [14].

Table 4.2 Energy level lifetimes comparison for Thulium in Silica and ZBLAN.

Transition	Tm: Silica $\tau_r(\mu s)$	Tm: ZBLAN $\tau_r(\mu s)$
$^3H_4 \rightarrow {}^3H_6$	4559	11223
$^3H_5 \rightarrow {}^3H_6$	3896	6863
$^3F_4 \rightarrow {}^3H_6$	697	1519
$^3F_3 \rightarrow {}^3H_6$	442	693
$^3F_2 \rightarrow {}^3H_6$	631	1234
$^1G_4 \rightarrow {}^3H_6$	428	908

Energy gaps for $^3H_5$, $^3F_3$ and $^3F_2$ levels are so small that multiphonon emission causes them to have very short lifetimes and it is unlikely that population inversion will occur for any of these levels (**table 4.3**), regardless of host material or temperature. The few effective gaps for some levels illustrate why the selection of the host material has so much influence on the efficiency of Tm^{3+}. The absorption and radiative transitions for thulium are shown in **figure 4.7** for most glasses.

Table 4.3 Energy gap to next Lower level for States of Tm^{3+}.

State	Energy Gap [cm^{-1}]
$^3H_4$	5400
$^3H_5$	2250
$^3F_4$	4150
$^3F_3$	1750
$^3F_2$	550
$^1G_4$	5950
$^1D_2$	6450

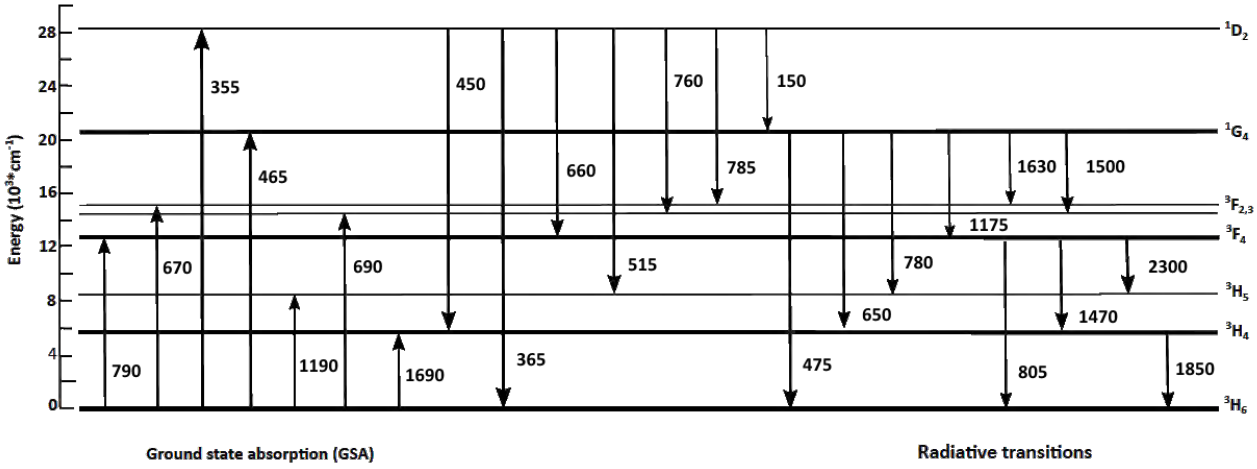

Figure 4.7 Energy level diagram of Tm^{3+} (Ground state absorption and radiative transitions) [nm].

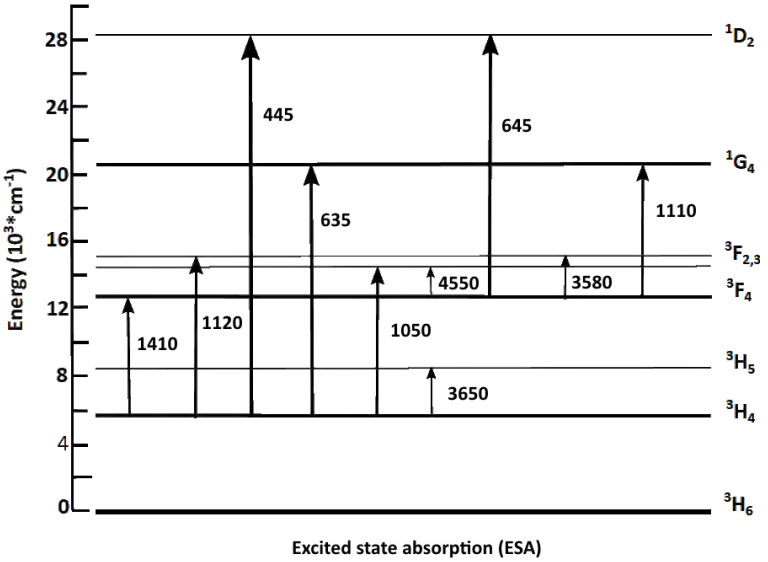

Figure 4.8 Excited state absorption transitions in Tm^{3+} [nm].

There are also excited absorption (ESA) states, which can be presented for numerous host materials. For thulium, the states with most of such transitions are $^3H_4$ and $^3F_4$, although others are also present, but less frequently (**figure 4.8**) [15].

There are several appreciated optical features in Tm^{3+}: ZBLAN; in particular, the up-conversion mechanism. The two most common excitation processes that lead to emission in the excited state absorption (ESA) are the up-conversion, shown in **figure 4.9,** and the energy transfer up-conversion (ETU), in which ions of different elements can participate; these processes allow to use the lifetimes of the upper excited states [16]. The difference between these processes is that up-conversion depends on a real intermediate state.

This state must have a finite lifetime that is long enough for an excitation to be store there for such a time as to allow a second excitation.

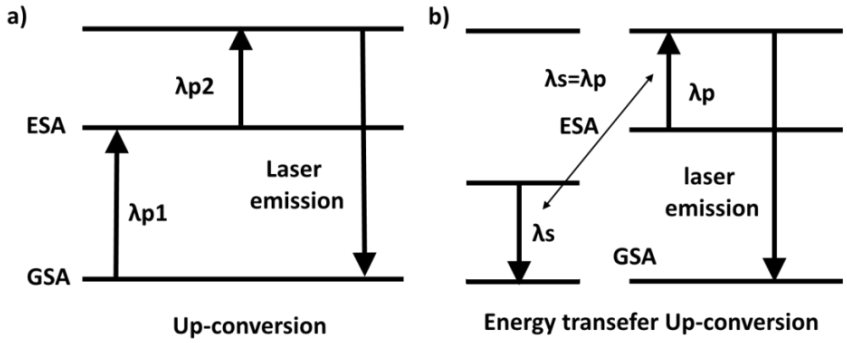

Figure 4.9 a) Up-conversion process; b) Energy transfer up-conversion.

4.6 Optical fibers as amplifiers and laser systems

A laser is an oscillator whose basic structure consists of an active medium in which there must be population inversion; this medium should be in the middle of two reflector systems (mirrors), which constitute a resonant cavity that confines light at a certain frequency. Mirrors can be replaced in optical fiber systems by FBGs or it could be a more complex system employing more than two reflecting systems.

These systems are based primarily on the *stimulated emission*. The atoms or molecules already excited can be stimulated by a pump to emit light with the same properties of the incident radiation, *i.e*. amplification in an active medium is when incident light (pump) increase the amplitude without changing the properties of the light, like the phase and frequency. These gain media may be pumped electrically (*e.g.*, electric discharge) or optically (*e.g.*, electromagnetic radiation). The active medium may be formed by several kinds of materials, such as: gaseous compounds, solid state devices or semiconductors. Some gain media for laser amplification are doped-crystals or glass-based waveguides that include the optical fibers.

When such a system is in a state of thermal equilibrium, there is a greater number of atoms in the ground state (N_1) than in the excited state (N_2), *i.e.*, $N_1 > N_2$ (in a non-degenerated system); therefore, only the mechanism of absorption exists (**figure 4.10**). Consequently, if the system is excited in some way or "pumped", so that population N_2 increases (*i.e.,* the relation $N_2 > N_1$ is fulfilled), then the pump will be amplified by the stimulated emission effect. This process is called "population inversion".

When a two-level system is excited, the number of ions in the upper level increases (population of this level increases) and so does the probability of de-excitation, regardless of the excitation power, there can be no population inversion. Therefore, there are systems with a greater number of levels to obtain laser action [17].

There are different amplification schemes for optical amplifiers and lasers. The simplest are the three- and four-level laser schemes. Where, $E_4 > E_3 > E_2 > E_1$ and $N_1 > N_2 > N_3 > N_4$, under thermal equilibrium.

In general, all schemes have a ground state (E_1) which, without excitation, contains the total population of ions within this level, *i.e.*, N_1 = 100%.

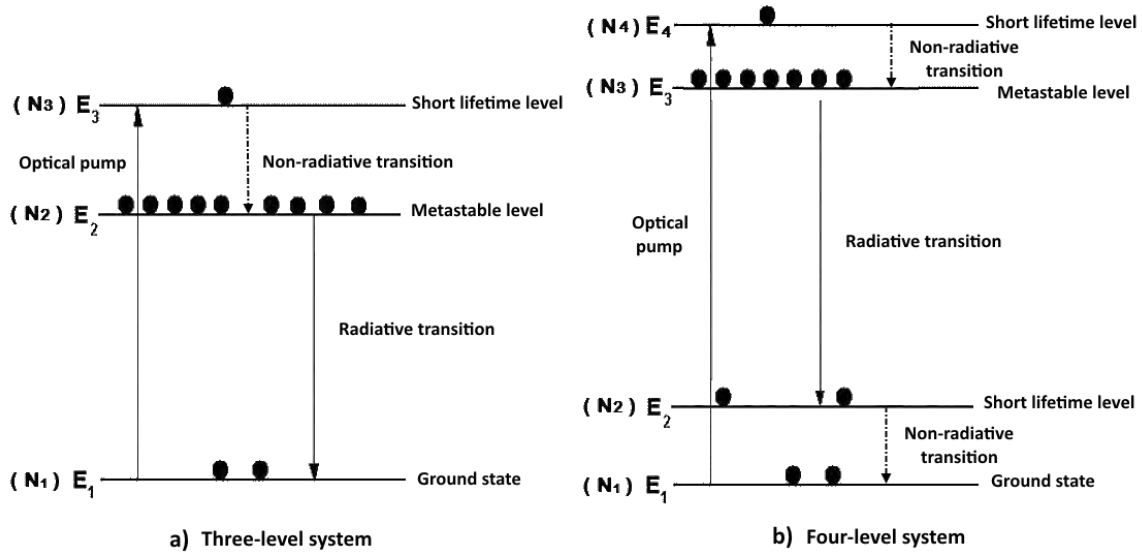

Figure 4.10 Energy level diagrams of different laser systems. a) Three-level system, b) four-level system.

For a three-level scheme (**figure 4.10a**), when there is an excitation proportional to the energy of ΔE_{13}, part of the population density N_1 rises to the E_3 energy level whose population density is N_3; since there is a rapid transition (*i.e.*, lifetime level in order of 10^{-9} s – 10^{-6} s) to the E_2 level by phonon emission this population is negligible. Phonon energies are proportional to the molecular kinetic energy of the material in which the active ions are immersed, and this transition is given in the form of heat generation. For this three-level scheme the E_2 level is the metastable state (*i.e.*, lifetime ~10^{-3} s for ZBLAN).

Lifetimes depends intrinsically on the glass or crystal in which the ion is immersed. *e.g.*, the lifetime for $^3F_4$ level in Tm^{3+}: ZBLAN is greater (~10^{-3} s) that if it were immersed in the SiO_2 which is of the order of 10^{-6} s [6]. The population tends to accumulate at the metastable state, having population inversion ($N_2 > N_1$). When ions decay, they emit

photons with energy ΔE_{21}, going back to the ground state E_1. This may occur due to the *spontaneous emission*, once the ion´s lifetime has been fulfilled at this level.

In order for amplification of the signal to take place, it is necessary that *stimulated emission* occur, *i.e.* when an incident, usually small, signal is absorbed having energy proportional to *e.g.* ΔE_{12}, it enforces ions in the E_2 level (population N_2) to decay emitting identical photons propagating in the same direction. The signal produced in this way is considered an amplified signal that continues growing up as it propagates through the material.

The same reasoning applies in the case of the four-level system (**figure 4.10b**), but for this scheme the population inversion condition is $N_3 > N_2$, since the metastable state is the E_3 level.

One disadvantage of the three-level amplification system is that more than half of the population must be pumped to the upper level E_3 to satisfy the population inversion $N_2 > N_1$ condition. Therefore this system is less efficient than a four-level system.

4.7 Population dynamics for a three-level system

The equations for population dynamics of an optical amplification system are temporal dependent and represent the rate of change of the ion population at each energy level under optical excitation. This system of equations also provides information about whether population inversion is achievable in certain transition and what would be the minimum pump power required to maintain a stable population inversion for CW laser emission [18].

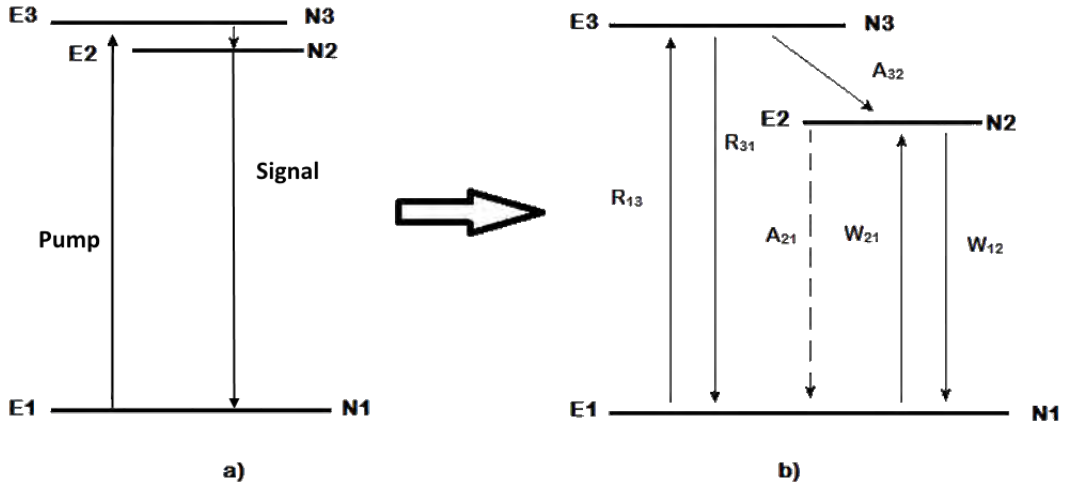

Figure 4.11 Three level system. a) Diagram representing a three-level system with a short life time τ_{32}. b) Equivalent three-level system.

Consider a three-level system (**figure 4.11**), with energy levels $E_3 > E_2 > E_1$ and with corresponding populations N_3, N_2 and N_1. The rates of excitation and de-excitation per unit of time for certain intensity can be expressed as a function of energy and the cross-sections of the active ions as follows:

$$R_{13} = \frac{I_p \sigma_a(\lambda_p)}{\hbar \omega_p} \quad \text{and} \quad R_{31} = \frac{I_p \sigma_e(\lambda_p)}{\hbar \omega_p}. \tag{4.1}$$

The corresponding signal rates are

$$W_{12} = \frac{I_s \sigma_a(\lambda_s)}{\hbar \omega_s} \quad \text{and} \quad W_{21} = \frac{I_s \sigma_e(\lambda_s)}{\hbar \omega_s}. \tag{4.2}$$

The relaxation rate can be expressed as a function of the lifetime, as

$$A_{21} = \frac{1}{\tau_{21}} \quad \text{and} \quad A_{32} = \frac{1}{\tau_{32}} \tag{4.3}$$

For **equation 4.1** to **equation 4.3** λ_p is the pump wavelength, λ_s is the signal wavelength, $\hbar$ is 2π multiplied by the Planck constant, ω_p and ω_s are the pump and signal frequencies, respectively.

The intensity of pump and signal are I_p and I_s [W/m^2] and the lifetime is τ. The absorption and emission cross-sections correspond to σ_a and σ_e. The small signal of attenuation can be expressed as

$$\alpha_0 = \sigma \cdot N \tag{4.4}$$

N is the concentration of ions / cm^3 and α_0 is the attenuation [cm^{-1}].

The rate of relaxation or radiative transition has units of [s^{-1}], which determines the probability of transition from one level to another. These parameters determine the physics of the system and are dependent on the energy and pump wavelength, as well as the cross-section area of the active ions of the medium, in this case the optical fiber.

If the system is a non-degenerate system, *i.e.*, the de-excitation rates for the signal and pump are equal to the excitation rates, then it can be assumed that

$$R_{31} = R_{13} = R \tag{4.5}$$

$$W_{21} = W_{12} = W \tag{4.6}$$

The population density (N_i) is distributed among the levels according to the following equations,

$$\frac{dN_1}{dt} = -N_1(W_{12} + R_{13}) + N_2(A_{21} + W_{21}) + N_3R_{31} = -R(N_3 - N_1) + W(N_2.N_1) + N_2A_{21} \quad 4.7$$

$$\frac{dN_2}{dt} = -N_2(W_{21} + A_{21}) + N_1W_{12} + N_3A_{32} = W(N_1 - N_2) + N_3A_{32} - N_2A_{21} \quad 4.8$$

$$\frac{dN_3}{dt} = -N_3(R_{31} + A_{32}) + N_1R_{13} = R(N_1 - N_3) - N_3A_{32} \quad 4.9$$

$$N_t = N_1 + N_2 + N_3 \quad 4.10$$

Equation 4.10 represents the conservation of energy, since the total population is the sum of populations of all levels (*i.e.,* concentration of ions at each energy level).

For solving these equations, it is assumed that the system operates under the condition of CW, *i.e.*, a stable system where the population density rate is constant in time for each energy level.

We can solve the system of equations applying these assumptions. By clearing N_3 from **equation 4.9**,

$$N_3 = \frac{N_1R}{R + A_{32}} \quad 4.11$$

From **equation 4.8** and **equation 4.11** it can be obtained that:

$$N_2 = \frac{N_1}{W + A_{21}}\left(W + \frac{RA_{32}}{R + A_{32}}\right) \quad 4.12$$

In order to obtain laser amplification, the population inversion condition must be fulfilled $N_2>N_1$. To obtain the necessary conditions to satisfy the population inversion condition, using equation **4.5** to **equation 4.10,** it is obtained

$$\frac{N_2 - N_1}{N_t} = \frac{R(A_{32} - A_{21}) - A_{32}A_{21}}{3RW + 2RA_{21} + 2A_{32}W + A_{32}R + A_{32}A_{21}} \quad 4.13$$

To obtain population inversion, it is necessary that: N_2-N_1>0, therefore the necessary condition applied for the three-level system is

$$R(A_{32} - A_{21}) > A_{32}A_{21} \quad 4.14$$

For this particular system, the lifetime of the third level is extremely small, *i.e.*, it is negligible and therefore the rate of transition probability is very high. Then in practice, this level may be a wide level so that the pump source can have a considerably bandwidth so that it can be used efficiently. In addition, a minimum pump power must be satisfied, **equation 4.10** to **equation 4.13**,

$$R_{Threshold} = \frac{A_{32}A_{21}}{A_{32} - A_{21}} \quad 4.15$$

Consequently, to obtain population inversion it is required that $R > R_{threshold}$. However, for low laser powers, *i.e.*, $W << A_{21}$, and if $A_{32} >> A_{21}$, from **equation 4.13**

$$\frac{N_2 - N_1}{N_t} \cong \frac{R - A_{21}}{R + A_{21}} \tag{4.16}$$

For this approximation, it is required that $R > A_{21}$ to obtain population inversion.

Let $\Delta N = N_2 - N_1$, rewriting **equation 4.16** as follows

$$R(N_t - \Delta N) = A_{21}(N_t + \Delta N) \qquad \rightarrow \qquad \frac{R}{A_{21}} = \frac{N_t + \Delta N}{N_t - \Delta N} \tag{4.17}$$

N_3 does not contribute, therefore the system can be simplified,

$$N_t = N_1 + N_2 + N_3 \cong N_1 + N_2 \tag{4.18}$$

So, to keep population inversion, the pump power must meet the minimum energy requirement

$$P_p = N_2 \hbar \omega_p A_{21} \tag{4.19}$$

There are several types of amplifier systems that operate on a three-level system; like doped systems with: Yb^{3+}, Er^{3+}, Tm^{3+} and Ho^{3+}. All these systems have in common that the higher levels are very close to each other.

For a more complex system, the corresponding equations of each level are added, *e.g.*, for a four-level system there will be four equations for population densities, plus the energy conservation equation and so on; according to the number of levels of the system.

4.8 Amplification and laser oscillation

If there is a system where absorption exists, the power of the light absorbed by a medium where there is a distribution of levels N_1 and N_2 as a function of medium´s length, can be expressed as

$$\frac{dP(z)}{dz} = -(N_1 - N_2)\frac{\hbar \omega B}{c} P(z) = -\alpha(\omega) P(z) \tag{4.20}$$

B corresponds to the probability for stimulated emission (Einstein coefficient), where absorption is defined as

$$\alpha(\omega) = -\Delta N \frac{\hbar \omega B}{c} = -\Delta N \sigma(\omega) \tag{4.21}$$

To create amplification in a medium, there must be a negative absorption α, *i.e.*, optical gain g. By integrating **equation 4.20**, this equation becomes,

$$P(z) = P(0)e^{-\alpha z} = P(0)e^{gz} \tag{4.22}$$

Rewriting **equation 4.20** for non-degenerate systems, then

$$\frac{dP(z)}{dz} = \Delta N\sigma(\omega)P(z) = g(\omega)P(z) \qquad 4.23$$

If a system is degenerated, then equation **4.20** becomes

$$\frac{dP(z)}{dz} = [N_2\sigma_{21}(\omega) - N_1\sigma_{12}(\omega)]P(z) \qquad 4.24$$

Consider the case of a RE-doped optical fiber, then the variation of the pump power $P_p(z)$, when it travels along the fiber, is given by

$$\frac{dP_P(z)}{dz} = g_p P_p = \left[N_2\sigma_{21}(\omega_p) - N_1\sigma_{12}(\omega_p)\right]P_p \qquad 4.25$$

For the signal power P_s is

$$\frac{dP_s(z)}{dz} = g_s P_s = \left[N_2\sigma_{21}(\omega_s) - N_1\sigma_{12}(\omega_s)\right]P_s \qquad 4.26$$

In the case where there is no pump the population in the upper level N_2 is near 0, and then the total population will be at the ground state, then $N_t = N_1$. Therefore, all the ions can be then absorbed from the ground state. This is called the small signal absorption,

$$\alpha_0(\omega) = N_1\sigma_{12}(\omega) = N_T\sigma_{abs}(\omega) \quad \text{and} \quad g_P = -\alpha_0(\omega) \qquad 4.26$$

Absorption is an optical phenomenon independent of the intensity, *i.e.*, linear absorption. But in the case of intense electric fields, the polarization of the light becomes nonlinear, as well as the susceptibility χ and therefore, so does the absorption and the refractive index. These nonlinear effects include the “absorption saturation”. When the intensity of light increases, the absorbed power increases linearly when the intensity is weak, if the light is strong, the absorption coefficient gradually becomes small and the absorbed power approaches a certain saturation value. As the absorbed power is no longer proportional to the incident power, this effect is called "absorption saturation” or “nonlinear absorption" (**figure 4.12**), and this is expressed as a function of the density of the incident power, as

$$\alpha(P_p) = \frac{\alpha_0}{1 + \dfrac{P_p}{P_p^{sat}}} \qquad 4.27$$

When the pump saturation power equals the value of the pump power, then the absorption coefficient fulfils the following condition, where a is the fiber core area.:

$$P_p^{sat} = P_P = \frac{\hbar\omega_p a}{\sigma_a\tau} = \frac{\Delta E a}{\sigma_a\tau} \quad \text{then } \alpha = \frac{\alpha_0}{2} \qquad 4.28$$

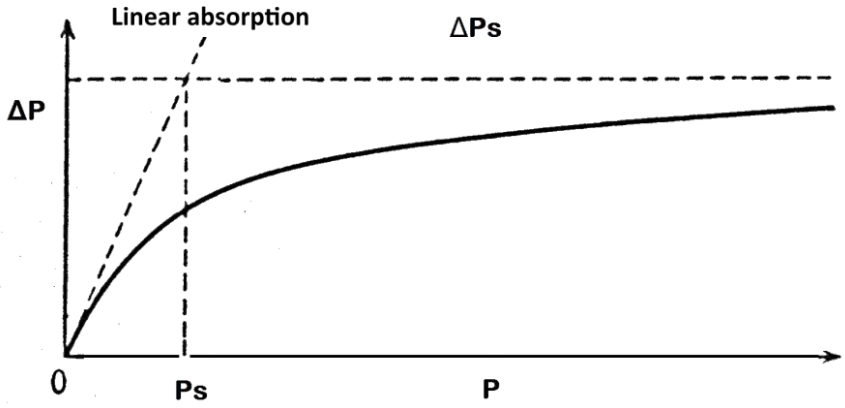

Figure 4.12 Absorption saturation as a function of incident power. Where P_s is the saturation power and ΔP_s is the saturation value of the power absorbed.

Let $I_{p,s}$ be the incident photon flux, in terms of the power density $P_{p,s}$ of the incident light, then it can be defined as

$$I_p = \frac{P_p}{a} \quad \text{and} \quad I_s = \frac{P_s}{a} \tag{4.29}$$

The absorption coefficient can be written as a function of the intensity as

$$\alpha(I_p) = \frac{\alpha_0}{1 + \frac{I_p}{I_p^{sat}}} \tag{4.30}$$

The gain constant of a medium with population inversion can also be saturated. For a weak incident light, it can be called the unsaturated gain coefficient g_0, which can be visualized as a weak signal that does not significantly redistribute the population. More powerful signals that do redistribute the population tend to experience lower gain, this gain constant is defined as

$$G(P_s) = \frac{g_o}{1 + \frac{P_s}{P_s^{sat}}} \quad \text{and} \quad G(I_s) = \frac{g_o}{1 + \frac{I_s}{I_s^{sat}}} \tag{4.31}$$

Where P_s^{sat} is the saturation power of the signal, $P_s^{sat} = \frac{\hbar \omega_s a}{\sigma_e \tau}$

It is also possible to calculate losses on an optical fiber based on its length (l) and input power (P_{in}), fulfilling the Beer-Lambert law,

$$P_{out} = P_{in} \exp(-\alpha_0 l) \tag{4.32}$$

Let the transmittance T be a function of the absorbance A; where $T + A = 1$. Then the transmittance in terms of the input and output powers is expressed as

$$\mathrm{T} = \frac{\mathrm{P_{out}}}{\mathrm{P_{in}}} = \exp(-\alpha_0 l) \qquad 4.33$$

Where the small signal absorption is given by

$$\alpha_0[cm^{-1}] = \frac{-\ln T}{l} \qquad 4.44$$

4.9 Optimal fiber length for fiber lasers

REDF laser systems need to fulfill the population inversion condition along their entire length for obtaining the highest possible efficiency and thus avoid losses by re-absorption of the signal at the end of the fiber. If the fiber is too short there will not be sufficient absorption of the signal, on the other hand if the fiber is too long there will be absorption of the laser signal at the output end and therefore the power output will be very poor.

It is then necessary to determine the optimum length at which a fiber laser will obtain the highest efficiency, *i.e.*, the highest possible gain. To obtain the optimal fiber length this would depend on important parameters, such as: dopant concentration (ppm/wt.), absorption efficiency and pump power. Considering these parameters, optimal fiber lengths fluctuates between a few centimeters to a few meters.

For this, a two-level fiber laser will be modeled, since a three-level system can be simplified to one of a two-level system [19]. Two signals generated by the stimulated emission from an incident pump power, which propagates in opposite directions, will be considered as in **figure 4.13**.

Let the normalized total power at any point along the fiber dependent on the saturation power of the signal:

$$\frac{P_s(z)}{P_s^{sat}} = p(z) = A(z) + B(z) \qquad 4.45$$

where propagation signals within the fiber are defined as

$$A(z) = \frac{P_s^{+}(z)}{P_z^{sat}} \qquad \text{and} \qquad B(z) = \frac{P_s^{-}(z)}{P_z^{sat}} \qquad 4.46$$

Let the normalized signal and pump powers be,

$$p = \frac{P_s}{P_s^{sat}} \qquad \text{and} \qquad q = \frac{P_p}{P_p^{sat}} \qquad 4.47$$

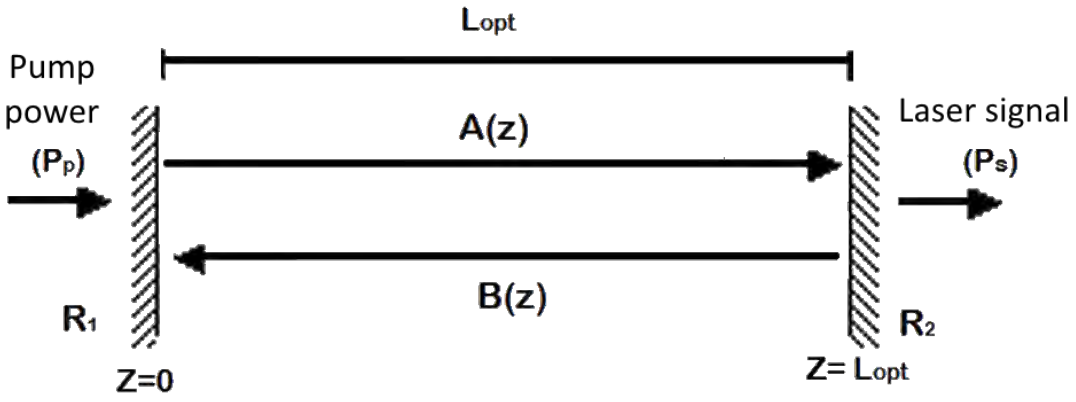

Figure 4.13 Laser resonator scheme composed of two mirrors with reflectivity R_1 and R_2.

Let the rate of change of the absorbed normalized power for signal and the pump dependent on the position along the fiber, and the ratios of the emission and absorption cross sections, derived from the two- level system [18]:

$$\frac{dq}{dz} = \frac{-\alpha_p q(U'p+1)}{1+p+q} \quad \text{and} \quad \frac{dp}{dz} = \frac{\alpha_s p(Uq-1)}{1+p+q} \tag{4.48}$$

with U' and U defined as

$$U' = \frac{\eta_s - \eta_p}{1+\eta_s} \quad \text{and} \quad U = \frac{\eta_s + \eta_p}{1+\eta_p} \tag{4.49}$$

where $\eta_i = \frac{\sigma_e(\omega_i)}{\sigma_a(\omega_i)} = \frac{\sigma_{21}(\omega_i)}{\sigma_{12}(\omega_i)}$ $\mathrm{i = s, p}$ represent the rates for the cross-sections of emission and absorption, for signal and pump.

Substituting **equation 4.46** into **equation 4.48** for the normalized power of the forward-propagating signal. The normalized pump power and the forward-propagating signal results in:

$$\frac{1}{A(z)}\frac{dA(z)}{dz} = \frac{\alpha_s(Uq-1)}{1+p+q} \qquad \frac{1}{q}\frac{dq}{dz} = \frac{-\alpha_p(U'p+1)}{1+p+q} \tag{4.50}$$

The ratio of the above equations obtains the propagation equation, as

$$\alpha_p(U'p+1)\frac{dA(z)}{A(z)} = \alpha_s(1-Uq)\frac{dq}{q} \tag{4.51}$$

Figure 4.13 establishes certain limits that can be set for the signal propagation equations. Let the pump power and the forward-propagating signal be evaluated at the limits of the cavity.

$$q(0) = q_o \qquad \text{and} \qquad \frac{\mathrm{d}A(L_{opt})}{\mathrm{dz}} = 0 \tag{4.52}$$

The pump power at the fiber input ($z = 0$) is it maximum value (q_0), and for the fiber end ($z = L_{opt}$), the pump power is minimally absorbed and the gain becomes saturated. Therefore $A(z)$ ceases to increase. Then applying the boundary criteria in **equation 4.50** we obtain that the value at which the derivative of $dA(L_{opt})/dz = 0$, when $q = 1/U$.

It is now possible to solve the differential equation, by integrating under the criteria of the limits in **equation 4.51**,

$$\int_0^{Lopt} \alpha_p (U'p + 1)\frac{dA(z)}{A(z)} = \int_{qo}^{1/u} \alpha_s (1 - Uq)\frac{dq}{q} \tag{4.53}$$

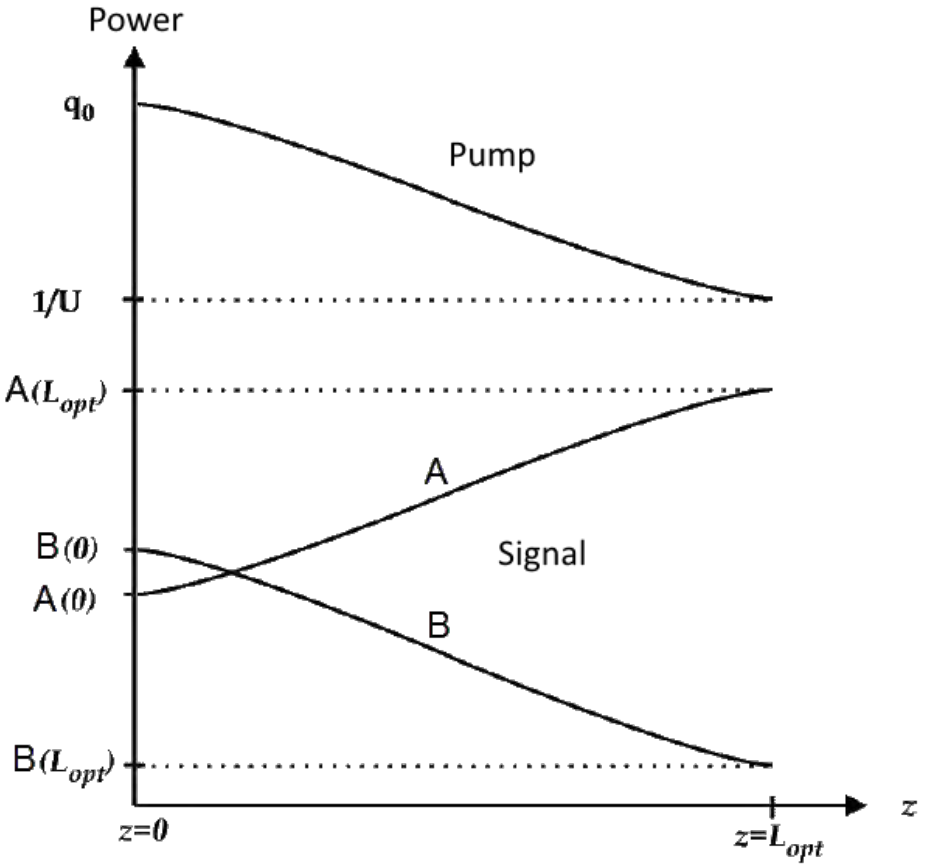

Figure 4.14 Normalized signal and pump power propagation along a two-level fiber laser.

Solving **equation 4.53**, we have

$$\alpha_p(U'p+1)\ln\left(\frac{A(L_{opt})}{A(0)}\right) = -\alpha_s\left(1-Uq_0+\ln(Uq_0)\right) \qquad 4.54$$

This equation will now be simplified in terms of known parameters, such as mirror reflectivities (R_1 and R_2), where the following boundary conditions are satisfied,

$$A(0) = R_1 B(0) \qquad \text{and} \qquad B(L_{opt}) = R_2 A(L_{opt}) \qquad 4.55$$

Because both signals experience the same gain as shown in **figure 4.14** [6], it is satisfied that $A(L_{opt}) = A(0)\exp(g \cdot L_{opt})$ and $B(L_{opt}) = B(0)\exp(-g \cdot L_{opt})$. Therefore,

$$A(L_{opt})B(L_{opt}) = A(0)B(0) \qquad 4.56$$

Using **equation 4.55** and **equation 4.56** we have

$$\frac{A(L_{opt})}{A(0)} = \frac{1}{\sqrt{R_1 R_2}} \qquad 4.57$$

Substituting **equation 4.57** into **equation 4.54**, we have

$$p = -\frac{\alpha_p \ln\left(\sqrt{R_1 R_2}\right) - \alpha_s\left(1-Uq_0+\ln(Uq_0)\right)}{\alpha_p U' \ln\left(\sqrt{R_1 R_2}\right)} \qquad 4.58$$

From **equation 4.50** for the normalized pump power, we have the following differential equation,

$$\int_{qo}^{1/U} \frac{(1+p+q)}{q} dq = \int_{0}^{Lopt} -\alpha_p(U'p+1)dz \qquad 4.49$$

By solving the integrals, the optimum length can finally be obtained

$$L_{opt} = \frac{\ln(Uq_0)(p+1) + q_0 + 1/U}{\alpha_p(U'p+1)} \qquad 4.60$$

4.10 Acknowledgements

Most of the content of this chapter is based on references [3,7 and 9].

4.11 References

1. W. H. Sulaiman, Selected Topics on Optical Fiber Technology (InTech, 2012).
2. P. Becker, A. O. Anders, and J. R. Simpson, Erbium-Doped Fiber Amplifiers: Fundamentals and Technology. (Academic press, 1999).
3. M. Digonnet, Rare-Earth-Doped Fiber Lasers and Amplifiers, Revised and Expanded (CRC Press, 2001).

4. L. Pauling, General Chemistry (Dover publishing, 1988).
5. L. de la. Pe a, Introduccion a La Mec nica Cu ntica (UNAM, 2010).
6. E. Mejía-Beltrán, "Rare-Earth Doped Optical Fibers," Sel. Top. Opt. Fiber Technol. (InTech 2012).
7. P. W. France, Optical Fibre Lasers and Amplifiers (CRC Press, Blackie and Son, 1991).
8. M. J. Weber, Handbook of Optical Materials (CRC Press, 2003).
9. M. Saad and J.-S. Tasse, "Fluoride glasses draw fiber into the mid-infrared," Laser Focus world **43**, 105–108 (2007).
10. E. Desurvire, Erbium-Doped Fiber Amplifiers Principles and Applications (Wiley, 1994).
11. K. Shimoda, Introduction to Laser Physics, Springer Series in Optical Sciences (Springer Berlin Heidelberg, 1986), Vol. 44.
12. D. Hewak, Properties, Procesing and Applications of Glass and Rare Earth-Doped Glasses for Optical Fibers (INSPEC Press,1988).
13. B. M. Walsh and N. P. Barnes, "Comparison of Tm: ZBLAN and Tm: Silica fiber lasers; Spectroscopy and tunable pulsed laser operation around 1.9 μm," Appl. Phys. B Lasers Opt. 78, 325–333 (2004).
14. D. V. Talavera and E. B. Mej a, "Blue up-conversion Tm3+-doped fiber laser pumped by a multiline Raman source," J. Appl. Phys. 97, 53102 (2005)
15. E. B. Mejía, "Ultraviolet emission in Tm3+ -doped fluoride fiber pumped with two infrared wavelengths," J. Appl. Phys. 100, 113110 (2006).
16. H. Xu and Z. Jiang, "Optical properties of Tm3+-doped fluorozirconate glass," Phys. Lett. A **299**, 85–88 (2002).
17. J. M. Senior and M. Y. Jamro, Optical Fiber Communications: Principles and Practice (Prentice Hall, 2009).
18. K. Thyagarajan and A. K. (Ajoy K. Ghatak, Lasers : Fundamentals and Applications (Springer, 2010).
19. E. Mejia, L. A. Zenteno, P. Gavrilovic, and A.K. Goyal, "High-efficiency lasing at 810 nm in single-mode Tm^{3+} doped fluorozirconate fiber pumped at 778 nm," Opt. Eng. **37**, 2699–2702 (1998).

Chapter 5

Red laser-diode pumped Tm^{3+}: ZBLAN fiber laser

Chapter 5

5. *Red laser-diode pumped Tm^{3+}: ZBLAN fiber laser*

5.1 Abstract

In the work described here, we report a proposal for a Tm^{3+}-doped fluorozirconate (ZBLAN) fiber laser operating in CW at 806 nm when diode-pumped at 687 nm. This system operates on the $^3F_4 \rightarrow {}^3H_6$ transition, and is suitable for first telecom window and sensing applications. A slope efficiency of 50.3% and low threshold pump-power of 11.6 mW were obtained. Maximum output power of 15 mW for 40 mW coupled pump was achieved.

5.2 Introduction

Fluorozirconate based glass fibers doped with rare earth ions have many properties that make them very suitable for fiber lasers and amplifiers. They have many metastable levels compared to silica-based fibers (*i.e.*, they usually present long excited state lifetimes in several energy levels). This is because fluorozirconate glass has lower phonon energies (approximately 500 cm^{-1}) than silica glass (~1100 cm^{-1}) [1], so that the multiphonon probability is reduced and hence the lifetime of many energy levels increases [2, 3] and some multiphonon decays from SiO_2 become photon emitting decays, increasing in this way the number of active transitions. Furthermore, these fibers have an extended transmitting window beyond silica in both UV and IR with background loss located around 3500 nm of one order of magnitude lower than that of silica [4]. The pump and signal overlap over long distances allows better pump absorption and signal amplification in this type of lasers and/or optical amplifiers. They also possess high inhomogeneous line broadening that makes possible to tune the emission and/or pump with multiline emitting sources in a large range of wavelengths. These features extend the possibilities for novel and more efficient designs for fiber laser schemes.

Most fiber laser and amplifier systems are based on rare-earth doped materials, among these Thulium-doped optical fibers are widely used. The selection of the host material is quite important, since this influences on its efficiency (this affects the lifetimes of the energy levels, since the difference between them is small and multiphonon emission is highly probable).

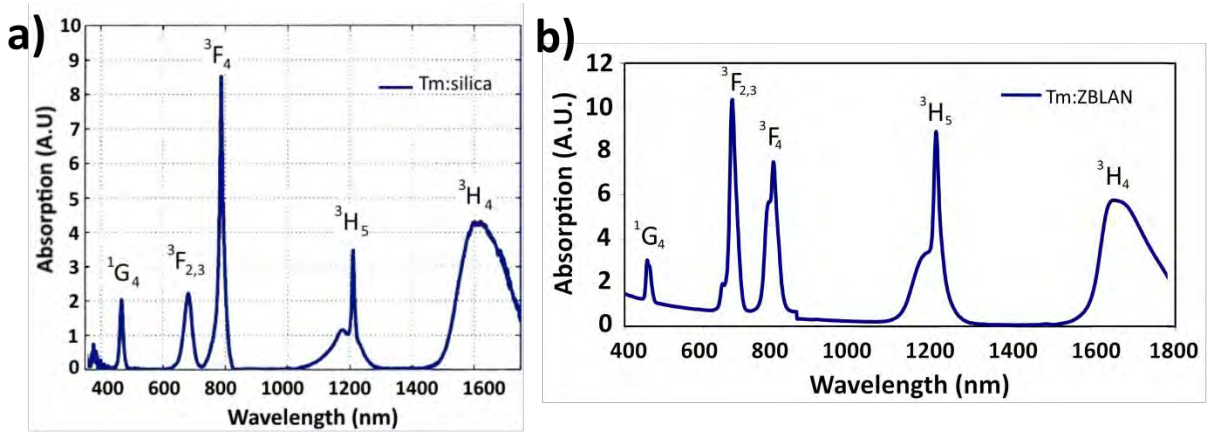

Figure 5.1 a) Tm: silica ground state absorption spectra; b) Tm: ZBLAN ground state absorption spectra

Tm^{3+}: ZBLAN has its stronger absorption band centered at ~690 nm (see **figure 5.1b**), unlike Tm^{3+}: silica that has its maximum absorption band centered at ~800 nm (**figure 5.1a**). This wavelength is commercially available wavelength from AlGaInP laser diodes. It corresponds to the $^3H_6 \rightarrow {}^3F_{2,3}$ transitions (energy levels $^3F_2$ and $^3F_3$ are in fact in thermal equilibrium owing to their small energy gap ~600 cm^{-1} [5]). Additionally, systems excited at this wavelength may experience a considerable mitigation of the photodarkening phenomenon present in these optical fibers [6-10]. Tm^{3+}: ZBLAN fibers can be efficiently pumped at around this wavelength to provide (among others) high gain at ~800 nm. This transition ($^3F_4 \rightarrow {}^3H_6$) is very efficient because it presents high radiative emission with a long lifetime (approximately 1.3 ms) [11].

Lasers and amplifiers operating in the first telecommunications window (800 nm – 850 nm) where silicon-based devices are cheap may find applications for short distance communications and local area networks. These lasers may be also useful for medical applications such as thermotherapy [12, 13] and bio-imaging [14, 15], located in the first biological window (680 nm – 940 nm) where there is a minimum of extinction coefficient produced by human tissue [16].

Tm^{3+}-doped fluoride glass has been extensively studied for obtaining these wavelengths not achievable in silica. Before our work reported here, this transition has been excited with a wavelength-fixed krypton ion laser at 676.4 nm [17] which is far from the 690 nm ground state absorption peak and hence they obtained just 1.6% conversion efficiency. It also has been excited (presenting the best efficiencies) at 780 nm with a Ti: Sapphire laser [18-20], under up-conversion with 1064 nm using a Nd: YAG laser [21, 22], with an Yb^{3+}-doped fiber laser emitting at 1108 nm [23], at 1120 nm with a Raman fiber

laser [24] and at 1319 nm pump using fluorogermanate glass as a host [25]. As one may note, apart from krypton-pump, little or no attention has been dedicated to this transition by pumping with more resonant (tunable) red laser diodes (LDs) at 690 nm [26] as described later on.

Light amplification in doped fibers development has been mostly driven by the ever-growing commercial availability of LDs as pumps because they continue covering more spectral regions. Therefore, it is highly desirable to use them as pump sources due to their high wall-plug efficiency and compactness that contribute to make fiber lasers and amplifiers also more compact and cheaper. These facts are essential to our motivations for investigating fiber devices pumped with LDs.

5.3 Theory, hypothesis and estimations

Before mounting our experimental setup, we considered a © FiberLabs Inc. Tm^{3+} doped ZBLAN glass optical fiber. The thulium concentration was 4500 ppm by weight (7.1063 x 10^{25} ions/m^3). It had a core diameter of 2.5 μm ± 0.3 μm and a NA 0.26 ± 0.02. Cutoff wavelength is 849 nm.

We obtained the absorption spectrum $\alpha(\lambda)$ [m^{-1}] considering our fiber concentration in the attenuation spectra of [27] and [28]. Once we obtained this coefficient then we could estimate the absorption cross-section spectrum, and from this, its corresponding emission cross-section spectrum (**figure 5.2a**), which is estimated by using the McCumber's relation [29] described by **equation 5.1**.

$$\sigma_{ems}(\lambda_s) = \sigma_{abs}(\lambda_p) \cdot \exp\left(\frac{hc}{kT}\left(\frac{1}{\lambda_0} - \frac{1}{\lambda_p}\right)\right) \qquad 5.1$$

Where *k* is the Boltzmann constant, *T* the absolute temperature, *h* is the Planck´s constant and λ_0 is the wavelength where emission and absorption cross-sections are equal (this corresponds to the centroid position of the energy level, usually given in cm^{-1}). For the transition $^3H_6 \rightarrow {}^3F_{2,3}$, λ_0 corresponds to 689nm [30,31].

When immersed in ZBLAN, Tm^{3+} ions can be pumped at the strongest absorption band (687 nm) from the $^3H_6$ ground state to the $^3F_3$ excited state; this will be followed by a rapid relaxation to the $^3F_4$ level and finally emission at ~806 nm takes place when returning to ground state (**figure 5.2b**). The cross-section absorption at 687 nm is calculated to be 4.08 x 10^{-25} m^2, which is close to the maximum absorption peak.

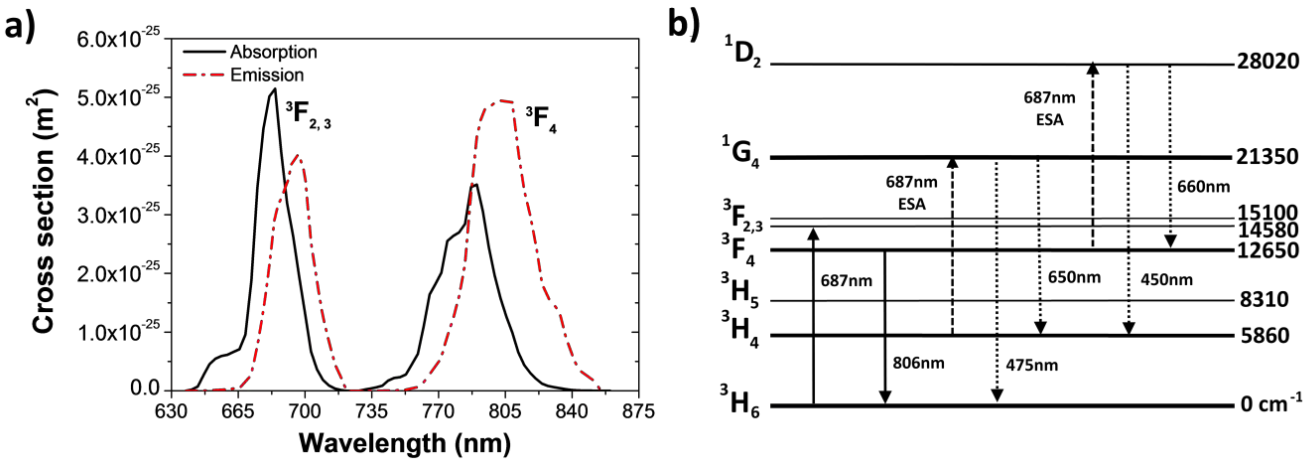

Figure 5.2 a) Estimated absorption and emission cross-section spectra of Tm^{3+}: ZBLAN; b) Partial energy level diagram of a Tm^{3+} ion in fluoride glass.

To obtain an optimal laser performance, an analytical approximate expression that estimates the optimal fiber length (L_{opt}) was used. This analysis is very similar to that used in [20] (described in **section 4.9**). To make this, we considered a Fabry-Perot cavity consisting of a Tm^{3+} doped fiber with length L with mirrors at the output ends (reflectivities R_1 and R_2 respectively). We normalized the pump power to the saturation power ($q_0 = P_p / P_{sat}$), and used the absorption coefficients α_p and α_s at λ_p=687 nm and λ_s =806 nm, respectively. We considered $\eta_{p,s}$ as the ratio of emission to absorption cross-section at pump and signal, used in **equation 4.58**.

Such system considers a simplified two-level approximation that under certain conditions might represent three or four-level pumping schemes although in general it is strictly valid when there exists a certain degree of spectral overlap between absorption and emission cross sections such that: $P_i^{sat} = h\nu_i a / [(\sigma_{abs}(\lambda_i) + \sigma_{ems}(\lambda_i)) \cdot \tau]$ with $i = p.s$ .Then we could have an estimation of the optimal fiber length (L_{opt}) as expressed in **equation 4.60**.

In our case we had reflectivities R_1 =0.99 and R_2 =0.04 and coupled a maximum of 40 mW (*i.e.*, ~60% of coupling efficiency); for this power and data supplied in **table 5.1**, the estimated optimal length was ~35 cm (**figure 5.3**). However, when probing fibers close to this length, total pump absorption was not achieved nor oscillation either.

Table 5.1 Supplementary data for numerical simulation.

Constant	Value
$\sigma_{abs}(\lambda_p)$ [a]	4.08 x10^{-25} m^2
$\sigma_{ems}(\lambda_p)$ [a]	3.28 x10^{-25} m^2
$\sigma_{abs}(\lambda_s)$ [a]	1.25 x10^{-25} m^2
$\sigma_{ems}(\lambda_s)$ [a]	4.94 x10^{-25} m^2
τ_{rad} ($^3F_4 \rightarrow {}^3H_6$) [b]	1.36 ms

[a] Values obtained from the calculated cross-section spectrum in **figure 5.1**.
[b] Value obtained from [31].

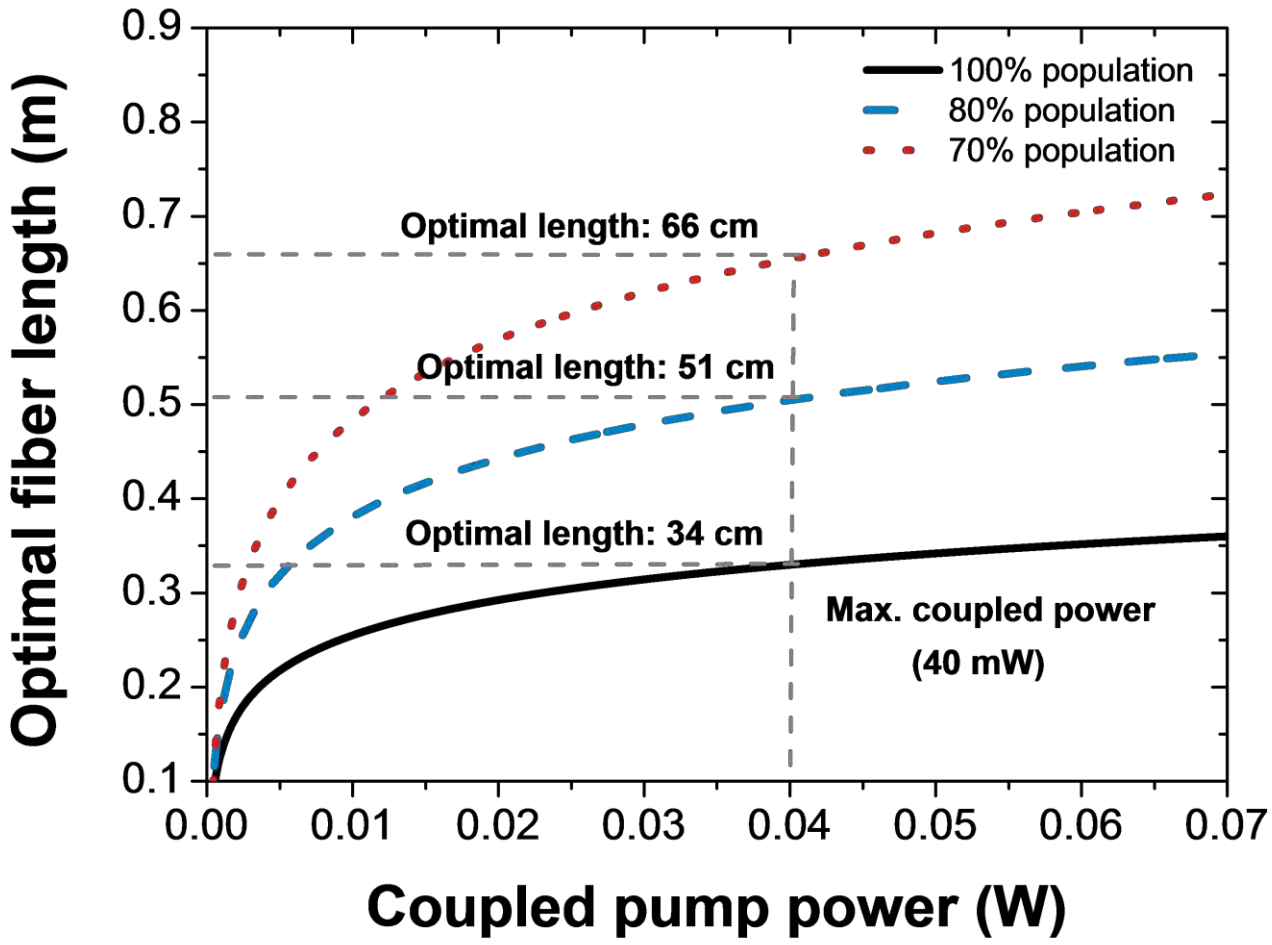

Figure 5.3 Calculated optimal fiber lengths for a two–level approximation.

Since we observed purple fluorescence that might be considered a combination of blue-violet with red, we assume that excited state absorption (ESA) takes place to populate $^1D_2$ and $^1G_4$ levels from where ~450 nm and 475 nm (blue) and 650 nm, 660 nm (red) lights are emitted (**figure 5.2b**); Here, we assume that part of the total population is being redistributed in these additional levels. Based on this, we used the two-level approximation probing with only 80% and 70% of the total population; the results were longer fiber lengths, giving 51 cm and 66 cm respectively (**figure 5.3**). We tried fiber lengths closer to these values (~70 cm) that operated reasonably. This is the fiber length that we chose for our experiments.

The NA of the fiber (0.26) implies a cut-off wavelength for mono-mode operation of 849 nm; it means that the fiber is multimode at both pump and signal wavelengths (non-total mode overlap); this might also be the source of errors in our optimal fiber length estimations.

5.4 Experiments

The experimental arrangement is shown in **figure 5.4** and in two photographs on **figure 5.5**. The Fabry-Perot cavity was formed by a high reflective (HR) dielectric mirror pressed against the launching end of the 0.7 m active fiber; we tried index-matching oil but it contaminated the fiber tip and degraded the coupling. The cavity was completed by the ~4% reflection derived from the fiber/air interface (Fresnel reflection) at the output end. The pump light was coupled by using a 10X microscope objective. The input dielectric mirror was highly reflecting (99%) at wavelengths greater than 800 nm and had a maximum transmission of 90% at 687 nm. All our experiments were performed at room temperature.

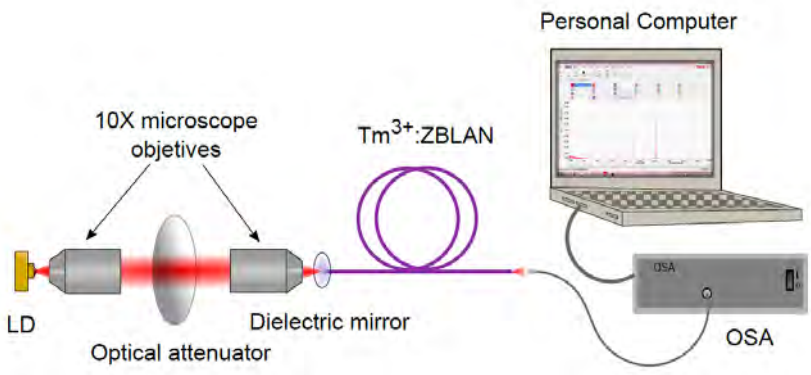

Figure 5.4 Experimental setup of a Tm^{3+}: ZBLAN laser.

With the purpose of finding the optimum pump wavelength for our experimental setup, we tuned the wavelength of the ©Opnext Inc. AlGaInP LD (680 nm – 689.5 nm) by using a non-commercial homemade temperature-controller that has a peltier electro-thermal device capable of regulating the temperature of a LD from 5 °C to 70 °C. Once the characterization (temperature vs. wavelength) of the LD was made, we applied the desired wavelength into our system. The wavelength that produced the highest pump absorption in our fiber was 687.6 nm ± 0.2 nm and the LD delivered a maximum power of 70 mW, it had a stable multi-mode spectral structure with a FWHM of ~0.4 nm. To control the input power coupled into the optical fiber, a variable optical attenuator was used.

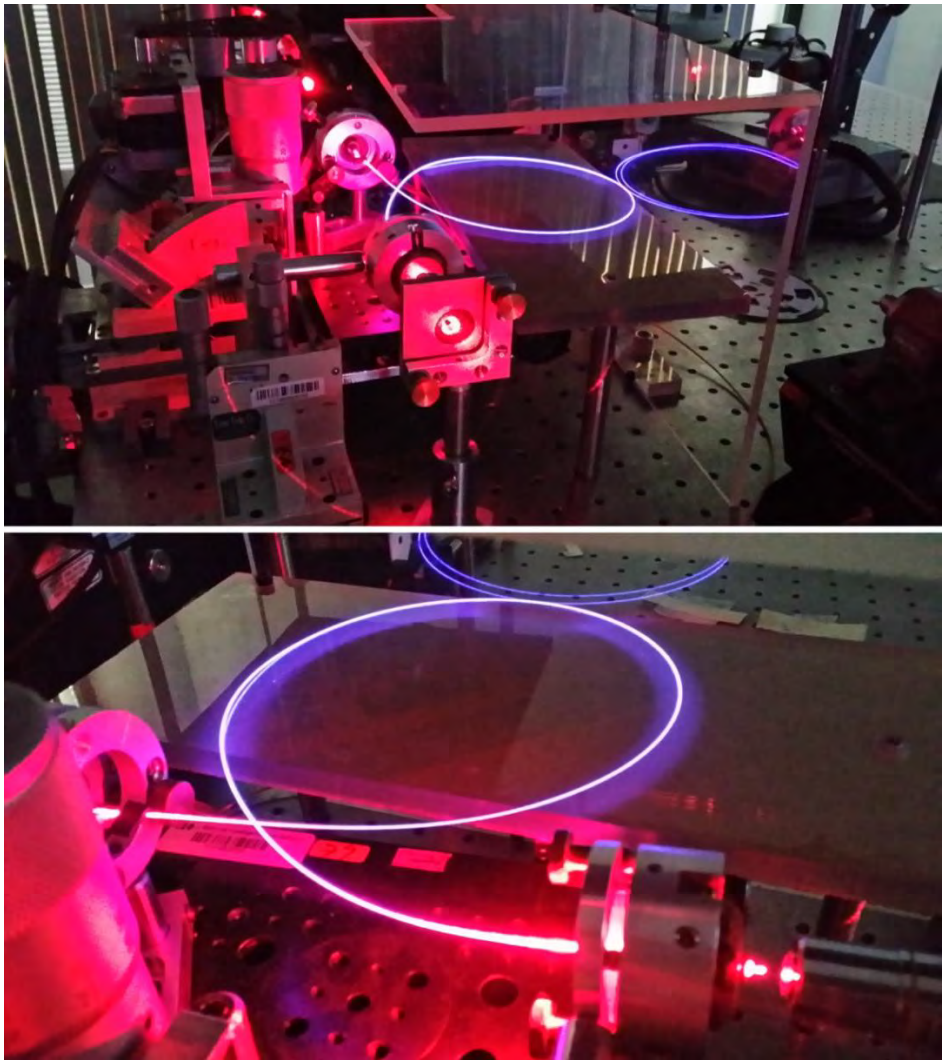

Figure 5.5 Photographs of experimental arrangement in laser operation (Tm: ZBLAN emitting 806nm and with purple fluorescence).

5.5 Results and discussions

The cavity emitted laser emission at around 806 nm when pumped above 11.6 mW coupled power. **Figure 5.6** presents the typical spectral evolution when gradually increasing pump. See that below threshold only ASE was obtained whereas above this only some modes located at the peak of the gain band compete; this is due to the dielectric mirror that had a quasi-flat reflecting spectrum covering more than ~45-nm wide (800 nm – 845 nm) (**figure 5.7**). The system behaved CW at higher frequencies (microseconds to milliseconds regime) and with certain instability (noisy) behavior in the order of seconds (**figure 5.8**). This is typical operation of the many modes lasing as a result of mode competition.

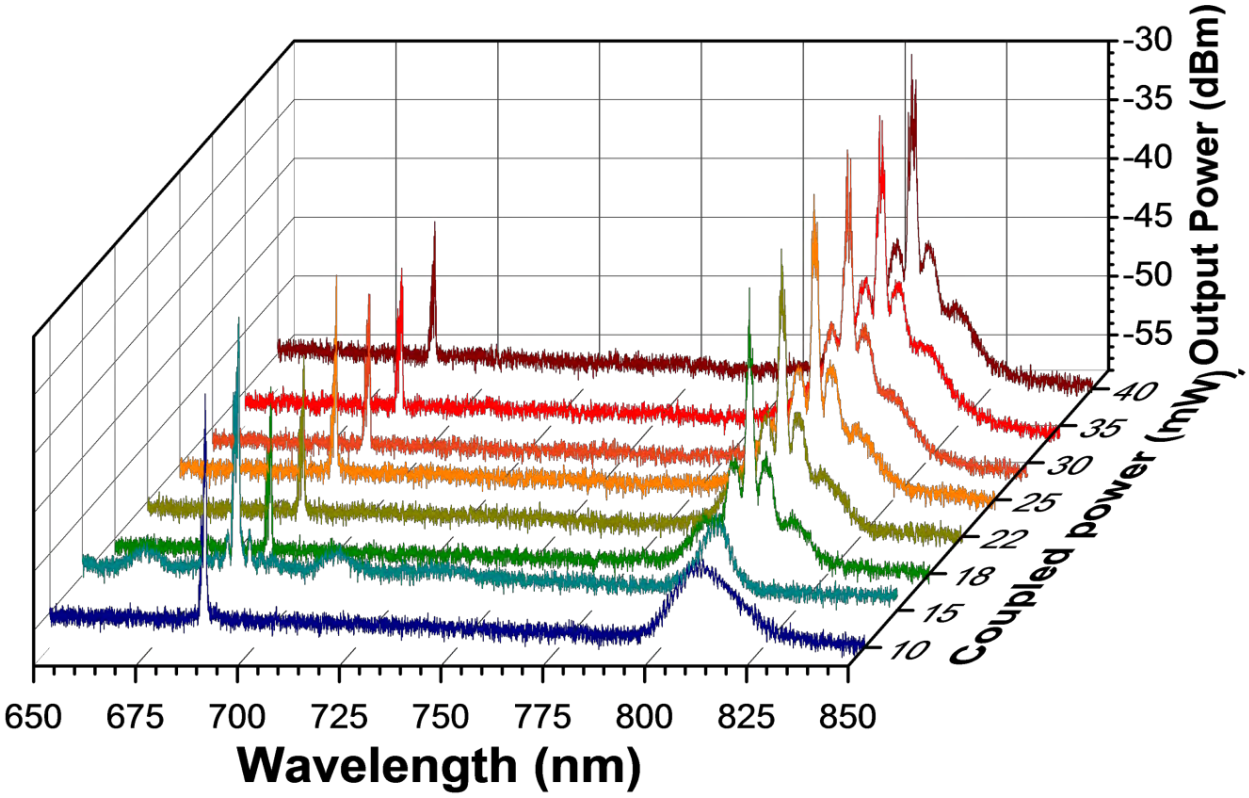

Figure 5.6 Pump dependent delivered spectra.

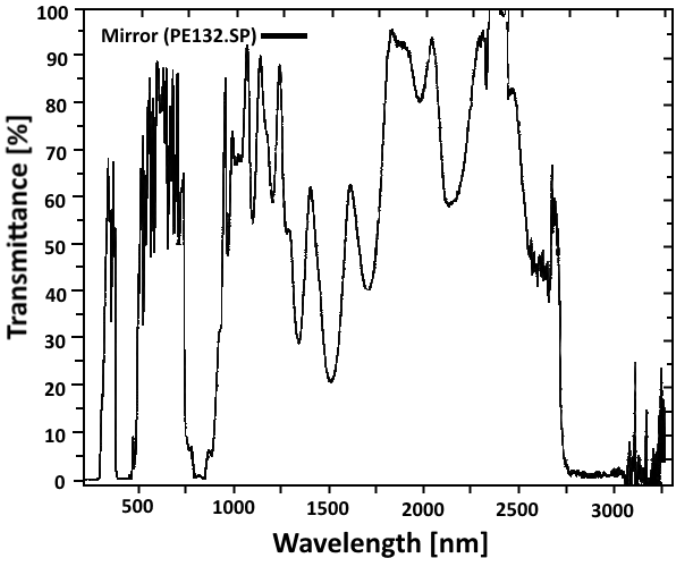

Figure 5.7 Transmittance of the PE132.SP dielectric mirror.

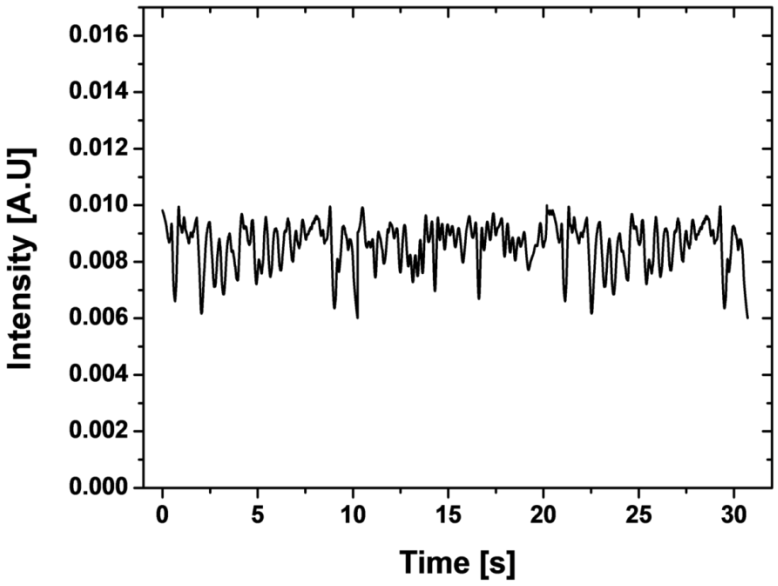

Figure 5.8 Typical temporal evolution of 806 nm signal at 40mW coupled pump when signal was spatially separated by a diffraction grating.

The slope efficiency above threshold was 50.3%. For the maximum-coupled pump power available in our experiments (40 mW) the output power was 15 mW (**figure 5.9**) giving an optical-to-optical conversion efficiency of 37.5%. Of the 40 mW coupled pump power, the optical fiber absorbed 36 mW representing 90% absorbed energy, this implies that in terms of efficiency the fiber length was close to optimum (**see figure 5.10**).

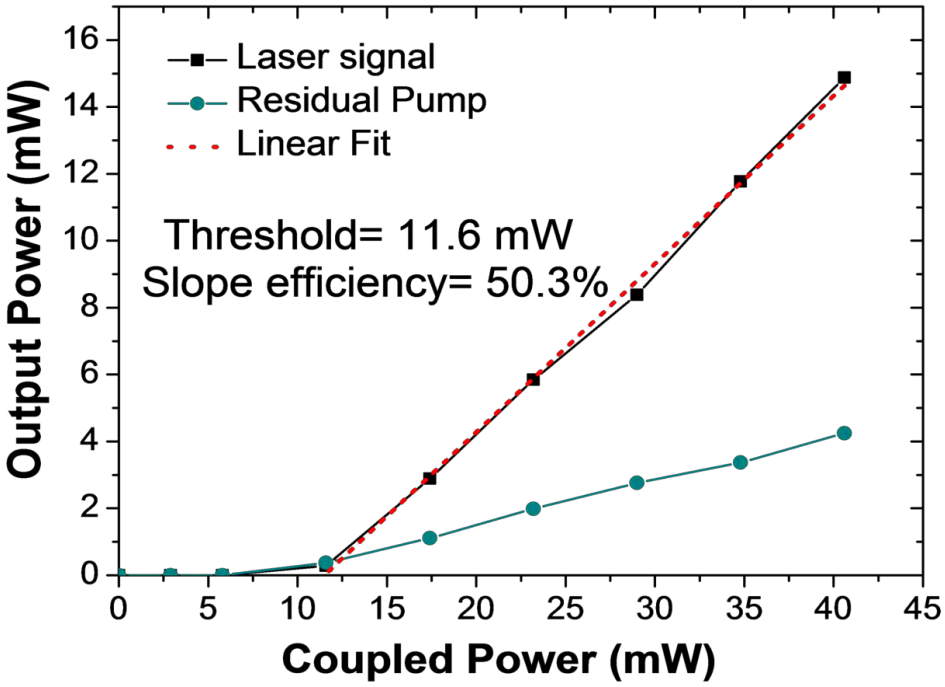

Figure 5.9 Delivered power as a function of pump power.

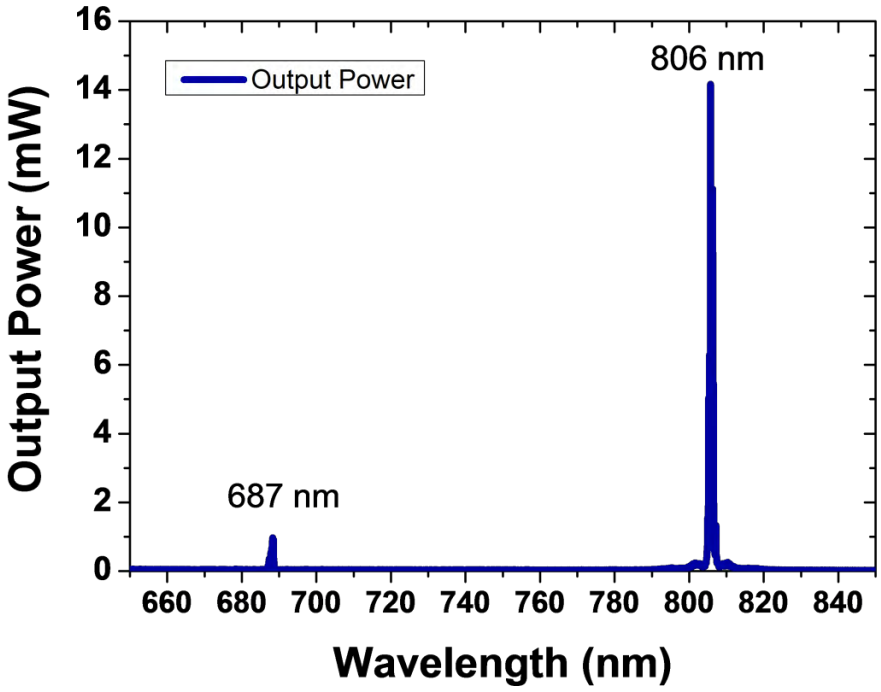

Figure 5.10 Laser signal at 806nm at 40 mW coupled pump.

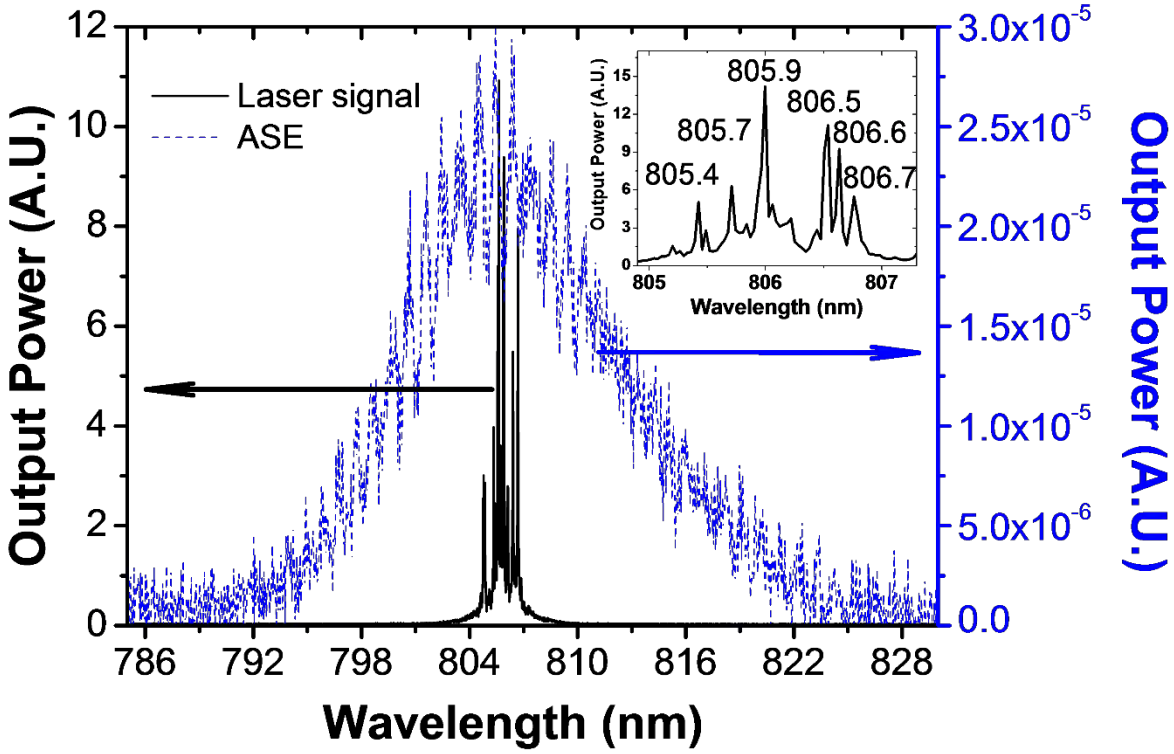

Figure 5.11 Tm^{3+}: ZBLAN laser signal and ASE signal comparison spectra.

The spectral emissions below threshold (ASE-emission) and above threshold are shown in **figure 5.11**; the broader one is obtained at 10 mW coupled, corresponding to the ASE band covering from 790 nm – 825 nm whereas the narrow one belongs to the laser signal at maximum pump power. The spectral linewidth (FWHM) of the laser signal is estimated to be ~0.7 nm compared to ~ 13.6 nm of the ASE signal; *i.e.* it is almost 19 times wider.

See that there is multi-frequency operation. This is due to oscillation axial and transversal modes in the cavity. Although the mode structure suffered changes as pump power changed, they were very stable at fixed powers. These spectral lines are less than 0.1 nm wide and covered ~1.6 nm from 805.2 nm to 806.8 nm; six of them can be easily identified (see inset of **figure 5.11**) having components at 805.4 nm, 805.7 nm, 805.9 nm (central line), 806.6 nm, and 806.7 nm. To achieve single-frequency operation a different experimental system using a different dielectric mirror with a narrower reflecting spectrum (less than 1 nm wide) or (although more challenging) using FBGs would be recommended.

5.6 Conclusions

In conclusion, we have demonstrated the possibility of using red laser diodes as an alternative for pumping 806 nm emitting Tm^{3+}-doped fluoride fiber lasers. Although reasonable high conversion efficiency close to 40% was obtained, some adjustments are required as the fiber was quasi multi-mode, dopant concentrations were possibly not optimum as well as fiber length. Pumping in this region offers several advantages as avoiding photodarkening and using cheap compact and commercial laser diodes. We believe this work is a departing point for considering changing the typical IR pumps. Also, an all-fiber configuration (*e.g.* using FBGs instead of dielectric mirrors) should be useful for single frequency operation. The laser configuration presented here could be an excellent prospect for sensing applications requiring modest powers. Also, this fiber laser can be modified to operate as an optical amplifier for local area network purposes.

5.7 Acknowledgement

Portions of this chapter have been presented at the Conference on Lasers and Electro-Optics (CLEO): Science and Innovations 2016, paper SM3Q.8 and formally published at the Laser Physics Letters Journal as: M. Juárez-Hernández and E. B. Mejía, "Red laser-diode pumped 806-nm Tm 3+: ZBLAN fibre laser," Laser Phys. Lett. **14**, 65103 (2017).

5.8 References

1. Peterka P, Kasik I, Dhar A, Dussardier B and Blanc W 2011 Theoretical modeling of fiber laser at 810 nm based on thulium-doped silica fibers with enhanced 3H4 level lifetime Opt. Express 19 2773
2. Zhu X and Peyghambarian N 2010 High-Power ZBLAN Glass Fiber Lasers: Review and Prospect Adv. Optoelectron. 2010 1–23
3. Zhou P, Wang X, Ma Y, Lü H and Liu Z 2012 Review on recent progress on mid-infrared fiber lasers Laser Phys. 22 1744–51
4. Tao G, Ebendorff-Heidepriem H, Stolyarov A M, Danto S, Badding J V., Fink Y, Ballato J and Abouraddy A F 2015 Infrared fibers Adv. Opt. Photonics 7 379
5. Walsh B M and Barnes N P 2004 Comparison of Tm: ZBLAN and Tm: Silica fiber lasers; Spectroscopy and tunable pulsed laser operation around 1.9 μm Appl. Phys. B Lasers Opt. 78 325–33
6. Barber P, Paschotta R, Tropper A and Hanna D 1995 Infrared-induced photodarkening in Tm-doped fluoride fibers Opt. Lett. 20 2195–7
7. Laperle P, Chandonnet A and Vallée R 1997 Photobleaching of thulium-doped ZBLAN fibers with visible light Opt. Lett. 22 178–80

8. Faucher D and Vallee R 2007 Real-Time Photobleaching and Stable Operation at 204 mW of a Tm : ZBLAN Blue Fiber Laser IEEE Photonics Technol. Lett. 19 112–4
9. Gebavi H, Taccheo S, LaBlonde L, Cadier B, Robin T, Monteville A, Le Goffic O, Landais D, Méchin D, Tregoat D, Milanese D, Leick L, Durrant T and Brandt T 2013 Photodarkening: investigation, mitigation and figure of merit Proceedings of SPIE - The International Society for Optical Engineering vol 8621, ed M J F Digonnet, S Jiang and J C Dries p 86210W
10. Piccoli R, Robin T, Brand T, Klotzbach U and Taccheo S 2014 Effective photodarkening suppression in Yb-doped fiber lasers by visible light injection Opt. Express 22 7638
11. Ramaswamy K, Jia C, Dastmalchi M, Chen L R and Saad M 2013 Dual-band 810/1480 nm Tm3+:ZBLAN fiber laser 2013 IEEE Photonics Conference (IEEE) pp 273–4
12. Holmer C, Lehmann K S, Risk J, Roggan A, Germer C-T, Reissfelder C, Isbert C, Buhr H J and Ritz J-P 2006 Colorectal tumors and hepatic metastases differ in their optical properties-relevance for dosimetry in laser-induced interstitial thermotherapy. Lasers Surg. Med. 38 296–304
13. Chen C-L, Kuo L-R, Lee S-Y, Hwu Y-K, Chou S-W, Chen C-C, Chang F-H, Lin K-H, Tsai D-H and Chen Y-Y 2013 Photothermal cancer therapy via femtosecond-laser-excited FePt nanoparticles Biomaterials 34 1128–34
14. Kuimova M K, Collins H A, Balaz M, Dahlstedt E, Levitt J A, Sergent N, Suhling K, Drobizhev M, Makarov N S, Rebane A, Anderson H L and Phillips D 2009 Photophysical properties and intracellular imaging of water-soluble porphyrin dimers for two-photon excited photodynamic therapy. Org. Biomol. Chem. 7 889–96
15. Escobedo J O, Rusin O, Lim S and Strongin R M 2010 NIR dyes for bioimaging applications. Curr. Opin. Chem. Biol. 14 64–70
16. Gouveia-Neto A S, Vermelho M V D, Jacinto C, Gouveia E A and Cassanjes F C 2016 Generation of Vis-NIR light within the first biological optical window via frequency upconversion in Tm 3+ - and Tm 3+ /Er 3+ -doped tellurite glass excited at 1319 nm SPIE LASE ed W A Clarkson and R K Shori (International Society for Optics and Photonics) p 97261K
17. Allain J Y, Monerie M and Poignant H 1989 Tunable CW lasing around 0.82, 1.48, 1.88 and 2.35 μm in thulium-doped fluorozirconate fibre Electron. Lett. 25 1660–2
18. Carter J N, Smart R G, Hanna D C and Tropper A C 1990 CW diode-pumped operation of 1.97 μm thulium-doped fluorozirconate fibre laser Electron. Lett. 26 599
19. Smart R G, Carter J N, Tropper A C, Hanna D C, Carter S F and Szebesta D 1991 20 dB gain thulium-doped fluorozirconate fibre amplifier operating at around 0.8 μm Electron. Lett. 27 1123
20. Mejia E, Zenteno L A, Gavrilovic P, and Goyal A K 1998 High-efficiency lasing at 810 nm in single-mode Tm3+ doped fluorozirconate fiber pumped at 778 nm Opt. Eng. 37 2699–702
21. Aggarwal I, Dennis M L and Dixon J W 1994 High power upconversion lasing at 810 nm, in Tm:ZBLAN fibre Electron. Lett. 30 136–7
22. Yang L-M, Sosnowski T, Stock M L, Norris T B, Squier J, Mourou G, Dennis M L and Durling III I N 1995 Chirped-pulse amplification of ultrashort pulses with a multimode Tm:ZBLAN fiber upconversion amplifier Opt. Lett. 20 1044
23. Androz G, Faucher D, Gingras D and Vallée R 2007 Self-pulsing dynamics of a dual-wavelength Tm^3+:ZBLAN upconversion fiber laser emitting around 800 nm J. Opt. Soc. Am. B 24 2907
24. Talavera D V. and Mej a E B 2005 Blue up-conversion Tm3+-doped fiber laser pumped by a multiline Raman source J. Appl. Phys. 97 53102

25. Gouveia-Neto A S, Vermelho M V D, Gouveia E A, Bueno L A and Jacinto C 2015 1.319 μm excited intense 800 nm frequency upconversion emission in Tm3+-doped fluorogermanate glass Appl. Phys. Lett. 107 211103

26. Juárez M and Mejía E 2016 Laser-conversion from a red laser-diode (687-nm) to IR (806-nm) by using a Tm^3+-doped ZBLAN optical fiber Conference on Lasers and Electro-Optics (Washington, D.C.: OSA) p SM3Q.8

27. France P W and Brierley M C 1990 Fluoride Glass Fibre Lasers And Amplifiers ed M J F Digonnet Proc. SPIE 1171 65–71

28. El-Agmy R M, Al-Hosiny N M, Abdallah S and Abdel-Aal M S 2014 Generation of Short Wavelength in Up-Conversion of Tm 3+ Doped Fluoride Glass and Its Application in Fiber Lasers J. Mod. Phys. 5 123–7

29. McCumber D E 1964 Einstein Relations Connecting Broadband Emission and Absorption Spectra Phys. Rev. 136 A954–7

30. Carnall W T, Fields P R and Rajnak K 1968 Electronic Energy Levels in the Trivalent Lanthanide Aquo Ions. I. Pr 3+, Nd 3+, Pm 3+, Sm 3+, Dy 3+, Ho 3+, Er 3+, and Tm 3+ J. Chem. Phys. 49 4424–42

31. Kozak M M, Goebel D, Caspary R and Kowalsky W 2005 Spectroscopic properties of thulium-doped zirconium fluoride and indium fluoride glasses J. Non. Cryst. Solids 351 2009–21

Chapter 6

Short wavelength emission by up-conversion in a Tm^{3+}: ZBLAN single and dual-diode-pumped optical fiber

Chapter 6

6. *Spectral analysis of short wavelength emission by up-conversion in a Tm^{3+}: ZBLAN single and dual-diode-pumped optical fiber*

6.1 Abstract

Emission at 450 nm, 475 nm and 365 nm by up-conversion in a Tm^{3+} doped ZBLAN optical fiber is spectrally analyzed. The fiber is diode-pumped by one or two red wavelengths, 687 nm and 645 nm, which help to reduce the photodarkening effect in the fiber.

6.2 Introduction

The need for obtaining short wavelength operation sources is constantly increasing. These types of light sources are already highly used in a huge range of disciplines and applications such as interferometry, laser microscopy, biomedicine, digital photofinishing, optical data storage, pump sources, laser projector displays, among others; since the relative short wavelength allows strong focusing, and helps resolving very fine structures for imaging applications.

These sources are often obtained from frequency doubling or tripling lasers emitting around 600 nm – 1100 nm. The most common lasers used for this purpose are, Nd: YAG (946 nm to obtain 473 nm and 1064 nm to get 355 nm) [1], Nd: YVO (914 nm to obtain 457 nm) [2], Nd: GAB (1062 nm to get 531 nm) [3] and Nd: $YAlO_3$ (930 nm to get 465 nm) [4]. Nevertheless, these kinds or lasers are usually bulky and they often need external cooling systems, increasing costs for operation and maintenance.

As an alternative to solid-state lasers systems, the up-conversion RE doped fiber lasers are excellent candidates. These have many properties that make them suitable for generating short wavelengths in the visible and UV regions. These systems barely have thermal problems, and have great conversion efficiencies. Among the REs, thulium (Tm^{3+}) is capable to convert low-energy, infrared (IR) photons, to high energy photons (in the visible region and in the UV); since the energy gaps between its levels are small and multiphonon emission is highly probable.

In particular Tm^{3+}: ZBLAN has attracted attention, since fluorozirconate glass has larger number of metastable levels compared to silica-based fibers, allowing a larger amount of radiative transitions.

Since the first report of blue up-conversion in fluoride glass fibers [5], short-wavelength laser operation in Tm^{3+}: ZBLAN has been demonstrated by many groups in the past, usually obtaining 480 nm pumped by IR laser sources (generally at 1064 nm and 1120 with Nd: YAG and Raman lasers) [6–9]. Also, wavelengths in the UV region (284 nm, 293 nm, 351 nm, and 360 nm) have been achieved by pumping with solid-state lasers such Nd: YAG at 1064 nm [10], with Ar+ laser at 485 nm and dye laser at 585 nm [11]. However, these systems often require absorption of three photons, which often have a tradeoff between ground state absorption (GSA) and excited state absorption (ESA), in addition to having small absorption (less than 5 dB/Km/ppm at 1064 nm, and 10 dB/km/ppm for 485 nm). They also present a factor that reduces the efficiency of their systems; when pumped with IR sources, it may produce a photodarkening effect [12, 13].

An alternative arrangement for obtaining short-wavelength emission in Tm^{3+}: ZBLAN is pumping with a dual-visible-wavelength configuration. Since the strongest absorption band of thulium-doped fluorozirconate is centered at around 690 nm ($^3H_6 \rightarrow {}^3F_3$) we proposed to use this wavelength as GSA [14]. Using this wavelength we can expect an optimal absorption (≥ 35 dB/Km/ppm) [15]; this represents a factor of 3.5 to 7 better than IR and some other visible (485 nm or 585 nm) pump sources. Additionally, by using ~645 nm ($^3F_4 \rightarrow {}^1D_2$) as ESA it is then possible to obtain a variety of radiative transitions in the UV (360 nm from $^1D_2 \rightarrow {}^3H_6$) and in the blue-visible region (450 nm from $^1D_2 \rightarrow {}^3H_4$ and 475 nm from $^1G_4 \rightarrow {}^3H_6$). An additional advantage is that these kinds of pump sources are already available from AlGaInP laser diodes (LDs), which are reasonably priced, have an extraordinarily large life span, in addition of being highly efficient and compact. Moreover, exciting at these wavelengths (red region) may experience a considerable mitigation of photodarkening [16–18], usually produced by IR pumping.

6.3 Experimental configuration

An AlGaInP LD operating at 687 nm was used as a pump source to be used as GSA to excite Tm^{3+} ions from the $^3H_6$ ground state to the $^3F_3$ excited state. A second LD was used to excite Tm ions via ESA operating at 645nm, to excite ions from the $^3F_4$ excited state to the $^1D_2$ upper level. Radiative transitions take place in the UV and visible when decaying to lower levels (360 nm from $^1D_2 \rightarrow {}^3H_6$ transition, 450 nm from $^1D_2 \rightarrow {}^3H_4$, 475 nm from $^1G_4 \rightarrow {}^3H_6$). The partial Tm^{3+} energy level diagram in fluoride glass is illustrated in **figure 6.1**.

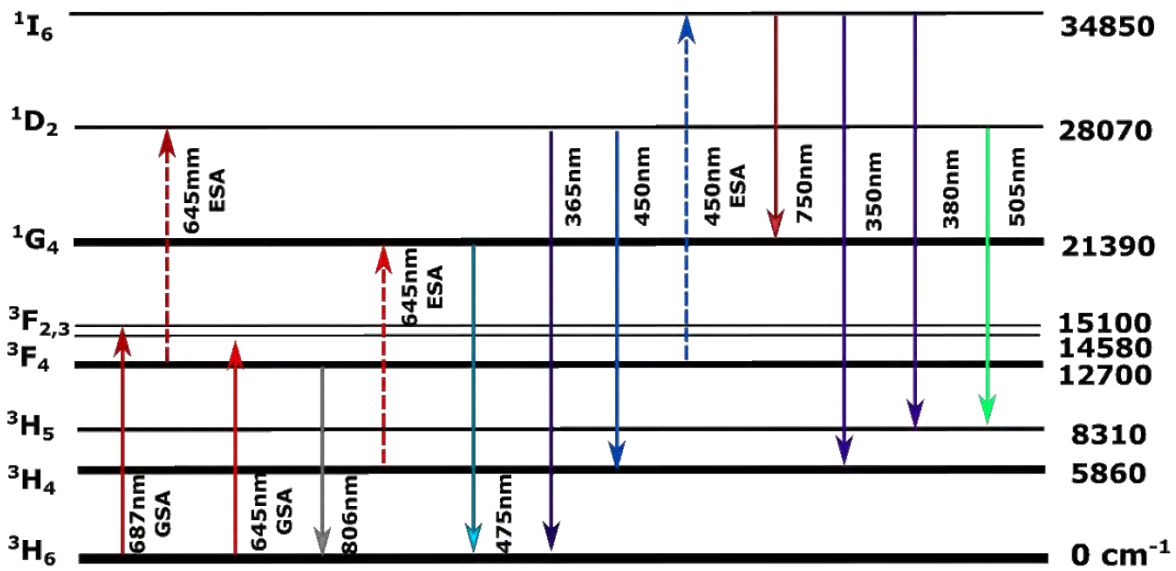

Figure 6.1. Partial energy level diagram of a trivalent thulium ion (Tm^{3+}) in fluoride glass.

The experimental configuration (see **figure 6.2**) consisted of a multimode fluorozirconate ZBLAN glass doped with thulium optical fiber pumped with tunable red AlGaInP LDs. These were coupled into the fiber using 20X microscope objective lenses. The calculated coupled power was estimated to be 60%, this is 65 mW for the ESA pump (645 nm) and 20 mW for the GSA pump (687 nm). We used the same Tm doped ZBLAN optical fiber described in **chapter 5**.

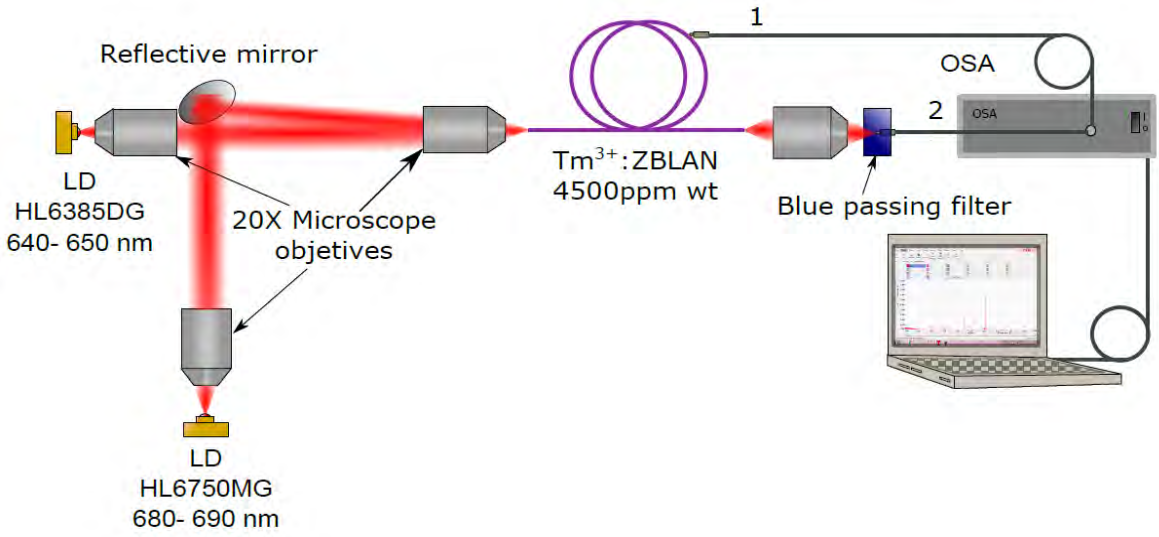

Figure 6.2. Experimental configuration of a Tm^{3+}: ZBLAN laser for the UV laser.

The "cavity" consisted of the Fresnel reflection (*i.e.*, representing approximately a 4% reflection of the fiber/air interface for both cleaved fiber ends). A blue passing filter was used in all measurements to avoid the residual pumps at the output.

6.4 Results and discussions

One of our limitations was the capability to observe the spectral emission in the UV-visible region (350 nm – 480 nm). Since our output is somewhat weak (in the order of units of mW), the optical spectrum analyzer (OSA) *Thorlabs 201*® was not capable to read these signals. Nevertheless, we had the alternative to use another OSA, the *Ocean Optics*® dual fiber optic spectrometer SD2000 model D2J966. But this OSA was un-calibrated. The calibration process is mentioned in **Appendix A**.

We analyzed the lateral fluorescence *i.e.*, the unguided fluorescence from the side of the Tm^{3+}: ZBLAN fiber, (see output 1 in the diagram in **figure 6.2**). We took measurements at different lengths (13 cm, 26 cm, 35 cm and 46 cm) of the optical fiber (the total fiber length was 55 cm). When normalizing all values at a center wavelength (450 nm), we can observe that the relative intensity for shorter lengths (*e.g.*, 13 cm and 26 cm) for the $^1I_6 \rightarrow {}^3H_4$ transition (350 nm) is higher (see **figure 6.3a**). Beyond 26 cm these signals fade away, so to produce these signals, a very short fiber is required. On the other hand, for the IR signal (805 nm) the relative intensity is diminished (see **figure 6.3 b**), so this signal requires longer fibers (beyond 35 cm). Also, it is possible to observe that residual pumps (645 nm and 687 nm) are stronger for shorter fiber lengths (13 cm), since at this distance the GSA and ESA are not completely absorbed along the fiber.

When probing with longer lengths (35 cm and 46 cm) the situation is inverted. The 805 nm IR signal ($^3F_4 \rightarrow {}^3H_6$ transition) is more relative intense since the GSA (687 nm) is better absorbed and produces more easily this transition. The signals corresponding to 475 nm ($^1G_4 \rightarrow {}^3H_6$) and 650 nm ($^1G_4 \rightarrow {}^3H_4$) are also enhanced for larger distances, since this is produced by the reabsorption of the ESA (observe the energy level diagram in **figure 6.1**). The 360 nm ($^1D_2 \rightarrow {}^3H_6$) is also benefited by increasing the fiber length; on the other hand, signal at 350 nm ($^1I_6 \rightarrow {}^3H_4$) is diminished, since this transition is affected by the emission of the 750 nm and 380 nm signals (see **figure 6.1**).

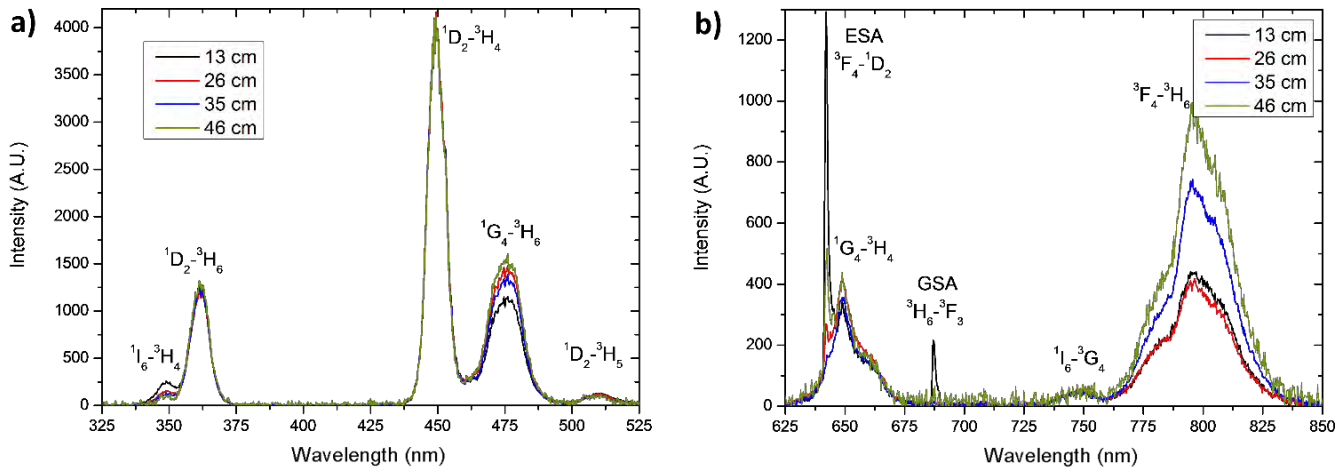

Figure 6.3. Relative intensities for lateral fluorescence at different fiber lengths. a) UV region, b) VIS-NIR region

We also analyzed the lateral fluorescence when the system was excited with each individual pump and with both pumps simultaneously. We took the 26 cm lateral fluorescence as an example (since all measurements behaved likewise). We can observe that when exciting the fiber with just the GSA pump (687 nm), no emission in the UV-Vis region is observed (**figure 6.4a**) since no up-conversion process takes place. On the other hand, the 805 nm signal ($^3F_4 \rightarrow {}^3H_6$ transition) it is remarkable intense (**figure 6.4b**).

When using single pump systems with the ESA pump (645 nm), although weak, there are emissions in the UV to NIR regions (*i.e.*, two and/or up to three photons are absorbed). These transitions do not compete too much with the 805 nm transition, and therefore are more efficient to produce and is better not having long fibers (≥ 35 cm) for this purpose.

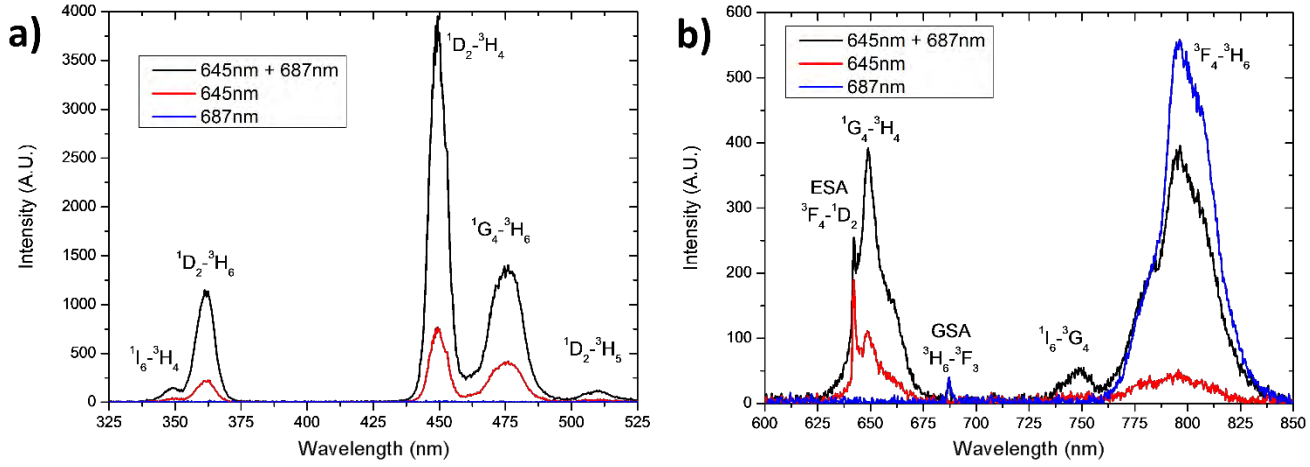

Figure 6.4 Lateral fluorescence for different pump configurations, a) UV-VIS region; b) VIS- NIR region

When exciting with both pumps (687 nm + 645 nm), the UV and visible regions are enhanced remarkably. For the IR region, there is emission comparable to just pumping with 687 nm (**figure 6.4b**).

The fluorescence at the fiber output was also measured *i.e.*, guided fluorescence emerging from the fiber end, (see output 2 in the diagram in **figure 6.2**). We probed two different fiber lengths, 17 cm and 55 cm and analyzed when the system was excited with each individual pump and with both pumps simultaneously.

When observe the UV-visible region (350 nm – 500 nm) in **figure 6.5a**. We observed that for the 17 cm fiber length the 360 nm, 450 nm, and 475 nm signals are present (although a little weak) when pumping with just the ESA pump (645 nm) since absorption of two photons takes place (**figure 6.1**).

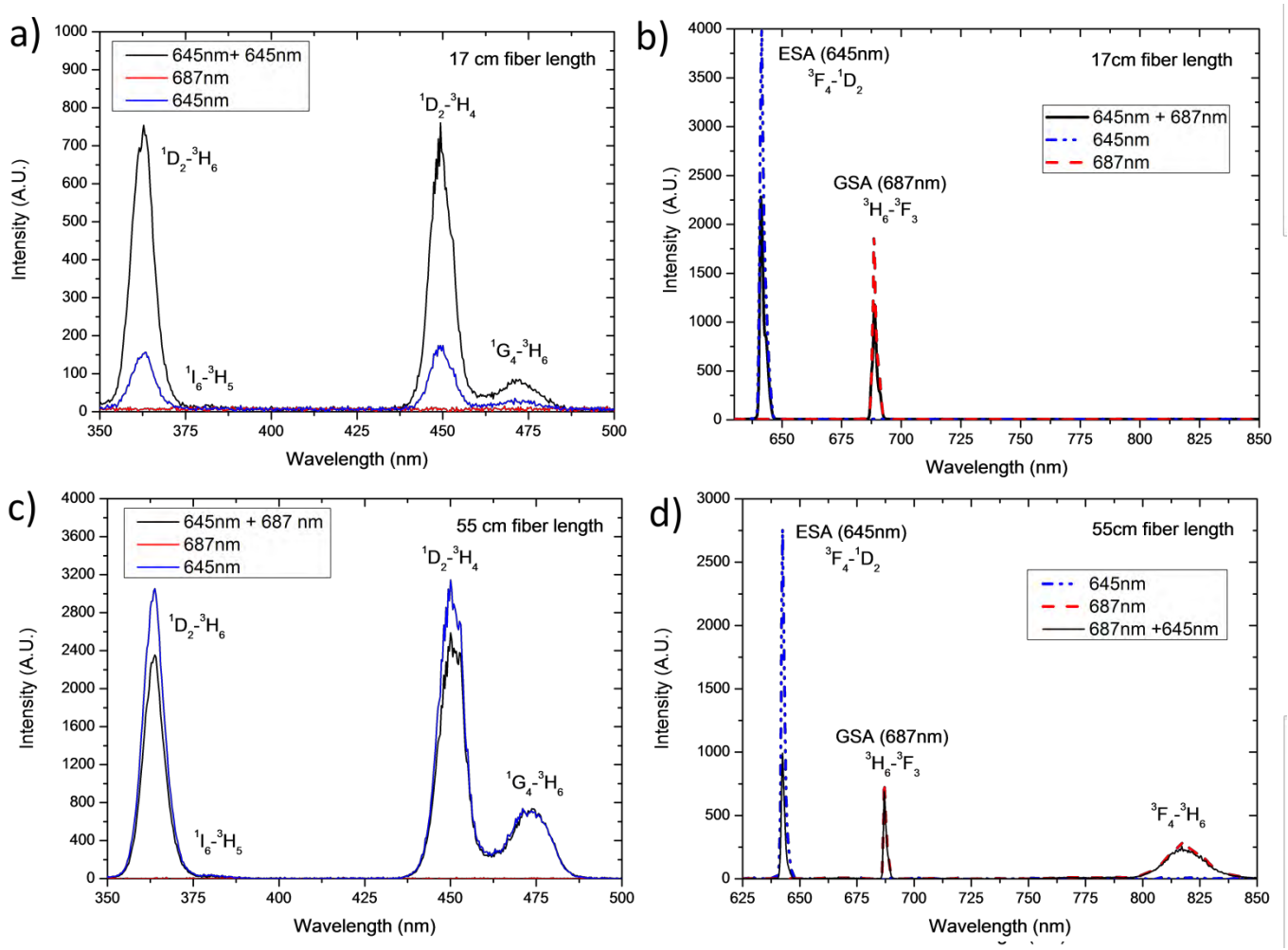

Figure 6.5 Spectral comparison between different fiber lengths at the fiber output: a) UV-Vis region for the 17 cm fiber length; b) Vis-IR region for the 17 cm fiber length, c) UV-Vis region for the 55 cm fiber length and d) Vis-IR region for the 55 cm fiber length

A considerable enhancement for short-wavelength emissions when pumping with both pumps (645 nm + 687 nm), at least a factor of five better than with just ESA pump, can be observed in **figure 6.5a** (black line). The presence of a slight UV signal at 380 nm, corresponding to transition $^1I_6 \rightarrow {}^3H_5$, is also detected. This could be due the reabsorption of the 450 nm signal ($^3F_4 \rightarrow {}^1I_6$). Furthermore, no emission was observed in this region by exciting with just the GSA pump (687 nm). Since too little or no up conversion is present. *i.e.*, this signal (687 nm) is mostly used in the $^3F_4 \rightarrow {}^3H_6$ transition to produce 805 nm.

We also analyzed the visible-IR region (600 nm – 900 nm). We could observe that there was a noticeable attenuation of the ESA signal (645 nm) in the presence of the GSA pump (687 nm) signal for both fiber lengths (17 cm and 55 cm), see **figure 6.5b** and **figure 6.5d**, this phenomenon has been previously reported in [19]; this is related to dopant concentration. The signal at 805 nm was barely detected for the 17 cm fiber length.

For the 55 cm fiber length when exciting with both pumps (645 nm + 687 nm) good emission in UV region ($^1D_2 \rightarrow {}^3H_6$ at 365 nm) and in the visible region ($^1D_2 \rightarrow {}^3H_6$ at 450 nm, $^1G_4 \rightarrow {}^3H_6$ at 475 nm) is observed (**figure 6.5c)**. Contrasting with the 17 cm fiber length system, the output spectrum is improved when exciting with just the ESA pump (645 nm), and as for the previous case, there was no emission in this region when exciting with just the GSA pump (687 nm),

In the visible – IR region (**figure 6.5d**) for the 55 cm fiber length, a strong 805 nm signal showed up corresponding to the $^3F_4 \rightarrow {}^3H_6$ transition. This transition is strongly intensified for the longer fiber lengths, mainly produced by the GSA pump (687 nm).

6.5 Physical model of the processes involved along an active optical fiber

To describe the process of the pump absorption (either 687 nm and/or 645 nm) and ASE amplification along an active optical fiber, the **figure 6.6** is used.

Figure 6.6. Processes of pump absorption and ASE generation along a doped optical fiber.

When pump is introduced into the optical fiber at $z = 0$, a serial of events takes place. The Rayleigh scattering of the pump ($P_p x10^{-6}$) spreads in all directions (a small portion is guided through the fiber) in conjunction with the absorption of the guided pump. This occur together with the generation of the "seed" signal, the fluorescence from dopants + spontaneous emission, which starts to propagate along the fiber and the ASE signal starts growing up (*i.e.*, amplification) and/or being re-absorbed.

When the signal propagates a distance $z = L$ (at the end of the fiber length), the guided ASE + a small portion of the residual pump (the one that was not absorbed along the fiber), and a small portion of fluorescence (negligible compared to other signals) all come out of the fiber. Also, a small portion of Rayleigh scattering of pump + ASE ($P_{ASE} x10^{-6}$ spread in all directions) are present at this point. This analysis is important to understand the results obtained and taking this into account for obtaining optimum fiber lengths (L_{opt}).

6.6 Conclusions

Tm^{3+}-doped fluoride fiber lateral and end fluorescence spectra when pumping with a single and dual- wavelength were investigated. It was found that the fluorescence spectra (lateral and fiber end) is affected by the fiber length and the pump configuration (*i.e.*, with applying one pump or both simultaneously). When modifying these features, abrupt changes in the spectral shape were observed. We concluded that to obtain a strong 350 nm and 360 nm signals, a very short fiber is required. Unlike for 475 nm and 800 nm, where larger lengths are required. Very clear improvement in the UV signal at 450 nm was observed when both pumps work together (for the short fiber length), in contrast with the long fiber length (55 cm), when more intense signals are obtained with just using a single pump at 645 nm (ESA). Attenuation of the residual ESA signal when pumped simultaneously with the GSA signal was also observed for both fiber lengths (i.e., attenuation of light by applying light). The present work is a precedent for producing more efficient short wavelength fiber lasers.

6.7 References

1. C. Czeranowsky, E. Heumann, G. Huber, All-solid-state continuous-wave frequency-doubled Nd:YAG–BiBO laser with 28-W output power at 473 nm, Opt. Lett. 28 (2003) 432. doi:10.1364/OL.28.000432.

2. Z. Quan, Y. Yi, L. Bin, Q. Dapeng, Z. Ling, 13.2 W laser-diode-pumped Nd:YVO4/LBO blue laser at 457 nm, J. Opt. Soc. Am. B. 26 (2009) 1238–1242. doi:10.1364/JOSAB.26.001238.
3. W. Liang, G.Y. Jin, G.C. Sun, X. Yu, B.Z. Li, Z.L. Liang, Diode-pumped Nd:GAB self-frequency-doubling green laser at 531 nm, Laser Phys. Lett. 8 (2011) 366–368. doi:10.1002/lapl.201110007.
4. J.H. Zarrabi, P. Gavrilovic, S. Singh, Intracavity, frequency-doubled, miniaturized Nd:YAlO_3 blue laser at 465 nm, Appl. Phys. Lett. 67 (1995) 2439–2441. doi:10.1063/1.114600.
5. J.Y. Allain, M. Monerie, H. Poignant, Blue upconversion fluorozirconate fibre laser, Electron. Lett. 26 (1990) 166–168. doi:10.1049/el:19900113.
6. R.M. El-Agmy, N.M. Al-Hosiny, 870 mW blue laser emission at 480 nm in a large core thulium doped ZBLAN fiber laser, Laser Phys. 20 (2010) 838–841. doi:10.1134/S1054660X10070066.
7. R. Paschotta, N. Moore, W.A. Clarkson, A.C. Tropper, D.C. Hanna, G. Mazé, 230 mW of blue light from a thulium-doped upconversion fiber laser, IEEE J. Sel. Top. Quantum Electron. 3 (1997) 1100–1102. doi:10.1109/2944.649548.
8. Guanshi Qin, Shenghong Huang, Yan Feng, A. Shirakawa, M. Musha, K. Ueda, Blue up-conversion laser in Tm3+ doped ZBLAN glass fiber, in: 2005 Pacific Rim Conf. Lasers & Electro-Optics, IEEE, n.d.: pp. 824–825. doi:10.1109/CLEOPR.2005.1569559.
9. T.E. Wiest, D.S. Hinkel, Blue laser emission from dual-wavelength-pumped Tm:ZBLAN fiber, in: A.R. Pirich, R.K. Boncek (Eds.), International Society for Optics and Photonics, 1997: pp. 47–51. doi:10.1117/12.277640.
10. R.M. El-agmy, N.M. Al-hosiny, S. Abdallah, M.S. Abdel-aal, Generation of Short Wavelength in Up-Conversion of Tm + 3 Doped Fluoride Glass and Its Application in Fiber Lasers, J. Mod. Phys. 2014 (2014) 123–127. doi:10.4236/jmp.2014.53021.
11. W. Tian, B. Rami Reddy, Ultraviolet upconversion in thulium-doped fluorozirconate fiber observed under two-color excitation, Opt. Lett. 26 (2001) 1580. doi:10.1364/OL.26.001580.
12. P. Barber, R. Paschotta, A. Tropper, D. Hanna, Infrared-induced photodarkening in Tm-doped fluoride fibers, Opt. Lett. 20 (1995) 2195–2197. doi:10.1364/OL.20.002195.
13. H. Gebavi, S. Taccheo, L. LaBlonde, B. Cadier, T. Robin, A. Monteville, et al., Photodarkening: investigation, mitigation and figure of merit, in: M.J.F. Digonnet, S. Jiang, J.C. Dries (Eds.), Proc. SPIE - Int. Soc. Opt. Eng., 2013: p. 86210W. doi:10.1117/12.2008184.
14. M. Juárez-Hernández, E.B. Mejía, Red laser-diode pumped 806 nm Tm 3+ : ZBLAN fibre laser, Laser Phys. Lett. 14 (2017) 65103. doi:10.1088/1612-202X/aa6dbe.
15. P.W. France, M.C. Brierley, Fluoride Glass Fibre Lasers And Amplifiers, Proc. SPIE. 1171 (1990) 65–71. doi:10.1117/12.963139.
16. P. Laperle, A. Chandonnet, R. Vallée, Photobleaching of thulium-doped ZBLAN fibers with visible light, Opt. Lett. 22 (1997) 178–80. doi:10.1364/OL.22.000178.
17. D. Faucher, R. Vallée, Real-time photobleaching and stable operation at 204 mW of a Tm:ZBLAN blue fiber laser, IEEE Photonics Technol. Lett. 19 (2007) 112–114. doi:10.1109/LPT.2006.889101.
18. R. Piccoli, T. Robin, T. Brand, U. Klotzbach, S. Taccheo, Effective photodarkening suppression in Yb-doped fiber lasers by visible light injection, Opt. Express. 22 (2014) 7638. doi:10.1364/OE.22.007638.
19. E.B. Mej a, D. V. Talavera, Red (632.8-nm) attenuation by a copropagating 1175-nm signal in Tm3+-doped optical fibers, Opt. Eng. 46 (2007) 105001. doi:10.1117/1.2790043.

Outcomes

1.1 General conclusions and discussions

Our main goals were to demonstrate and improve new schemes for fiber laser systems, using stimulated Raman scattering and RE doped optical fibers.

For the RFLs, we made investigations for making these lasers more efficient, by studying the energy transfer among all the signals involved (Stokes, Stokes-to-Stokes and anti-Stokes-to-Stokes components). First, we observed that increasing OC reflectivity resulted in a decrease of energy-transfer of pump to other Stokes signals (making it inefficient); we also observed that threshold for Stokes generation was achieved more easily, occurring the contrary for low OC (which improved the energy transfer, but with high threshold operation). Then we proposed systems with low OC reflectivity, using longer fibers for more efficient RFLs, sacrificing lower thresholds, since it is more economic than expending in more FBGs components.

We also investigated new RFL designs, as an alternative for cascade RFLs, where simplifying the cavities (eliminating most of the FBGs) would allow even cheaper and more optimized RFL systems for getting higher Stokes orders. With this proposal, it is possible to substitute the more expensive phosphate fibers. Researches concerning RFLs makes possible to achieve our initial objectives: more efficient, simpler and more economical laser systems.

Regarding the investigations concerning RE doped fiber laser systems, more specifically for Tm^{3+}: ZBLAN, we have demonstrated that LDs can be an excellent option for pumping such laser schemes, allowing to pump the band with most absorption in the Tm^{3+}: ZBLAN (687 nm), and providing high conversion efficiency (close to 40 %). As well pumping in this region (visible) diminishes the photodarkening effect, a phenomenon so undesirable in many laser systems. By pumping with LDs, the costs of acquisition and maintenance are reduced. We demonstrate laser operation at 806 nm at pumping with LDs, and offered an alternative to IR laser sources pumps. This scheme can be used for different applications, such as sensors and optical amplifier for local area network purposes.

We also studied a dual- wavelength pumping scheme (687 nm and 645 nm), where up-conversion mechanisms occur. There were two main factors that affected the operation of our system: fiber length and pump configuration (*i.e*., single pump or dual pump). By changing these factors, we observed an alteration on the optical spectrum (lateral and output). The signal at 450 nm was improved when dual pumping the short Tm^{3+}: ZBLAN fiber (17 cm). On the other hand, by single pumping the 55 cm fiber length (long fiber) the signal at 645 nm was improved. Attenuation of the residual signal at 645 nm when pumped simultaneously with the 687 nm signal was also observed in both fiber lengths (*i.e.*, attenuation of light by applying light). This work is a precedent for producing more efficient short wavelength fiber lasers, by using up-conversion mechanisms with LD dual pump.

1.2 Future work

For future work, we expect to construct a fully functional short wavelength Tm^{3+}: ZBLAN laser (emitting mainly at 365 nm, 450 nm, and 475 nm), by pumping with a dual-visible-wavelength configuration; at 687 mm, the strongest absorption band, and 645 nm. By using these wavelengths, we can expect an optimal absorption (≥ 35 dB/Km/ppm); representing a factor of 3.5 to 7 better than IR and some other visible (485 nm or 585 nm) pump sources. Additionally using 645 nm pump as excited state absorption (ESA) makes possible to obtain a variety of radiative transitions in the UV (360 nm) and in the blue region (450 nm and 475 nm). Exciting at these region (red) makes possible to mitigate the photodarkening effect, usually experienced when pumping with IR sources. Moreover, by using LDs we expect to reduce the total cost of the experimental setup and the energy consumption; expanding the system lifespan, and reducing the total size of the laser system.

Appendix A

Calibration of wavelength of the Ocean Optics USB2000

Appendix A

1. *Calibration of wavelength of the Ocean Optics USB2000*

1.3 Overview

This appendix describes how to calibrate the wavelength of the optical spectrometer *Ocean Optics dual fiber optic spectrometer SD2000 model D2J966*. Since the wavelength of most of the spectrometers will drift slightly as function of time and environmental conditions, it is important to solve this problem.

1.4 Understanding the Ocean Optics USB200

The Optical spectrum analyzer is composed as shows the **figure 1**. The CCD linear sensor (see the 8 element in **figure 1**) assigns a pixel at each determined wavelength of the incident light (*i.e.*, light passing through the slit). The position of these pixels must be calibrated so that the spectrum reading program correctly identifies them.

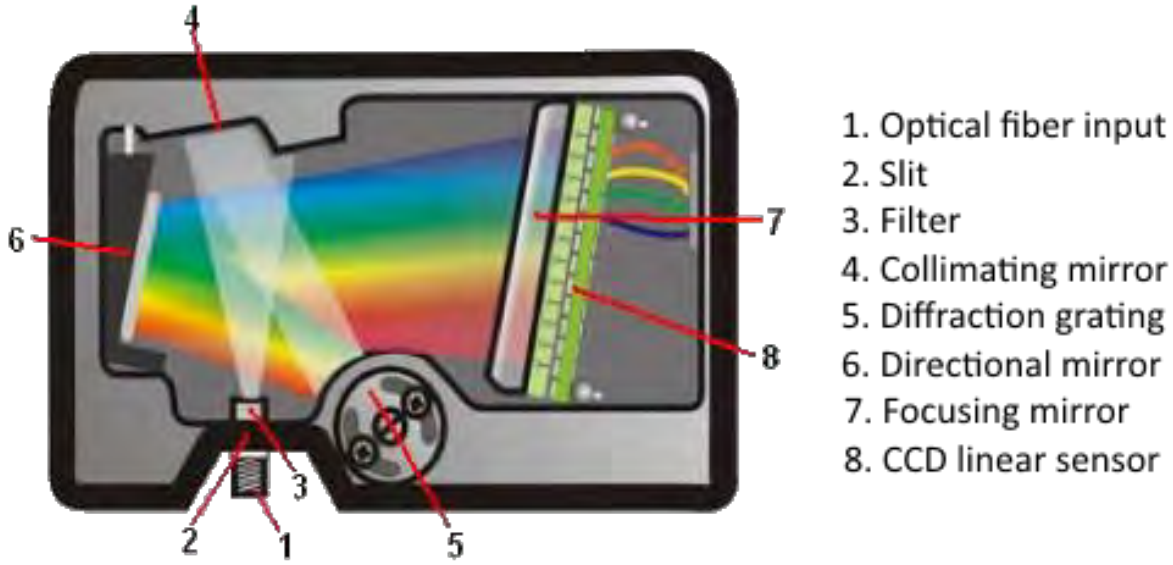

Figure 1. Inner view of a typical optical spectrum analyzer

To calibrate these pixels, we needed to use a light source that produces spectral lines which are known. To obtain this kind of light source we used a mercury lamp (**figure 2**). The mercury lamp provides several specific spectral lines, which range from 250 nm – 600 nm (*i.e.*, from the UV to the visible); allowing us to calibrate this wavelength region.

1.5 Calibrating the wavelength of the spectrometer

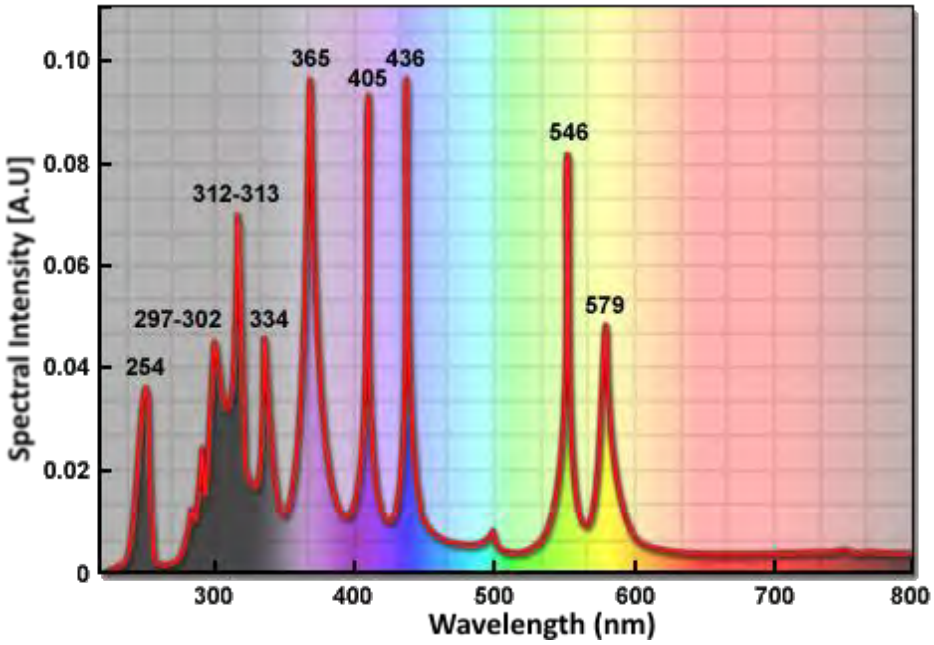

Figure 2. Mercury arc lamp spectral distribution

To properly identify the exact wavelength of these peaks with high definition (in the order of pm), we used our Thorlabs 201 OSA. Later, we took the spectrum of our light source, and identified the position of each peak at the point of maximum intensity, identifying the correspondent pixel number in our un-calibrated Ocean Optics DJ966 OSA. We record this data to later create the **table 1**.

In **table 1** in the first column we place the exact wavelength of the spectral lines that we used (for filling some gaps between wavelengths, *e.g.* 532.09 nm, 643.49 nm and 686.48 nm, we used extra light sources like LDs and the pump of our Ti: Sapphire laser). In the second column, we placed the observed pixel number; in the third and in the fourth columns we calculated the pixel number squared and cubed respectively.

To solve the relation between pixel number and predicted wavelength (calibrated wavelength), we need to perform a 3rd order linear regression that solves the **equation 1**.

$$\lambda_p = I + C_1 p + C_2 p^2 + C_3 p^3 \qquad 1$$

Where λ_p is the predicted wavelength (calibrated), I is the intercept coefficient (wavelength at pixel 0), C_1, C_2 and C_3 are the first, second and third coefficients respectively.

Table 1. Mercury lamp data spreadsheet

True Wavelength	Pixel	Pixel^2	pixel ^3
264	179	32041	5735339
269.93	211	44521	9393931
275.36	224	50176	11239424
280.39	240	57600	13824000
289.46	254	64516	16387064
292.61	280	78400	21952000
296.81	301	90601	27270901
302.27	316	99856	31554496
313.2	347	120409	41781923
334.17	408	166464	67917312
365	499	249001	124251499
390.95	571	326041	186169411
404.7	613	375769	230346397
435.85	705	497025	350402625
532.09	996	992016	988047936
546.1	1038	1077444	1118386872
576.98	1139	1297321	1477648619
643.49	1342	1800964	2416893688
686.48	1482	2196324	3254952168

Table 2. Comparison calibration coefficients between excel and python algorithms for the mercury lamp data

	Excel	Python
First coefficient	0.31692815	0.3174
Second coefficient	2.2982E-05	2.209E-05
Third coefficient	-1.0733E-08	-1.037E-08
Intercept	203.263812	203.2068
Regression Fit	0.99977249	1

We performed the regression fit in Excel and in Python to compare results as in **table 2**.

With these results, we could be able to solve the predicted wavelength value. The results we obtained were the following in shown in **table 3** using the values from the Excel algorithm.

Table 3. Obtained results from the excel algorithm for the mercury lamp data

True Wavelength	Pixel	Predicted wavelength	Difference
265.32	179	260.6687593	4.6512407
269.93	211	271.058008	-1.12800803
275.36	224	275.2882297	0.07177033
280.39	240	280.5019584	-0.11195841
289.46	254	285.0703869	4.38961309
292.61	280	293.569873	-0.95987304
296.81	301	300.4486804	-3.63868042
302.27	316	305.3693258	-3.09932578
312.83	347	315.5566778	-2.72667783
334.17	408	335.6672235	-1.49722354
365.16	499	365.7999244	-0.6399244
390.95	571	389.7247297	1.22527027
405.43	613	403.7044169	1.72558314
435.85	705	434.3599696	1.49003036
532.16	993	530.125834	2.03416602
546.1	1038	544.9936021	1.10639785
576.98	1139	578.200672	-1.22067197
643.49	1342	644.0310783	-0.5410783
686.48	1482	688.4924695	-2.01246946
805.24	1864	804.3581806	0.88181943

The coefficients obtained are not very different from one algorithm to another. The error of the difference between wavelengths (true and predicted) is practically maintained. The maximum error is about 4 nm in the ~260 nm – 290 nm region which is tolerable, since we had previously an error of up to more than 100 nm. This calibration was performed for one of the two channels in the UV - VIS region.

For calibrating the VIS-IR region in the Ocean Optics DJ966 OSA we used a Krypton light source (**figure 3**) and we repeated the process for obtaining the regression coefficients in this spectral region.

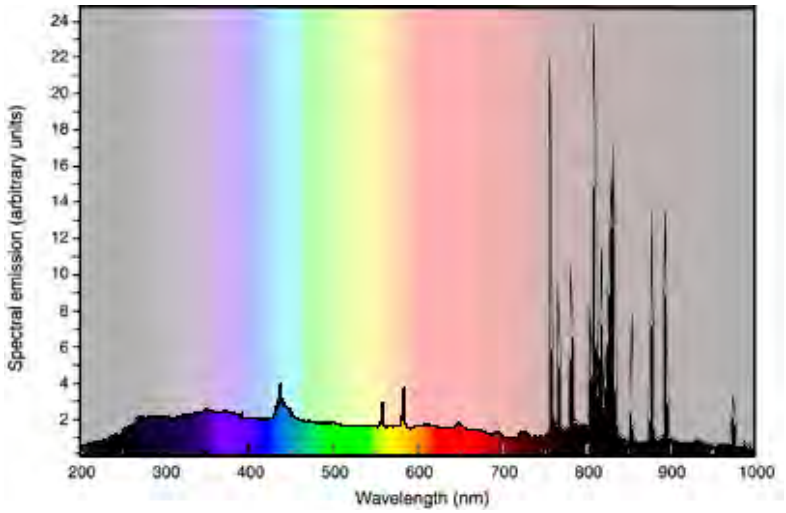

Figure 3. Krypton arc lamp spectral distribution

In **table 4** in the first column we place the exact wavelength of the spectral lines that we used. In the second column, we placed the observed pixel number; in the third and in the fourth columns we calculated the pixel number squared and cubed respectively. Then for solve the **equation 1**, we perform a third-order linear regression in Excel an in Python to compare algorithms (see **table 5**).

With these results, we could be able to solve the predicted wavelength value (λ_p). The results we obtained are shown in **table 6** using the values from the Excel and Python algorithm (these values are the same).

Table 4. Krypton lamp data spreadsheet

True Wavelength	Pixel	Pixel^2	Pixel ^3
532.16	34	1156	39304
557.03	103	10609	1092727
587.1	189	35721	6751269
643.4	358	128164	45882712
686.52	490	240100	117649000
759.56	710	504100	357911000
769.45	738	544644	401947272
785.48	792	627264	496793088
811.29	870	756900	658503000
819.01	895	801025	716917375
829.81	925	855625	791453125
850.89	997	994009	991026973
877.67	1086	1179396	1280824056
892.86	1135	1288225	1462135375
1064.3	1727	2982529	5150827583

Table 5. Comparison calibration coefficients between excel and python algorithms for Krypton lamp data

	Excel	Python
First coefficient	0.3477516	0.3478
Second coefficient	-1.3845E-05	-1.385E-05
Third coefficient	-3.1064E-09	-3.106E-09
Intercept	520.972358	520.9724
Regression Fit	0.9999685	1

Table 6. Obtained results from the excel and python algorithm for the Krypton Lamp data

True Wavelength	Pixel	Predicted wavelength	Difference
532.16	34	532.7797857	-0.61978573
557.03	103	556.6404961	0.38950385
587.1	189	586.1818786	0.91812143
643.4	358	643.5504621	-0.15046209
686.52	490	687.680979	-1.16097895
759.56	710	759.7848909	-0.22489092
769.45	738	768.8238085	0.6261915
785.48	792	786.1638896	-0.68388961
811.29	870	810.9913652	0.29863484
819.01	895	817.9053094	1.10469064
829.81	925	828.3378573	1.47214273
850.89	997	850.8400875	0.04991247
877.67	1086	878.3230691	-0.65306914
892.86	1135	893.2929338	-0.43293377
1064.3	1727	1064.245711	0.05428857

As one may notice the error is minimal, with a maximum error of ~1.46 nm around 830 nm. With these results, we could now measure the optical spectrum in the (master) 260 nm – 850 nm (slave) and from 500 nm – 1100 nm.